A non Gaussian model for the lateral dose evaluation in hadrontherapy: development and Treatment Planning System implementation

Valentina Elettra Bellinzona

Pavia, München
2016

A non Gaussian model for the lateral dose evaluation in hadrontherapy: development and Treatment Planning System implementation

Valentina Elettra Bellinzona

A thesis submitted for the degree of

PhilosophiæDoctor (PhD) for Università degli Studi di Pavia
Doktor der Naturwissenschaften for Lüdwig-Maximilians-Universität München
Under cotutelle agreement

Università degli Studi di Pavia, Ludwig-Maximilians-Universität München

Submitted by
Valentina Elettra Bellinzona
Born in Pavia on 14/01/1990

First advisor for Università degli Studi di Pavia: Prof. Dr. Alberto Rotondi
First advisor for Ludwig-Maximilians-Universität München: Prof. Dr. Katia Parodi
Second advisor for Università degli Studi di Pavia: Dr. Andrea Fontana
Submission: Munich, 9/01/2017
Defence: Pavia, 16/02/2017

Contents

List of Figures **vii**

List of Tables **xiii**

1 Introduction to the lateral spread of an hadrontherapy beam **9**

1.1 Particle therapy 9

1.2 Dose deposition and lateral beam shape 12

2 A non Gaussian model for lateral displacement calculation **15**

2.1 Electromagnetic core: Molière theory 16

2.1.1 Derivation of the crucial parameters 21

2.1.2 Projected angle distribution 25

2.1.3 Compound and mixture generalization 27

2.1.4 Energy loss 28

2.1.5 Lateral displacement 30

2.2 Nuclear effects 32

2.3 Model summary 34

2.4 Validation 35

2.4.1 Electromagnetic core results 36

2.4.2 Complete model results 36

2.4.3 Beam scan result 44

2.5 From one dimensional to two dimensional distributions 45

2.6 Conclusion 48

3 Treatment Planning system implementation **49**

3.1 Introduction 49

3.2 Clinical volumes 50

3.3 CERR - A Computational Environment for Radiotherapy Research . 52

3.4 Dose evaluation 52

3.4.1 Lateral dose evaluation 56

3.5 Optimization process 57

3.6 Treatment quality quantification 59
3.6.1 Dose-Volume-Histogram 60
3.7 MC database comparison 61
3.7.1 Geant4 61
3.7.2 FLUKA 61
3.7.3 Comparison Results 62

4 CERR Results **65**
4.1 Single beam 65
4.1.1 Phantom set up 65
4.1.2 Lateral beam comparison 66
4.1.3 Kolmogorov-Smirnov test 69
4.1.4 Lateral width 69
4.2 Full treatment plan 74
4.2.1 Dose Volume Histogram 77
4.2.2 Kolmogorov-Smirnov test 80
4.2.3 Residual analysis 81
4.3 Inhomogeneities 83
4.3.1 Bone 84
4.3.2 Fat 88
4.4 Conclusion 90

5 Conclusions **93**

References **95**

List of Figures

1.1 Facilities in clinical operation and the number of patients treated from 1955 to 2014. 10

1.2 Energy deposited by different particles in function penetrate depth. Protons and carbon ions deposit most of their energy at a specific depth, with the Bragg Peak curve, whereas photons used in conventional X-rays tend to leave energy all along their path [1]. 11

1.3 Calculated beam spread for protons and ^{12}C ions in a typical treatment beam line. The particle beam is parallel with an initial FWHM (Full Width at Half Maximum) of 5 mm, and passes through the nozzle, including a thin vacuum window and beam monitors and enters a water absorber patient at 1 m distance from nozzle exit. Figure courtesy of U. Weber, Rhön-Klinikum AG 12

2.1 Effect of Multiple Coulomb Scattering 16

2.2 Schematic representation of the two main angles of the theory, χ and θ. 18

2.3 Schematic view of lateral displacement y_M of the angular distribution on the transverse plan. 30

2.4 Comparison between the analytical model (red line), FLUKA (blue histogram) and MCNP6 (green histogram, slightly below the line on the log scale) in water for 200 MeV protons at a depth of 18 cm in log (left) and decimal (right) scale. All the nuclear effects (target fragmentation) are excluded. 37

2.5 Simulation geometry setup 38

2.6 Lateral profiles of the original phase space at the isocenter for $158.58\,MeV$ proton beam at $z = 0\,cm$ depth (left) and lateral beam divergences at $z = 16.55\,cm$ (right), obtained by replacing water with vacuum. The solid lines is the fit with the function of Eq.2.73 before the convolution with the model. 38

2.7 Behaviour of the free parameters A and b as a function of normalized depth for *81.49 MeV* (upper) and for *158.58 MeV* (lower). 40
2.8 Maximum distance D obtained from the Kolmogorov Smirnov test between the model and the FLUKA simulation. 41
2.9 Comparison between analytical model, FLUKA simulation and experimental data for 81.49 MeV in water for a thickness of: z=1.57 cm in logarithmic (left) and linear (right) scales. The curves are normalized to the maximum of the FLUKA histogram, obtained by fitting the highest dose channels with a smooth curve. In the normalization zone the error of the data points is 2% (see section 2.4.2). 42
2.10 As in figure 2.9 with z=4.57 cm. Bragg peak is at 5.38 cm 43
2.11 As figure 2.9 with E=157.43 MeV and z=11.55 cm. 43
2.12 As figure 2.11 with z=16.55 cm. Bragg peak is at 17.23 cm 43
2.13 Lateral dose profile for a beam scan for the energy 81.49 MeV. In green a subset of the original single beams is shown. 44
2.14 Example of a bidimensional Gaussian distribution 45

3.1 Schematic flowchart of a inverse treatment planning system 50
3.2 The diagram shows the various volumes to be considered. GTV is the volume as seen by physicians. CTV is the volume calculated according to the pathological knowledge of usual local invasion by cancer. PTV is a compromise taking into account various physiological phenomena (respiration, difficulties in positioning the patient, patient movement) as well as the Internal Margin (IM) to be added to CTV to compensate for internal physiologic movements and variation in size, shape, and position of the CTV during therapy in relation to an internal reference point and its corresponding coordinate system, and the Set-up Margin (SM) for patient movement and set-up uncertainties. Normal tissue (in dark green) is included in the PTV. The arrows show various attempts to reduce parasitical irradiation, the ideal being of course the smallest volume (ICRU Report no. 62 (25). 51
3.3 Screenshot of CERR interface; the three gray windows are the different cutting planes. The structures are displayed in different colours, in this case WORLD (green), PTV (red) and PTV+1 (cyan). The dose distribution is illustrated in colours with the intensity colour scale on the left. 53
3.4 Schematic representation of beam scanning method 53

3.5 Schematic representation of beam scanning method 55

3.6 Beam structure: One beam direction is divided into parallel Pencil Beams. The PBs are placed on a equidistant (lateral) grid and CERR chooses the PBs that hit the CTV. Every chosen PB is sub- divided into spots. One spot reflects one (available) particle energy. The spots have different weights to perform a Spread-out Bragg peak (SOBP). 56

3.7 Schematic view of the CERR lateral dose evaluation. 58

3.8 Example DVH of a CTV. The area highlighted in orange is correlated with the mean dose. The determination of V_{98} is indicated by the two black arrows. 60

3.9 Plot of the comparison between Geant4 and FLUKA values of FWHM, Full Width 80% Maximum (FW80M) and Full Width 95% Maximum (FW95M), for $Z_{rel} = 20\%, 60\%, 80\%, 90\%$ at $E = 158$MeV 62

3.10 Comparison of the lateral energy distribution between Geant4 (red curve) and FLUKA (blue curve) for a proton beam of initial $\sigma = 0.8cm$ and energy $E = 158$MeV, at a normalized depth of $z_{rel} = 20\%$ 63

3.11 As in 3.10 for a normalized depth of $z_{rel} = 80\%$ 63

3.12 Comparison of the energy distribution between FLUKA (top) and Geant4 (bottom) for a proton beam of initial $\sigma = 0.8$cm and energy $E = 158$MeV 64

4.1 Plot of CERR database of the position at 80% of the peak dose (before the peak) versus the energy. This curve is used by the TPS to select the beams that are needed to achieve the best dose delivery to the PTV region. 66

4.2 Example of geometry set up displayed in CERR interface. The world is a parallelepiped of water of $10 \times 10 \times 30\,\mathrm{cm}^3$ displayed in green, the PTV in red, is $1 \times 1 \times 1\,\mathrm{cm}^3$ positioned at a depth of 20 cm and the cyan region is the safety margin in which the dose has to be minimized by the optimizer, it is delineated following the clinical requirements, adding 1 cm^3 to the PTV. 67

4.3 Lateral profile of the dose deposition evaluated by CERR TPS, in logarithmic scale for a single beam of energy E=60 MeV at a relative depth of Z_{rel} = 50% **(a)** and Z_{rel} = 95% **(b)**; the same for E=148 MeV **(c)**,**(d)** and E=195 MeV **(e)**,**(f)**. The blue curve represents the dose calculated using the DG lateral approximation to evaluate the plan, in red, the one obtained using the model to evaluate the same plan and the green one is the *MC Opt ReCalc*. 68

4.4 P-value results of Kolmogorov-Smirnov test for the energy E=64 MeV **(a)**, E=148 MeV **(b)**, E=195 MeV **(c)** at the relative depths of Z_{rel} = 0%, 20%, 50%, 95%. A linear interpolation of the points is added to improve visualization. The DG values are displayed in blue, the model ones in red. 70

4.5 Plots of the values for the FWHM **(a)**, FW20%M **(b)**, FW10%M **(c)** and FW0.5%M **(d)** for a single beam of energy E=64 MeV at relative depths of Z_{rel} = 0%, 20%, 50%, 95%. 71

4.6 Same as in Fig.4.5 for a single beam of energy E=148 MeV. 72

4.7 Same as in Fig.4.5 for a single beam of energy E=195 MeV. 73

4.8 Full treatment plan dose deposition using the model results to evaluate the lateral beam shape, displayed in CERR interface. The geometry set up is a world of water of $10 \times 10 \times 30\text{cm}^3$ displayed in green, the PTV in red, is $1 \times 1 \times 1\text{cm}^3$ positioned at a depth of 20 cm and the cyan region is the safety margin in which the dose has to be minimized by the optimizer, it is delineated following the praxis requirement, adding 1 cm^3 to the PTV. The lateral cutoff is extended until 5 cm, to study the lateral differences between the different approaches, while the default one is normally evaluated at 2σ; this is the reason for which in the WORLD area, a blue dose region is displayed. 74

4.9 Lateral profile of the dose deposition evaluate by CERR TPS, for a full treatment plan. Fig. **(a), (c), (e)**, show the comparison between the dose evaluated using the DG lateral approximation to evaluate the plan in blue and the DG *MC Opt ReCalc* in cyan, is shown for relative depths of Z_{rel} = 20%, 50%, 95%. Fig. **(b), (d), (f)**, show the same comparison but using the model, in red and its *MC Opt ReCalc* in green. 76

4.10 DVH calculated by CERR, for the PTV, the safe margin of PTV + 1 cm and the WORLD regions, both for the plan obtained with the DG (blue curves) and its *MC Opt ReCalc* (cyan curves). 78

4.11 Same as in Fig.4.10 for the model (red curves) and its *MC Opt ReCalc* (green curves). 78
4.12 Same as in Fig.4.10, comparing the results of the DG (blue curves) and the model ones (red curves). 79
4.13 P-value results of Kolmogorov-Smirnov test for the the full treatment plan dose evaluation,at the relative depths of $Z_{rel} = 0\%$, 20%, 50%, 95%. The points are joined by a segmented line to improve visualization. The DG values are displayed in blue, the model ones in red 80
4.14 Net difference between the dose deposition in Gy, obtained for the treatment using DG lateral parametrization and the relative *MC Opt ReCalc (left)* and using the model evaluation compared in the same way with the MC re-evaluation for the model *(right)*; both for the relative depth $Z_{rel} = 50\%$. 81
4.15 Same as in Fig.4.14 for the relative depth $Z_{rel} = 80\%$. 82
4.16 Same as in Fig.4.14 for the relative depth $Z_{rel} = 95\%$. 82
4.17 Geometry set up displayed in CERR interface. The same as in Fig.4.2 with the inclusion of an inhomogeneity region of a parallelepiped of bone of $10 \times 10 \times 4\text{cm}^3$ 84
4.18 Lateral profile of the dose deposition evaluate by CERR TPS, at a relative depth of $Z_{rel} = 50\%$ **(a)**, $Z_{rel} = 70\%$ **(b)**, $Z_{rel} = 80\%$ **(c)** and $Z_{rel} = 95\%$ **(d)**, in logarithmic scale, for a single beam of energy $E = 198$ MeV in presence of a bone inhomogeneity. The blue curve represents the dose evaluated using the DG lateral approximation, in red, the one obtained using the model to evaluate the same plan and the green the *MC Opt ReCalc*. 85
4.19 P-values results of Kolmogorov-Smirnov test for for a single beam of energy $E = 198$ MeV, in presence of a bone inhomogeneity schematically represented with the gray bar. Results are reported for a relative of depth of $Z_{rel} = 50\%$ before bone, $Z_{rel} = 70\%$ inside bone and relative depths of $Z_{rel} = 80\%$, 95% after bone. A segmented line that connects points is added to improve visualization. The DG values are displayed in blue, the model ones in red. 86
4.20 Plots of the values for the FWHM **(a)**, FW20%M **(b)**, FW10%M **(c)** and FW0.5%M **(d)** for a single beam of energy $E = 198$ MeV, in presence of a bone inhomogeneity schematically represented by with the gray bar, at the relative depths of $Z_{rel} = 0\%$, 20%, 50% before bone, and 70% inside bone, 80%, 95% after bone. 87

4.21 Lateral profile of the dose deposition evaluate by CERR TPS, at a relative depth of $Z_{rel} = 50\%$ **(a)**, $Z_{rel} = 70\%$ **(b)**, $Z_{rel} = 80\%$ **(c)** and $Z_{rel} = 95\%$ **(d)**, in logarithmic scale, for a single beam of energy $E = 183$ MeV in presence of a fat inhomogeneity. The blue curve represents the dose evaluated using the DG lateral approximation to evaluate the plan, in red, the one obtained using the model to evaluate the same plan and the green one is the *MC Opt ReCalc*. 89

4.22 P-values results of Kolmogorov-Smirnov test for for a single beam of energy $E = 183$ MeV, in presence of a fat inhomogeneity schematically represented by the gray bar, at the relative depths of $Z_{rel} = 0\%$, 20%, 50% before fat, $Z_{rel} = 70\%$ inside fat and $Z_{rel} = 80\%$, 95% after fat. A linear interpolation of the points is added to improve visualization. The DG values are displayed in blue, the model ones in red. 90

4.23 Plots of the values for the FWHM **(a)**, FW20%M **(b)**, FW10%M **(c)** and FW0.5%M **(d)** for a single beam of energy $E = 183$ MeV, in presence of a fat inhomogeneity schematically represented by the gray bar, at the relative depths of $Z_{rel} = 0\%$, 20%, 50% before fat, and 70% 80% 95% after fat. 91

List of Tables

2.1 Parameters used for the range calculations of Eq.2.57 29

4.1 *Geant4* element composition for bone 84
4.2 *Geant4* element composition for fat 88

To my mum,
that has never told me which is the right way,
lovingly keeping my hand on all my ways.

To my dad
that has drawn a lot ways, sharing his colors with me,
encouraging to draw my own one.

To my little and immeasurable sister,
that without words has shown me a world.

Abstract

Challenging issues in Treatment Planning System for hadrontherapy are the accurate calculation of dose distribution, the reduction in memory space required to store the dose kernel of individual pencil beams and the shortening of computation time for dose optimization and calculation.
In this framework, the prediction of lateral dose distributions is a topic of great interest [2] because currently, a Double Gaussian parametrization [3],[4] is typically used as approximation although other parameterizations are also available [5],[6],[7]. The best accuracy for this kind of calculations can be obtained by Monte Carlo (MC) methods [8], at the expense of a long computing time.
As alternative, we propose a flexible model based on the full Molière theory for Coulomb multiple scattering [9]. The use of the original equations of the theory allows to remove free parameters for the electromagnetic interaction with the advantage of full accuracy with a reasonable increase in the computing time. The contribution of the nuclear interactions are also fully taken into account with a two-parameters fit on FLUKA simulation [10],[11] and this part is added to the electromagnetic core with a proper weight [12]. The model has been validate with MC simulations and with Heidelberg Ion-Beam Therapy Center (HIT) experimental data.
In a second step, the model has been inserted in a research Treatment Planning System CERR - A Computational Environment for Radiotherapy Research [13],[14] at the Ludwig-Maximilians-Universität München, to compare its result against the ones obtained with the currently used Double Gaussian parametrization to evaluate the lateral energy deposition.
A quantitative comparison has been done to evaluate the difference between a treatment plan obtained using the Double Gaussian parametrization and a treatment plan obtained using the model calculation, in the cases of a single beam and a full treatment plan in homogeneous water phantom and also a plan is performed in presence of inhomogeneities.

Extended outlines

Chap.1 presents a general introduction to hadrontherapy, with a focus on the problem of the calculation of the lateral beam profile, introducing its importance in clinical practice.

Chap.2 describes an original model based on Molière theory for Coulomb multiple scattering [9], to calculate the lateral beam profile. First, the pure electromagnetic part is explained, whit its validation with MC calculation, followed by the explanation of how the nuclear part is added to obtain a model that takes into account all the relevant interactions in proton-therapy contest. Hereafter, the model validation against MC simulations and experimental data is presented. At the end, the generalization at the two dimensional case is presented with the application of the theory of non-Gaussian cases.

Chap.3 introduces the treatment planning systems workflow, preceded by an overview of the clinical volumes definition and clinical requirements. A focus is given on CERR - A Computational Environment for Radiotherapy Research [13],[14] treatment planning systems, explaining its characteristics and the dose evaluation process. Within this, a special attention is paid to the lateral dose calculation and the model implementation process. The dose optimization process and the general treatment quality quantifications follow. At the end, the comparison between the *Geant4* and FLUKA simulation results is given, since the model has been validated on FLUKA simulation and CERR databases are built bases on *Geant4* simulation results.

Chap.4 aims to present the results obtained by implementing our model in the CERR workflow. The model takes as input energy and depth automatically from the TPS workflow, and evaluates the lateral beam profile requires for the treatment. The dose obtained using this method is compared with the one obtained using the currently used Double Gaussian approximation.

First, the case of a single beam in homogeneous water phantom is studied for several energies and depths, and the results are validated on *Geant4* simulations. A quantitative analysis is performed using a Kolmogorov-Smirnov test and a lateral width evaluation. After, a full treatment plan is studied with the same tests of the previous case, and an additional analysis of the residuals and the DVH are also shown. To conclude,

an inhomogeneous phantom is considered, studying the impact of the presence of fat and bone tissues on the lateral profile calculation.

Zusammenfassung

Eine der anspruchsvollsten Herausforderungen in der Bestrahlungsplanung von Ionenstrahltherapie ist die präzise Berechnung der Dosisverteilung im Patienten, die Reduktion des Speicherbedarfs der Dosiskernel von einzelnen Pencil-beams, sowie die Verkürzung der Rechenzeit für Dosisoptimierung und berechnung [2]. In diesem Rahmen ist die Berechnung der lateralen Protonen-Dosisverteilungen ein Thema von großem Interesse, da momentan eine Double Gaussian Parametrisierung [3],[4] als Näherung verwendet wird, obwohl weitere Parametrisierungen existieren [5],[6],[7]. Die größte Genauigkeit für diese Art von Berechnungen kann mit Monte Carlo (MC) Simulationen erzielt werden [8], jedoch auf Kosten langer Laufzeiten. Als Alternative wird in dieser Arbeit ein flexibles Modell vorgeschlagen, welches auf der vollständigen Moliere-Theorie für Multiples Coulomb Streuung basiert [9]. Die Verwendung der originalen Gleichungen der Theorie erlaubt die Reduktion der freien Parameter für die elektromagnetischen Wechselwirkungen, was den Vorteil der vollen Genauigkeit mit einer moderaten Erhöhung der Rechenzeit vereint. Der Beitrag von nuklearen Wechselwirkungen wird mit einem zwei-Parameter Fit an FLUKA Simulationen [10],[11] berücksichtigt und dieser Anteil wird dann zu dem elektromagnetischen Core mit einer Gewichtung addiert [12]. Das Modell wurde in das Forschungs-Bestrahlungsplanungssystem CERR A Computational Environment for Radiotherapy Research [13],[14] implementiert, um die Ergebnisse bei der lateralen Dosis-Deposition mit der momentan verwendeten Double Gaussian Parametrisierung zu vergleichen. Ein quantitativer Vergleich wurde durchgeführt zwischen den Bestrahlungsplänen die einmal mit der Double Gauss Parametrisierung und einmal mit dem vorgeschlagene Modell berechnet wurden. Das untersuchte Szenario beinhaltete Pläne die entweder für einzelne Strahlen verschiedener Energien in einem homogenen Wasserphantom, ein voller Bestrahlungsplan in einem homogenen Wasserphantom, sowie einzelne Strahlen verschiedener Energien für ein Phantom mit Inhomogenitäten berechnet wurden.

Abstract

Temi di grande interesse nell'ambito dello sviluppo dei Software per il calcolo di piani di trattamento per adroterapia (Treatment Planning System (TPS)), sono la riduzione dei tempi computazionali del calcolo e dell'ottimizzazione della dose, e la riduzione della memoria richiesta per l'archiviazione della dose di ogni singolo fascio (pencil beam).
In questo contesto, la valutazione della distribuzione laterale della dose è un argomento di grande interesse [2] in quanto attualmente viene utilizzata una funzione a doppia gaussiana [3],[4] come approssimazione, che risulta non completamente accurata. Altre parametrizzazioni sono disponibili [5],[6],[7]; anch'esse rimangono però approssimazioni. La migliore accuratezza per questo tipo di calcolo della dose viene ottenuta utilizzando le tecniche Monte Carlo (MC)[8] che richiedono però tempi computazionali molto lunghi.
In alternativa, questo lavoro propone un modello flessibile e analitico basato sulla teoria completa di Molière per la valutazione dello scattering multiplo di Coulomb [9]. L'utilizzo delle equazioni originali di questa teoria permette di rimuovere ogni parametro libero per il calcolo delle interazioni elettromagnetiche, ottenendo così il vantaggio di un'accuratezza pari a quella del metodo MC ma con tempi di calcolo di molto inferiori. Il contributo delle interazioni nucleari è considerato tramite un fit, con soli due parametri, sulle simulazioni MC FLUKA [10],[11]. La funzione viene aggiunta alla parte analitica elettromagnetica assegnando ad entrambe un fattore di peso di senso fisico, calcolato appropriatamente [12]. Il modello così ottenuto è stato validato con simulazioni MC e con dati sperimentali del centro di adroterapia di Heidelberg, Heidelberg Ion-Beam Therapy Center (HIT).
Successivamente, il modello è stato inserito nel TPS di ricerca CERR - A Computational Environment for Radiotherapy Research [13],[14] presso l'università di Monaco Ludwig-Maximilians-Universität München, per confrontare i risultati ottenuti valutando piani di trattamento che utilizzano l'approssimazione gaussiana per il calcolo della dose, con piani di

trattamento che utilizzano il modello per il calcolo della dose stessa.
Uno studio quantitativo è stato svolto considerando i casi di: singoli fasci di energia fissata in un fantoccio di acqua omogeneo, un piano di trattamento completo (come caso reale della pratica clinica, che considera più fasci di diverse energie e posizioni) in un fantoccio di acqua omogeneo, e infine i casi di singoli fasci a energie fissate in fantocci che presentano disomogeneità.

Chapter 1

Introduction to the lateral spread of an hadrontherapy beam

1.1 Particle therapy

14.1 million: The number of new cancer cases diagnosed in 2012 worldwide.
8.2 million: The number of cancer deaths in 2012 worldwide.
21.7 million: The number of new cancer cases expected to be diagnosed in 2030.[15]

Particle radiotherapy treatments constitute about the 1% of the total number of treatments for patients receiving radiotherapy worldwide. In the recent past, there is a significant interest by all groups involved in this technology, that is emerging as one of the prime modality of cancer treatment [16]. From 1954 through 2014, a total of 137,179 patients across the world have been treated with all forms of particle therapy (Fig.1.1) since it was first started in Berkeley at the Lawrence Berkeley Laboratories (LBL) in 1954.

Why particle therapy?
The answer is based on two main characteristic of ions, one is on the physics behaviour and the second on the radio-biological aspect.
High-energy beams of charged nuclear particles like protons and heavier ions offer significant advantages for the treatment of deep-seated local tumours in comparison to conventional megavolt photon therapy. Their physical depth-dose distribution in tissue is characterized by a small entrance dose and a distinct maximum near the end of range with a sharp fall-off at the distal edge, called *Bragg peak* (see Sec.1.2). Taking full advantage of the well-defined range and the small lateral beam spread, modern scanning beam systems allow delivery of the dose with millimetre precision.

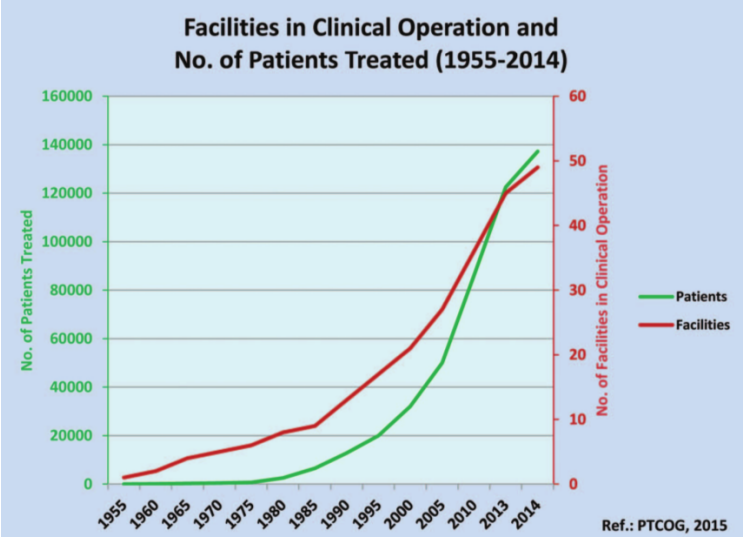

Figure 1.1: Facilities in clinical operation and the number of patients treated from 1955 to 2014.

In addition, projectiles heavier than protons such as carbon ions exhibit an enhanced biological effectiveness in the Bragg peak region caused by the dense ionization of individual particle tracks, that cause an increased amount of cluster damages resulting in reduced cellular repair while LET[1] is increasing. This makes them particularly attractive for the treatment of radio-resistant tumours localized near organs at risk [18].

More specifically, the *physical* advantage is due to the characteristic depth−dose profile, analytically based on the Bethe-Bloch formula described by the Bragg curve, named after Sir William Henri Bragg who investigated the slowing down of α particles in air [19]. Many years later Wilson [20] proposed the application of protons and heavier ions for precision exposures in radiotherapy. A comparison of depth-dose profiles for electromagnetic (radiation X-rays and mega-volt photon beams) and particle beams (protons and carbon ions) is reported in Fig.1.2.

For high-energy photons mostly used in conventional therapy nowadays the initial dose build-up, mainly caused by forward scattered Compton electrons, shifts the peak dose by a few centimetres away from the surface of the patient's body, thereby improving the target-to-entrance dose and sparing the radiosensitive skin. In contrast to photons, the dose profiles of protons and heavier ions are characterized by a distinct narrow peak at the end of their path. The position of this peak can be precisely adjusted to the desired depth in tissue by changing the kinetic energy of the incident ions, by summing several peak a highly conformal dose region

[1]Linear energy transfer (LET) is the average amount of energy a particular radiation imparts to the local medium per unit length; ie: Energy per Length [17].

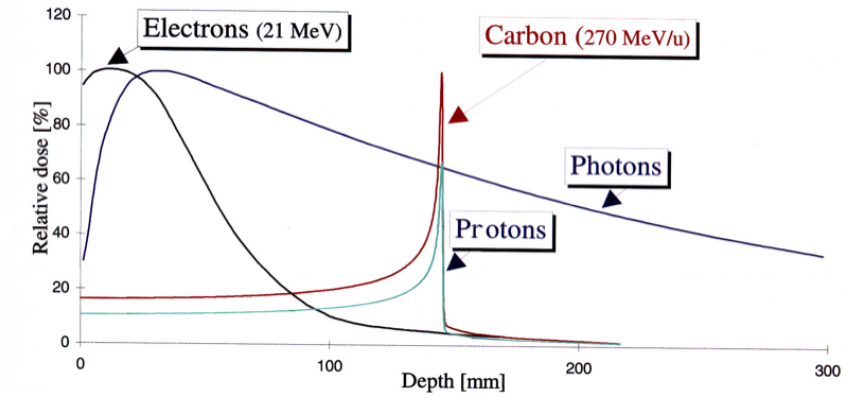

Figure 1.2: Energy deposited by different particles in function penetrate depth. Protons and carbon ions deposit most of their energy at a specific depth, with the Bragg Peak curve, whereas photons used in conventional X-rays tend to leave energy all along their path [1].

can be achieved the *spread-out Bragg-peak* with the possibility of covering (even small) tumour volumes with high accuracy. But heavy ions (unlike protons) exhibit also a characteristic dose tail behind the Bragg peak, which is caused by secondary fragments i.e. mainly projectile fragments, produced in nuclear reactions along the stopping path of the ions, resulting in a complex radiation field [21].

Under the *biological* point of view [18], protons and heavier ions have different radiobiological effectiveness[1] (RBE), protons have a similar biological effect as photons at the same absorbed dose in the plateau region, and higher RBE on the peak region that anyway remains lower respect to the one of heavy ions; them show higher effectiveness ranging from low RBE values in the plateau region to a significant enhancement in the Bragg peak [22]. The reason for this higher RBE is the high ionization density produced by the carbon ion as it traverses a cell, and this results in more disruptive damage to the DNA double helix.

Furthermore, heavy ions also have a lower *Oxygen-Enhancement Ratio*[2] (OER). Both the higher RBE and the lower OER, especially in and around the Bragg peak, can

[1] The relative biological effectiveness (RBE) is the ratio of biological effectiveness of one type of ionizing radiation relative to another, given the same amount of absorbed energy. The RBE is an empirical value that varies depending on the particles, energies involved, and which biological effects are deemed relevant. It is a set of experimental measurements.
$RBE = \frac{D_X}{D_R}$
where D_X is a reference absorbed dose of radiation of a standard type X, and D_R is the absorbed dose of radiation of type R that causes the same amount of biological damage. Both doses are quantified by the amount of energy absorbed in the cells.

[2] The Oxygen-Enhancement Ratio (OER) is defined as the ratio of radiation doses during lack of oxygen compared to no lack of oxygen for the same biological effect.
$OER = \frac{Radiation\ dose\ in\ hypoxia}{Radiation\ dose\ in\ air}$.

be a considerable advantage in tumor cell killing, particularly for resistant tumor cells.

1.2 Dose deposition and lateral beam shape

Analytically, the Bragg curve is the results of three interactions processes [17]

- *stopping*, that cause the slow down of the particles trough ionization process.
- *scattering*, that mainly affect deflection of the beam from the original direction. The most relevant process is the multiple Coulomb scattering (MCS).
- *nuclear interactions* that cause the fragmentation of the target (and of the projectile in the case of particles heavier than protons) and result in a contribution to the lateral beam broadening and a nuclear fragmentation tail after the peak. In addition this effect cause also a reduction of the beam fluence.

Focusing on the lateral beam shape (on the plane perpendicular to the beam axis), the previous cited effects result in a broader shape, compared to the one expected from the one given by pure electromagnetic calculations.

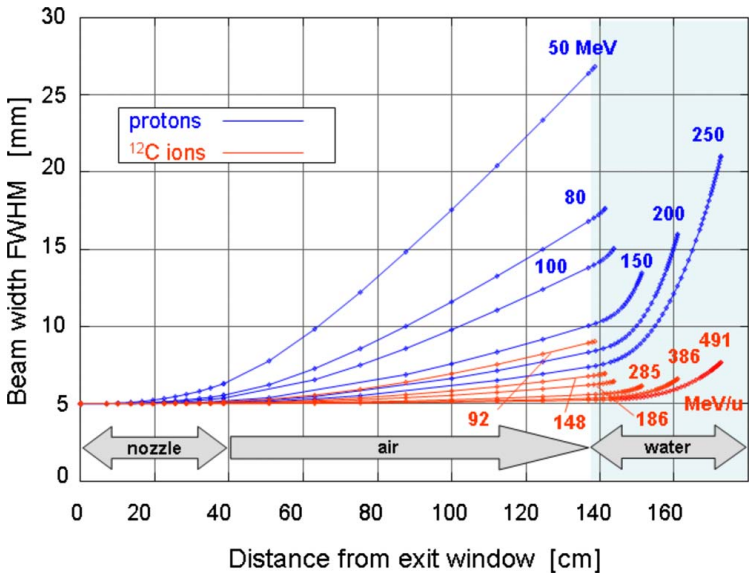

Figure 1.3: Calculated beam spread for protons and ^{12}C ions in a typical treatment beam line. The particle beam is parallel with an initial FWHM (Full Width at Half Maximum) of 5 mm, and passes through the nozzle, including a thin vacuum window and beam monitors and enters a water absorber patient at 1 m distance from nozzle exit.
Figure courtesy of U. Weber, Rhön-Klinikum AG

The angular deflection is mainly due to the *Multiple Coulomb Scattering (MCS)*. In a first approximation, the MCS angular distribution is nearly Gaussian, because

its the sum of many small random deflections; for this reason, the most simple solution nowadays is to approximate it with a Gaussian or a double Gaussian function (See Chap.3)

However, its not exactly Gaussian: the theory does not really apply because large single scatters in the target, though rare, are not quite rare enough [23]. The complete angular distribution has a Gaussian core with a single scattering tail.
The theoretical challenge is to predict the exact form of the MCS angular distribution and to predict its characteristic width as a function of proton energy as well as scattering material and thickness.
Several theories have been published from 1930s [24],[25],[26],[27] but so far the most elegant and accurate theory for incident protons is that of Molière [28] written in German and improved by Bethe [29]; a remarkable effort point of this theory [3] is its validity for any kind of particles and targets (see *Chap.2*).
In clinical practice, a sharp lateral penumbra is essential for sparing critical organs adjacent to the target volume [17]. This happens to be one of the most attractive features of the proton beam. The lateral penumbra achievable in the patient depends on the design of the beam delivery system and also the nature of interaction between protons and tissues in the patient. For scattering, the lateral beam penumbra is affected by the source size and source position, the position of the aperture, the range compensator, the air gap between the compensator and patients body surface, and naturally, the depth of tissue that the beam must penetrate before reaching the target volume.
So, the possibility of modelling and predict the lateral spread of a proton beam is indeed a topic of actual interest, in order to chose the best dose set up that has to be delivered to the patient, and to ensure that the delivered dose is equal to the planned one.

Chapter 2

A non Gaussian model for lateral displacement calculation

In this chapter a new computational model for the calculation of the lateral deflection of a proton pencil beam in water will be presented.
The model is based on the full Molière theory, taking into account the energy loss and the effects of mixtures and compounds. Concerning the electromagnetic part, the model has no free parameters and is in very good agreement with the FLUKA Monte Carlo (MC) code. The effects of the nuclear interactions are parametrized with a two-parameters tail function, adjusted on MC data calculated with FLUKA. The model, after the convolution with the beam and the inclusion of detector response, is in agreement with recent proton data in water from HIT. The model gives results with the same accuracy of the MC codes based on Molière theory, with a much shorter computing time [9].
In the first section of this chapter, the pure electromagnetic Molière theory will be presented, considering also the generalization to compound and mixture and the energy loss process. Thereafter, the explanation of how nuclear interactions are taken into account will follow. The validation of the model's prediction results will be given comparing them with Monte Carlo simulation and experimental data. To complete the treatise, a generalization in 2D plan will be evaluated.

2.1 Electromagnetic core: Molière theory

Particles passing through matter suffer repeated elastic Coulomb scattering from nuclei although with a lower probability. Considering that, a considerable number of nuclei have a greater mass than the incoming particles, the energy transfer is negligible, but each scattering center adds a small deviation to the incoming particles trajectory. Even if this deflection is small the sum of all the contribution adds a random component to the particle's path which proceeds with a zig-zag path Fig.2.1. As a result, an incoming beam after a thickness of material shows a divergence greater than the initial one.

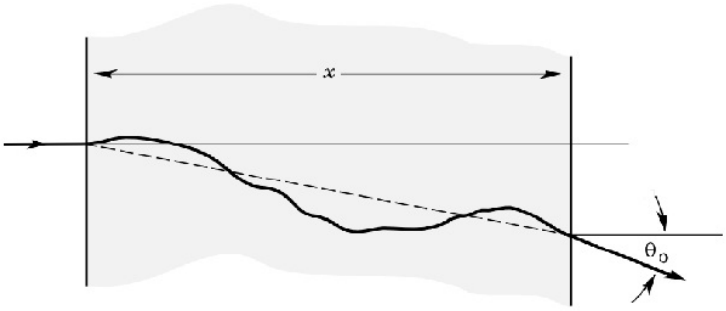

Figure 2.1: Effect of Multiple Coulomb Scattering

Three situations can be considered:

1. *Single scattering.* When the thickness is extremely small and the probability to have more than one interaction is negligible. This situation is well described by the Rutherford formula [30].

2. *Plural scattering.* When the number of Coulomb scattering increases but remains under few tens of interactions [31].

3. *Multiple scattering.* When the thickness increases and the number of interactions become high; the angular dispersion in a first approximation can be modeled as Gaussian.

In an hadrontherapy contest the most common situation is for sure the multiple scattering, since the considered depths are within human body scale. It is the main process that causes the beam broadening and the lateral beam shape, so it is important to carefully evaluate it since it mainly affects the final lateral beam shape (with nuclear tails addiction, see 2.2) in a treatment plan.
The expression of angular distribution is not known exactly in a closed functional

form. However, some theories derive a set of formulae, usually obtained in the framework of transport theory, that can be computed numerically. Here we use the MCS Molière's theory.

Many numerical analyses and comparisons with data ([32], [33]) have shown that the Molière theory [28] describes very well the MCS for protons at energies below $1\,GeV$ and that in this energy range it is completely equivalent to others more recent approaches [34].

In order to provide a mathematical formulation of the problem, let us initially ignore the energy loss of the incident particle and assume that the target is of a homogeneous material. The theory is based on the standard transport equation, the Bessel transforms and the small angles approximation ($\sin\theta \backsim \theta$).

In order to define the problem, first the two main angles are introduced as (see Fig.2.2):

- χ, which stands for the net angle after a single scattering event
- θ, which is the total angle after multiple scattering events occur traversing a thickness t

If z is the incident beam direction, the MCS of a particle passing through a target of thickness t can be expressed as a function of the particle angle θ, with respect to z.

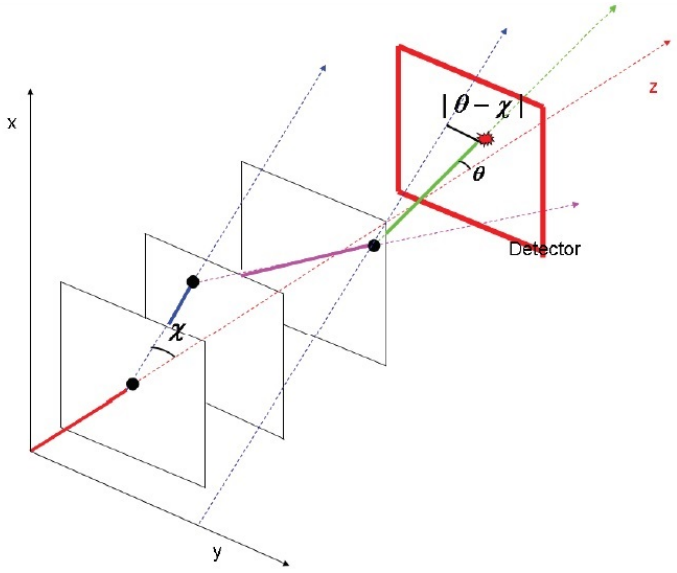

Figure 2.2: Schematic representation of the two main angles of the theory, χ and θ.

The target is described as an homogeneous media of thickness $t(cm)$ and volume number density $N(\text{atoms/cm}^3)$.

Now, the standard transport equation is applied to the number of particles in the angular interval $d\theta$ after a path of t:

$$\frac{\partial f(\theta,t)}{\partial t} = -Nf(\theta,t)\int \sigma(\chi)\chi \mathrm{d}\chi + N\int f(|\hat{\theta}-\hat{\chi}|,t)\sigma(\chi)\chi \mathrm{d}\chi \qquad (2.1)$$

where $\sigma(\chi)\chi \mathrm{d}\chi$ is the differential scattering cross section into the angular interval $\mathrm{d}\chi$ centred around the angle χ, $|\hat{\theta}-\hat{\chi}|$ is the vector in the plane that represents the direction of the particle before the last scattering and $\mathrm{d}\hat{\chi}$ can be expressed as $\mathrm{d}\hat{\chi} = \frac{\chi \mathrm{d}\chi \mathrm{d}\phi}{2\pi}$ where ϕ stands for the azimuth of the vector $\mathrm{d}\chi$ in the plane.

The function is separable in polar coordinates and is circularly symmetric, so to solve Eq.2.1 Bessel transforms are applied:

$$f(\theta,t)=\int_0^\infty \eta \mathrm{d}\eta J_0(\eta\theta)F(\eta,t) \tag{2.2}$$

obtaining

$$F(\eta,t)=\int_0^\infty \theta \mathrm{d}\theta J_0(\eta\theta)f(\theta,t) \tag{2.3}$$

where $J_0(\eta\theta)$ is the Bessel function of zero order.
The Bessel transform of order zero is essentially the 2-dimensional Fourier transform of a circularly symmetric function. With no loss of generality, the two dimensional space can be described in polar coordinate system (r,θ), therefore the Fourier transform is now written in these polar coordinates as the integral on θ of the Bessel function:

$$F(k)=\int_{r=0}^\infty \mathrm{d}r\int_{\theta=0}^{2\pi}\mathrm{d}\theta f(r,\theta)e^{i\hat{k}\hat{r}}=\int_{r=0}^\infty \mathrm{d}r\int_{\theta=0}^{2\pi}\mathrm{d}\theta f(r)e^{ikr\cos(\theta)} \tag{2.4}$$

The relation between $F(k)$ and $f(r)$ in terms of J_0 is obtained by integrating on θ:

$$F(k) = 2\pi\int r\mathrm{d}r f(r)J_0(kr) \tag{2.5}$$

$$f(r) = \frac{1}{2\pi}\int k\mathrm{d}k F(k)J_0(kr) \tag{2.6}$$

Now the convolution theorem can be applied on the Bessel transform; it ensures that the Bessel transform of the convolution of two functions is equal to the product of the Bessel transforms of the functions. Let $h(y)$ be the convolution between two generic functions $f(x)$ and $g(x)$:

$$h(y)=f(x)*g(x)=\int f(|\hat{y}-\hat{x}|)g(x)d\hat{x} \tag{2.7}$$

the Bessel Transform of $h(x)$ is:

$$H(\eta)=\int \mathrm{d}x\mathrm{d}y f(|\hat{y}-\hat{x}|)g(x)e^{-2\pi i(\hat{y}\cdot\hat{\eta})} \tag{2.8}$$

by defining $\hat{t}=\hat{x}-\hat{y}$ Eq.2.8 becomes:

$$H(\eta) = \int \mathrm{d}x g(x)\left(\int \mathrm{d}t f(t)e^{-2\pi i(\hat{x}+\hat{t})\cdot\eta}\right) \tag{2.9}$$

$$= \int \mathrm{d}x g(x)e^{-2\pi i(\hat{x}\cdot\hat{\eta})}\left(\int \mathrm{d}t f(t)e^{-2\pi i(\hat{\eta}\cdot\hat{t})}\right) \tag{2.10}$$

$$= G(\eta)F(\eta)$$

Based on the Molière's calculation, the following identity can be expressed:

$$\int f(|\hat{x}-\hat{y}|)g(y)d\hat{y}=\int_0^\infty G(y)F(y)J_0(xy)\mathrm{d}y \tag{2.11}$$

The result of the convolution theorem can be applied to the second term of Eq.2.1:

$$\begin{aligned}\frac{\partial F(\eta,t)}{\partial t} &= -NF(\eta,t)\int \sigma(\chi)\chi \mathrm{d}\chi + NF(\eta,t))\int \sigma(\chi)J_0(\eta\chi)\mathrm{d}\hat{\chi} \\ &= -NF(\eta,t)\int [1-J_0(\eta\chi)]\,\sigma(\chi)\chi\mathrm{d}\chi\end{aligned} \tag{2.12}$$

and integrating t, the following expression is obtained

$$F(\eta,t) = e^{\Omega(\eta)-\Omega_0} \tag{2.13}$$

with

$$\Omega(\eta) = Nt\int_0^\infty \sigma(\chi)\chi\mathrm{d}\chi J_0(\eta\chi) \tag{2.14}$$

and $\Omega_0 = \Omega(0)$ is the total number of collision.

Finally the solution of Eq.2.1 is obtained inserting Eq.2.2 in the antitransform of 2.13

$$f(\theta,t) = \int_0^\infty \eta\mathrm{d}\eta J_0(\eta\theta)e^{\left[-Nt\int_0^\infty \sigma(\chi)\chi\mathrm{d}\chi(1-J_0(\eta\chi))\right]} \tag{2.15}$$

It is mandatory to point out that this solution is exact for any scattering law under the assumption of small angle approximation.

At this point, referring to Eq.2.15, Molière sets

$$Nt\sigma(\chi)\chi\mathrm{d}\chi = \frac{2\chi_c^2\chi\mathrm{d}\chi q(\chi)}{\chi^4} \tag{2.16}$$

where q stands for the ratio between the real and the Rutherford scattering, and χ_c is the *characteristic single scattering angle*, which is one of the two main parameters of this theory, it is connected to the RMS of the scattering angle and it will be described hereafter.

The equivalence in Eq.2.16 is based on the consideration that the σ, for scattering cross section from atoms, decreases rapidly for large χ and follows the Rutherford law $\frac{1}{\chi^4}$, whereas is complicated by the electron screening effect, only for angles of the order of:

$$\chi_0 = \frac{\hbar}{p\cdot a} = \frac{\hbar}{p}\frac{Z^{1/3}}{0.885a_0} \sim 4.216\cdot 10^{-6}\frac{Z^{1/3}}{p} \tag{2.17}$$

where $\hbar/p = \lambda_e = 2,43\cdot 10^{-12}$ is the de Broglie wavelength of electrons, a the Fermi radius, Z the atomic number number of the target[1] and $a_0 \equiv \frac{\hbar^2}{m_e c^2} = 0.52918\cdot 10^{-8} cm$, the Bohr radius. The ratio $q(\chi)$ is 1 for large χ and decreases to zero at $\chi = 0$ where the main drop occurs.

[1] In all this work, capital letter for atomic and mass number will be referred to the target, instead letters will refers to the incident particle.

2.1.1 Derivation of the crucial parameters

The first factor is the *characteristic single scattering angle* χ_c introduced in Eq.2.16; it represents the independent angle part of the Rutherford cross section. The total probability of single scattering through an angle greater than χ_c is equal to one (that means that it takes into account the RMS of the angle).
Its expression can be written as

$$\chi_c^2 = \frac{4\pi \left(\frac{e^2}{\hbar c}\right)^2 (\hbar c)^2 \varrho Z^2 z^2}{p^2 \beta^2} \tag{2.18}$$

where $\varrho = Nt$ is the surface number density.
By introducing the target mass thickness $x = \rho t \, (g/cm^2)$ and the equivalence $Nt = N_A x/A$ with the usual meaning of the symbols, this equation can be rewritten as

$$\begin{aligned} \chi_c^2 &= \frac{4\pi N_A \frac{x}{A} Z^2 z^2 e^4}{p^2 v^2} \\ &= 0.1569 \cdot 10^{-6} \frac{x}{A} \frac{Z^2 z^2}{p^2 \beta^2} \end{aligned} \tag{2.19}$$

with $p \, (GeV/c)$ is the momentum and $e^2/\hbar c \sim 1/137$ is the fine structure constant.
Now, taking the logarithm of Eq.2.13 and inserting Eq.2.16 in Eq.2.14 the following formula is obtained:

$$\begin{aligned} -\ln F(\eta, t) &= \Omega_0 - \Omega(\eta) \\ &= 2\chi_c^2 \int_0^\infty \chi^{-3} \mathrm{d}\chi \, [1 - J_0(\chi\eta)] \, q(\chi) \end{aligned} \tag{2.20}$$

Here Molière made a fundamental consideration; he realized that this integral can be calculated considering that the important values of η will be at least of the order $1/\chi_c$ and q becomes appreciably different from 1 only for $\chi \sim \chi_0 \ll \chi_c$ where χ_0 is the screening parameter of Eq.2.17. This leads to the possibility of splitting the integral at certain angle k like:

$$\chi_0 \ll k \ll 1/\eta \sim \chi_c \tag{2.21}$$

and so, in Eq.2.20,

$$\int_k^\infty \chi^{-3} \mathrm{d}\chi \, [1 - J_0(\chi\eta)] \, q(\chi) = \int_k^\infty \chi^{-3} \mathrm{d}\chi \, [1 - J_0(\chi\eta)] \cdot 1$$

and for the other part of the integral $\int_0^k$ the argument of the Bessel function is small and it is performed the substitution $1 - J_0(\chi\eta) = \frac{1}{4}\chi^2\eta^2$.
With this considerations, Molière defined the second main parameter of this theory, *the characteristic screening angle* χ_a as:

$$-\ln \chi_a = \lim_{k \to \infty} \left[\int_0^k q(\chi) d\chi/\chi + 1/2 - \ln k \right] \tag{2.22}$$

From this definition, Molière obtained [29]:

$$\Omega_0 - \Omega(\eta) = \frac{1}{4}\chi_c^2\eta^2\left[b - \ln\left(\frac{1}{4}\chi_c^2\eta^2\right)\right] \tag{2.23}$$

$$= \frac{1}{2}\chi_c^2\eta^2\left(-\ln(\chi_a\eta) + 0.616\right) \tag{2.24}$$

where b represents the natural logarithm of the effective number of collisions in the target, and is defined as

$$b = \ln\left(\frac{\chi_c^2}{\chi_a^2} - 0.154432\right) \tag{2.25}$$

$$= \ln\Omega_0 - 0.154432$$

In order to simplify Molières fundamental equation 2.15, a new variable $y = \eta\chi_c$ is defined, and Eq.2.23 is inserted in the Eq. 2.13:

$$f(\theta)\theta\mathrm{d}\theta = \frac{\theta\mathrm{d}\theta}{\chi_c^2}\int_0^{y=\Gamma}\mathrm{d}yJ_0\left(\frac{\theta\cdot y}{\chi_c}\right)\exp\left[-\frac{y^2}{4}\left(b - \ln\left(\frac{y^2}{4}\right)\right)\right]y \tag{2.26}$$

This is called Molière's transformed equation. The motivation for evaluating the integral only until $y = \Gamma$ can be found in [29].

One fundamental result of Molière's Theory is that the scattering is described by a single parameter: the screening angle χ_a and the angular distribution depends only on the ratio χ_a/χ_c. Also, the distribution function $f(\theta)$ is independent of the shape of the differential cross section $\mathrm{d}\sigma$, and only the final form of the function $f(\theta)$ depends on the form of $\sigma(\theta)$. The general assumption is

$$\varrho\sigma(\chi) = 2\chi_c^2 Q(\chi) \tag{2.27}$$

where $Q(\chi)$ is the angular part of $\sigma(\chi)$.

The explicit form of $Q(\chi)$ can be obtained assuming a screened Coulomb potential in the Born approximation [35]:

$$V(r) = \left(\frac{zZe^2}{r}e^{-\mu\lambda_0 r}\right) \tag{2.28}$$

where $\lambda_0 = \frac{Z^{1/3}}{0.468\cdot 10^{-8}}$ is the reciprocal of the Fermi radius $a[cm]$, and $a_0 = \frac{\hbar^2}{m_e c^2} = 0.52918\cdot 10^{-8}\,cm$ is the Bohr radius.

So,

$$Q(\chi) = \frac{1}{(\chi^2 + \chi_a^2)^2} = \frac{1}{(\chi^2 + (\mu\chi_0)^2)^2} \tag{2.29}$$

within this formula, the electrons screening is taken into account by χ_a.

The main parameters are related as in the following equation:

$$\begin{aligned} \chi_a^2 &= \mu^2 \chi_0^2 \\ \mu^2 &= \left(1.13 + 3.76 \frac{z^2 Z^2}{137^2 \beta^2}\right) \end{aligned} \tag{2.30}$$

To obtain an easier evaluation of $f(\theta)$, Molière replaces the exponential factor of $V(r)$ with a function, derived from the Thomas-Fermi theory given by a sum of three exponentials [29]. Furthermore, to determine the screening angle χ_a, Molière used his original calculation of the single scattering by a Thomas-Fermi potential and the solution was realized by means of the Wentzel−Kramers−Brillouin method[1] instead of Born approximation (the final formula for the differential cross section is numerical and only approximate). Once the final form of the differential cross section has been obtained, to evaluate the total number of collisions, Molière makes two considerations:

1. Since the scattering angle χ_c is connected to the RMS of the scattering angle, taking into account the integral of Eq.2.27 and 2.29, the number of collisions in a finite target leading to deflections in a given range of χ is

$$\int_0^{2\pi} \int_{\chi_c}^{\infty} \sigma(\chi) \chi \mathrm{d}\Omega = 1 \tag{2.31}$$

   This quantity can be easily evaluates if $\chi_a \ll \chi_c$, which is true for any physical target thickness.

2. In Eq.2.29, χ_a is a cut-off angle, due to screening of nuclear charge by orbital electrons; that, for distant collisions, eliminates the divergency as the $1/\chi^4$ law, .

   So for large χ the scattering from atoms is characterized by the rapid decrease of σ, and it becomes complicated if $\chi \sim \chi_0$

So, the total number of collisions is given by:

$$\begin{aligned} \varrho \int_0^{\infty} \sigma(\chi) \chi \mathrm{d}\chi &= \int_0^{\infty} 2\chi_c^2 \frac{\chi}{(\chi^2 + \chi_a^2)^2} \mathrm{d}\chi \qquad (2.32) \\ &= \frac{\chi_c^2}{\chi_a^2} \equiv \Omega_0 \qquad (2.33) \end{aligned}$$

The main points of this theory are the following:

[1] Wentzel−Kramers−Brillouin (WKB) is a method for finding approximate solutions to a time-independent one-dimensional differential equation with spatially varying coefficients.

- the scattering is described by just a single parameter, the screening angle χ_a^2
- the angular distribution depends only on the ratio between χ_a/χ_c, the screening angle to the scattering angle
- The distribution function $f(\theta)$ is insensitive to the differential cross section $\mathrm{d}\sigma$ provided that $\mathrm{d}\sigma$ goes over into Rutherford law for large angles.

2.1.2 Projected angle distribution

Based on these results, the projected angle θ_x can be evaluated to predict the particles distribution on the projected plane, perpendicular to the beam direction. By geometrically projecting Molières transformed equation 2.26, the following distribution is obtained [36]:

$$f(\theta_x)\mathrm{d}\theta_x = \frac{\mathrm{d}\theta_x}{\pi\chi_c^2}\int_0^\Gamma \cos\left(\frac{\theta_x y}{\chi_c}\right)\exp\left[-\frac{y^2}{4}\left(b-\ln\left(\frac{y^2}{4}\right)\right)\right]\mathrm{d}y \tag{2.34}$$

and, in the small angle approximation, the relation between the projected angles in the traverse plane xy and the spatial angle is a geometric construction

$$\theta = \sqrt{\theta_x^2+\theta_y^2} \tag{2.35}$$

Now, setting $x = \vartheta^2$, y is changed in $u = B^{1/2}y$, and the distribution function is expanded in a power series in $1/B$ as

$$f(\theta)\theta\mathrm{d}\theta = \vartheta\mathrm{d}\vartheta\left[f^{(0)}(\vartheta)+B^{-1}f^{(1)}(\vartheta)+B^{-2}f^{(2)}(\vartheta)+...\right] \tag{2.36}$$

and using characteristic multiple scattering angle

$$f(\theta) = \frac{1}{2}\cdot\frac{1}{2\pi\theta_M^2}\left[f^{(0)}(\vartheta)+B^{-1}f^{(1)}(\vartheta)+B^{-2}f^{(2)}(\vartheta)+...\right] \tag{2.37}$$

where:

- $f(\vartheta)^n$ is expressed as

$$f(\vartheta)^n = \frac{1}{n!}\int_0^{\inf} u\mathrm{d}uJ_0(\vartheta u)e^{-\frac{u^2}{4}}\left[\frac{u^2}{4}\ln\left(\frac{u^2}{4}\right)\right]^n \tag{2.38}$$

- $f^{(0)}(\vartheta)$ is a Gaussian distribution of θ_M standard deviation

$$f^{(0)}(\vartheta) = 2e^{-\vartheta^2} = 2\exp\left(-\frac{\theta}{\chi\sqrt{B}}\right)^2 = 2\exp\left(-\frac{\theta}{\sqrt{2}\theta_M}\right)^2 \tag{2.39}$$

- $f^{(1)}(\vartheta)$ has the following form

$$f^{(0)}(\vartheta) = 2e^{-x}(x-1)[\overline{Ei}(x)-\ln x]-2(1-2e^{-x}) \tag{2.40}$$

  where $\overline{Ei}$ is the exponential integral function.

This functions have a behaviour of the type

$$\vartheta > 2 \Rightarrow f^{(1)}(\vartheta) > f^{(0)}(\vartheta)$$

instead

$$\begin{aligned} \text{for } \vartheta >> 1 \quad &\Rightarrow \quad f^{(0)}(\vartheta) \sim -e \\ &\Rightarrow \quad f^{(1)}(\vartheta) \sim 2\vartheta - 4 \\ &\Rightarrow \quad f^{(2)}(\vartheta) \sim \vartheta - (2n+2) \end{aligned} \tag{2.41}$$

This last statement leads the series 2.37 to converge even faster at large ϑ than at little ones; so $f^{(0)}(\vartheta) + B^{-1} f^{(1)}(\vartheta)$ is a good approximation for the distribution at any angle.

Since x and y are independent, and the media is homogeneous, it can be assumed without losing generality, that θ_x and θ_y have the same distribution (so, the same mean square) and the mean square angles relation is

$$\langle \theta^2 \rangle = 2\langle \theta_x^2 \rangle \tag{2.42}$$

Considering that the distribution in Eq. 2.34 can be divided into a Gaussian core shape and an additional tail term, in the precedent equation a Gaussian RMS can be introduced as:

$$\theta_R \equiv \sqrt{\langle \theta^2 \rangle} = \chi_c \sqrt{B} \tag{2.43}$$

where B is the solution of the equation

$$B - \ln B = b \tag{2.44}$$

and it can be approximated with the Scott formula [36] based on the total number of collisions obtained in Eq.2.32:

$$B = 1.153 + 1.122 \ln \Omega_0 \tag{2.45}$$

This approximation is valid within $2 - 3\%$ and so, B is linearly related to b in the region of interest.

With these relations, the connection between the RMS of the space angle and the projected one can be written as:

$$\theta_{xR} = \frac{\theta_R}{\sqrt{2}} = \frac{\chi_c \sqrt{B}}{\sqrt{2}} \tag{2.46}$$

For a matter of usefulness, the total angular distribution is expressed in terms of a reduced angle variable ϑ that is the angle measured in unit of $\chi_c \sqrt{B}$

$$\vartheta = \frac{\theta}{\chi_c \sqrt{B}} \tag{2.47}$$

.

2.1.3 Compound and mixture generalization

Since the theory is valid for any kind of particle and media, let us generalize this equations for the case of mixtures and compounds, and in particular for the example of a water molecule (a motivation to chose water molecule as reference material to validate the model, is that currently in clinical practice each human tissue is expressed in water equivalent tissue). The equation of χ_c and χ_a now will extended from a single atom to a sum of n_i constituents of Z_i atomic numbers and A_i atomic mass. So, for a water molecule

$$\begin{aligned} Z_M &= \sum_i n_i Z_i = 10\,, \\ A_M &= \sum_i n_i A_i = 18 \end{aligned} \tag{2.48}$$

Equation 2.19 becomes:

$$\chi_c^2 = \sum_i \chi_{ci}^2 = \chi_W^2 \frac{x}{p^2\beta^2} \tag{2.49}$$

where χ_W^2 is the the energy loss independent part (see Sec.2.1.4) given by

$$\chi_W^2 = 0.1569 \cdot 10^{-6} \frac{z^(2Z_H^2 + Z_O^2)}{A_M} \tag{2.50}$$

with $Z_H = 1$, $Z_O = 8$.

The generalization of χ_a is not so easy because the logarithmic function of the Bessel transform of the cross section, i.e. that gives the effective number of events, depends both on $\ln \chi_a^2$ and χ_c^2 as reported in Eq.2.23:

$$\ln \chi_a^2 = \frac{1}{\chi_c^2} \sum_i \chi_{ci}^2 \ln \chi_{ai}^2 \tag{2.51}$$

where χ_c^2 and χ_{ci}^2 are defined in Eq.2.49, χ_{ai}^2 are calculated from 2.59 substituting $Z = Z_i$, $i = H$, O, $Z_H = 1$, $Z_O = 8$.

If a molecule is considered, another correction has to be performed; effectively the incident particle is scattered by atomic electrons as well as by the screened Coulomb field of the nucleus. To consider this, the Fano's solution [33],[37] is applied, which requires the modification of equation 2.51 as:

$$\ln \chi_a^2 = \frac{1}{\chi_c^2} \sum_i \chi_{ci}^2 \left(\ln \chi_{ai}^2 - \frac{D_i}{Z_i} \right) \tag{2.52}$$

with (2.53)

$$D_i = \ln \left(\frac{1130}{Z_i^{4/3} \left(\frac{1}{\beta^2} - 1 \right)} \right) + u_i - \frac{\beta^2}{2}$$

where D_i is the Fano correction [36],[37] $u_H = 3.6$ and $u_O = 5.0$ (these values are calculated based on [37]).

At this point the total angular distribution of particles passed through a thickness x has been obtained and a closed formula is given even for the projected angle, as for the spatial angle.

This result is valid for any kind of mixture and component. Now it has to be considered that in hadrontherapy the above-mentioned thickness is a considerable path in human body, so this ideal equations have to be modified to take into account the energy loss process.

2.1.4 Energy loss

To include the energy loss process in the theoretical formulation, one has to consider that both χ_c and χ_a parameters explicitly depend on the quantity $p\beta$. So, the problem can be solved if one finds the dependence of these quantities on the water thickness x traversed. Defining $p(x)$ and $\beta(x)$ the current values at the depth x in the target Eq.2.49, we have:

$$\chi_c^2 = \chi_W^2 \int_0^x \mathrm{d}t \frac{1}{p^2(t)\beta^2(t)} \tag{2.54}$$

The value of $p(x)\beta(x)$ for charged particle of initial momentum $p\beta$, after traversing a thickness x, is given by [38]:

$$(p(x)\beta(x))^2 = p^2\beta^2 \left(1 - \frac{x}{R}\right)^k \tag{2.55}$$

where R is the range for that particle of incident momentum p, and k is a parameter evaluated using Schneider formulae [39] as :

$$k = 1.0753 + 0.12e^{-0.09\rho \mathrm{X}_0} \tag{2.56}$$

This formula is fairly accurate for many materials of density $\rho(g/cm^3)$ and radiation length $X_0(cm)$. The accuracy has been tested up to a distance of $0.99 \cdot R$ resulting to be within 2% both for protons and carbon ions.

To provide a completely analytical evaluation of the range R, in Eq.2.55, a very accurate formula is used, based on [40]

$$R(cm) = \frac{1}{\rho}\frac{A_M}{Z_M}\sum_{n=1}^{N} \alpha_n E_I^{p_n} E_k^n \tag{2.57}$$

where $E_k(MeV)$ is the incident kinetic energy, $E_I(eV)$ the mean ionization potential of the medium and A_M, Z_M are the result of 2.48. This model has been tested with $E_I = 77.0$eV as suggested in [41]. For water and protons of incident kinetic energy

order	α_i	p_i
1	6.84690e-04	0.4002
2	2.26769e-04	0.1594
3	-2.46100e-07	0.2326
4	1.42750e-10	0.3264

Table 2.1: Parameters used for the range calculations of Eq.2.57

$E_k < 300$ MeV, a sum with $N = 4$ gives results accurate to a more than 0.5% [40]. The coefficients α_i and p_i are reported in Tab. 2.1.

So, inserting the range formula given by Eq.2.57 in Eq.2.54 the following equation is obtained:

$$\begin{aligned} \chi_c^2 &= \chi_W^2 \frac{1}{p^2\beta^2} \int_0^x \frac{1}{\left(1-\frac{t}{R}\right)^k} \mathrm{d}t \\ &= \chi_W^2 \frac{R[(1-x/R)^{1-k}-1]}{(k-1)\cdot p^2\beta^2} \end{aligned} \tag{2.58}$$

This is the form of χ_c parameter valid for any compound taking into account the energy lost after a thickness x.

The calculation of χ_a is much more complicated and cannot be obtained in closed form. Applying equations 2.55 to the general form of χ_a in Eq. 2.51,2.50, the following equation is obtained:

$$\ln \chi_a^2 = \frac{1}{\chi_c^2} \frac{0.1569 \cdot 10^{-6} z^2}{A_M} \sum_i \frac{n_i Z_i^2}{p^2\beta^2} \int_0^x \frac{\ln[\mu_i^2 \chi_{0i}^2] - \frac{D_i}{Z_i}}{\left(1-\frac{t}{R}\right)^k} \mathrm{d}t \tag{2.59}$$

where A_M is from Eq.2.48, μ_i is a function of $\beta(x)$ and χ_{0i} is a function of $p(x)$. They can be calculated using Eq.2.17, 2.59 with $Z_i = Z_H, Z_O$ and χ_c from Eq.2.58. This formula can be evaluated with good precision with the Simpson numerical integration rule because of the smooth behaviour of the integrand. In water, integration steps of $0.5\,cm$ are enough to provide good accuracy. Since μ_i and χ_{0i} depend on p and β separately, we have to calculate them from the current product $p(x)\beta(x)$ resulting during the numerical integration.
Starting from the known product $p(x)\beta(x) \equiv \omega$ from Eq.2.55:

$$
\begin{aligned}
p(x)\beta(x) \equiv \omega &= \frac{p^2(x)}{E_x} = \frac{E_x^2 - m^2}{E_x} \\
&\downarrow \\
E_x^2 - \omega E_x &- m^2 = 0 \\
&\downarrow \\
E_x = \frac{1}{2}\,(\quad \omega &+\sqrt{\omega^2 + 4m^2})\ , \qquad (2.60)
\end{aligned}
$$

$$
p(x) = \sqrt{E_x^2 - m^2} \quad , \quad \beta(x) = \frac{p(x)}{E_x}\ . \qquad (2.61)
$$

where E_x is the relativistic total energy of the projectile.

2.1.5 Lateral displacement

So far, the angular distribution of an incident beam that passes a layer of any kind of mixture is obtained, taking into account also energy loss effect in addition to the pure Molière distribution.

At this point it is useful to obtain a general formula, that permits the passage from the angular to the spatial displacement. By referring to Fig.2.3, the RMS y_M of the transverse displacement on a measuring plane at distance x due to a layer t is given by $(x - t)\theta_{xR}$, where the angle is given by Eq.2.46.

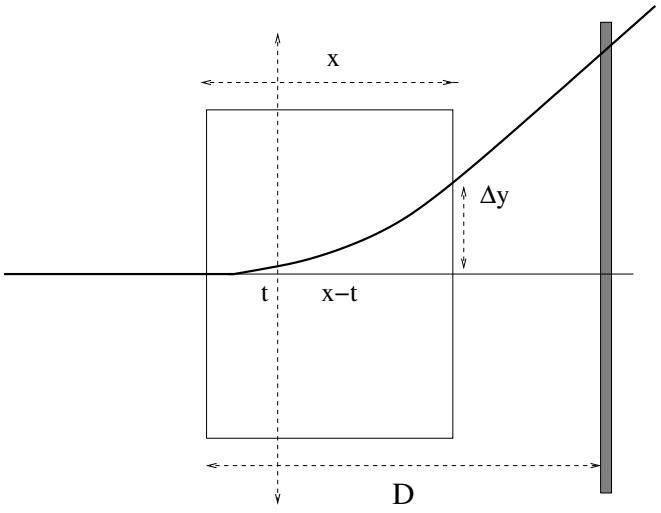

Figure 2.3: Schematic view of lateral displacement y_M of the angular distribution on the transverse plan.

As it explicitly stands, the angular squared rms is a product of $\chi_c^2\ \sqrt{B}$. The first argument depends on the thickness x, while the second one depends on the thickness in a logarithmic way. This fact is inevitable and is present in many formula that

calculate the angular rms, as in the Highland [42] one.
What is the physical meaning?
Physically, it means that two successive layers act in a dependent manner, because the second layer receives trajectories deflected by the first one.
Based on this consideration, the usual Gottschalk procedure [33] is applied, so χ_c^2 contributions are combined in quadrature, and multiplied for an average value of B.

Taking into account the energy loss from equations 2.54-2.58, considering 2.46,2.49 and replacing $x \to \int \mathrm{dt}$, than by adding in quadrature all the χ_c^2 contributions, for a thickness x and a detector plane placed at a distance $D \geq x$, we obtain:

$$y_M = \frac{\chi_W \sqrt{B}}{\sqrt{2} p\beta} \left[\int_0^x \frac{(D-t)^2}{\left(1 - \frac{t}{R}\right)^k} \mathrm{dt} \right]^{1/2} \tag{2.62}$$

The B contribution is calculated from equation 2.44 with the final values of χ_c^2 and χ_α^2 from equations 2.58 and 2.59. From equation 2.45, this corresponds to the use of the mean number of collisions, taking into account all the relevant processes.
A more common case is the one in which it is necessary to find the displacement at the plane of distance x, and to obtain such result it is sufficient replace the term $D - t$ in the integrand with $x - t$.
When $D = x$, *Microsoft Mathematics* gives a rather simple analytical solution for the integral in Eq.2.62:

$$y_M = \frac{R^2[2R(1-x/R)^{3-k} - 2kx + 6x - 2R]}{(k-1)(k-2)(k-3)} - \frac{Rx^2}{k-1} \ , \quad k > 1 \ . \tag{2.63}$$

Other more complicated analytical expressions can be found when $x < D \leq R$ and $D > R$.

So, the RMS from Eq.2.62 corresponds to the RMS of the projection on the measuring plane of the RMS θ_{xR} from Eq.2.46 of the Gaussian core of the angular distribution. Therefore, the factor

$$\delta = \frac{y_M}{\theta_{xR}} = \frac{y_M \sqrt{2}}{\chi_c \sqrt{B}} \tag{2.64}$$

$$= \int_0^x \frac{(z-t)^2}{(1-t/R)^k} \, \mathrm{d}t \Big/ \int_0^x \frac{1}{(1-t/R)^k} \, \mathrm{d}t \ . \tag{2.65}$$

represents the scale factor that allows the passage from the angular to the spatial distribution observed after the passage of a thickness x. The change of variable therefore is

$$\delta = \frac{y}{\theta_x} \quad \to \quad \theta_x = \frac{y}{\delta} \ , \tag{2.66}$$

and Eq.2.34 becomes

$$f_M(y) = \frac{1}{\pi \chi_c \delta} \int_0^\Gamma \cos\left(\frac{y\eta}{\chi_c \delta}\right) \exp\left[-\frac{\eta^2}{4}\left(b - \ln\frac{\eta^2}{4}\right)\right] \mathrm{d}\eta \tag{2.67}$$

2.2 Nuclear effects

So far a completely analytical formulation is obtained to describe the pure electromagnetic part of the multiple scattering process. The obtained equations predict the electromagnetic particle distribution both in the spatial angle and on the transverse plan after traversing a slab x; they are valid for any particles and any kind of compound and mixture, without the use of free parameters.
But in order to have an evaluation of the distribution of the particles in the matter when large thicknesses are involved, as in the case of hadrontherapy, nuclear interactions have to be taken into account. Since this work is performed for proton in water, the only fragmentation of the target will be considered (on the contrary, if one want to deal with carbon ions, also the projectile fragmentation has to be taken into consideration).
So,to complete the Molière distribution, an additional term is added. This term describes the interaction of non primary particles that affect the tails and accounts for the primary protons fluence decrease. This effect plays an important role, since the nuclear reactions cause a decrease of the primary proton fluence with about 1% per cm of depth [12].

Potential scattering, which induces transitions between different states of the nucleus, is the dominant process for protons. However at therapeutic energies ($E <$ 300 MeV), a minor contribution arises also from nuclear reactions that results in the production of secondary particles and heavy recoils.
In the case of protons in water, the total nuclear cross-section for proton$-$nucleus interactions is often calculated only taking into account the $p -^{16} O$ reactions [12]. The main reactions induced by protons on Oxygen, as Ulmer suggests, are:

$$\begin{aligned}
p + {}^{16}_{8}O &\Rightarrow n + {}^{16}_{9}F \\
p + {}^{16}_{8}O &\Rightarrow p + n + {}^{15}_{8}O \\
p + {}^{16}_{8}O &\Rightarrow p + p + {}^{15}_{7}N \\
p + {}^{16}_{8}O &\Rightarrow \alpha + {}^{13}_{7}N \\
p + {}^{16}_{8}O &\Rightarrow d + {}^{15}_{8}O \\
n + {}^{16}_{8}O &\Rightarrow p + {}^{16}_{7}N \\
n + {}^{16}_{8}O &\Rightarrow p + n + {}^{15}_{7}N
\end{aligned} \tag{2.68}$$

Considering these reactions Ulmer [12] provides a formula for the determination of the percentage W_p of events *without* nuclear interactions (primary protons), as a

function of the traversed thickness, for protons of incident kinetic energy E_k and range R in water, at a distance water thickness x:

$$W_p = \frac{1}{2}\left[1 - \left(\frac{E_k - E_{th}}{m}\right)^f \frac{x}{R}\right]\left[1 + \mathrm{erf}\left(\frac{R-x}{\tau}\right)\right] \ , \tag{2.69}$$

where erf is the error function, f is a parameter of value $f = 1.032$, $m(MeV)$ is the proton mass, $E_{th} = 7\,MeV$ is the ^{16}O threshold energy of the Coulomb barrier.

The parameter τ takes into account the range variation due to the straggling along the beam path and can be parametrized as [40]

$$\begin{aligned} \tau &= 0.0179651452 \cdot R^t \\ &\text{where} \\ t &= \begin{cases} 0.9352 & \text{if } R \geq 1\text{cm} \\ 1.1763 & \text{if } R < 1\text{cm} \end{cases} \end{aligned} \tag{2.70}$$

This formula has been implemented in the GEANT4 code [43] and is used for protons with $E_k < 300\,MeV$. It gives approximatively a linear decrease, which reaches about 78% at a depth of 40 cm for $E_k = 300\,MeV$, followed by a sharp fall-off to zero within a range of about $1\,cm$, determined by the straggling parameter τ.

Once the weight of the nuclear interactions has been parametrized, its influence on the secondary build up contribution has to be described, to evaluate the total energy lateral deposition.

As Soukup suggests [6], a Cauchy-Lorentz distribution is used to parametrize the nuclear tail contribution:

$$t(x) = \frac{1 - A\exp\left[-\frac{x^2}{2b^2\sigma_n^2}\right]}{\pi b\left(\frac{x^2}{b^2} + 1\right)} \tag{2.71}$$

where the three free parameters are the amplitude A, the Half Width Half Maximum (HWHM) b and the variance σ_n^2.

The total normalized final distribution for the lateral displacement, is then given by adding 2.71 to the electromagnetic part:

$$f(x) = W_p f_M(x) + (1 - W_p)\frac{t(x)}{\int_{-\infty}^{+\infty} t(x)\mathrm{d}x} \ , \tag{2.72}$$

where $f_M(x)$ is the distribution of Eq.2.67 and W_p is the weight from Eq.2.69. Both $f_M(x)$ and $t(x)$ are normalized to unit area.

The free parameters A and b contained in equations 2.71, 2.72 are determined by fitting a FLUKA Monte Carlo simulation (see Sec.2.4.2) for the lateral displacement

distributions with the nuclear interaction switched on; during the fit procedure good results were obtained with the variance fixed at the value of $\sigma_n^2 = 1$. The behaviour of these parameter has also been studied as a function of normalized depth for the two energies; evidences show that a parametrization with Chebyshev polynomials well describes the parameters with third and eighth degree respectively and this makes the model faster to be calculated in water (in case of a different material, the nuclear parametrization has to be recalculated again by fitting a new MC simulation, and the parameters have to be simply stored in a different database.).

The difference, with respect to the pure electromagnetic case, is evident on the tails of the curve, for the larger deviations. (see Sec. 2.4.2)

2.3 Model summary

Here a short summary of all the model steps is presented, to have a synthetic overview of the overall procedure:

1. As input, the model needs the kinetic energy of the projectiles in GeV, the water thickness x, the particle type (A,Z) and the ionization potential I. The momentum p and β are calculated with the standard formulae.
   The energy can be also a energy distribution with energy spread and different beam positions and σ like in current clinic practise. This particular case is treated for the model validation and described in Sec.2.4.2

2. The *characteristic single scattering angle* χ_c is calculated with Eq.2.54

3. Then, the other crucial parameter, the parameter χ_α is calculated from Eq.2.59.

4. The parameters b and B are calculated from Eq.2.25 and 2.44.

5. Afterwords, the displacement y_M is calculated from Eq.2.62.

6. So, with all the previous results, the Molière Coulomb multiple scattering distribution $f_M(y)$ for the lateral displacement can be evaluated using Eq.2.67.

7. Now, the nuclear effects are included using the Cauchy-Lorentz distribution $t(x)$ in Eq. 2.71; it depends on two free parameters determined from the fit of the FLUKA simulated data

8. The weight factor W_p that evaluates the percentage of protons that have only had electromagnetic interactions is calculated with Eq.2.69

9. The total distribution that consider all the relevant interactions is obtained by adding the nuclear parametrization $t(x)$ to the Molière function $f_M(y)$ properly weighted by W_p. In this way the complete evaluation is given in Eq.2.72.

2.4 Validation

Equation 2.72 gives a complete description of proton displacement in water, taking into account all relevant interactions, i.e. electromagnetic interactions described by Molière theory and nuclear interactions considered by additional parametrization. So the results of this calculation have to be validated.

Two types of tests are performed:

1. the prediction of *electromagnetic* lateral distribution, by comparing the model evaluation with Monte Carlo ones (without nuclear interactions), reported in Sec.2.4.1.

2. the model *complete* lateral distribution accounting for all the interactions compared with Monte Carlo simulation (whit all possible interaction) and experimental data, reported in Sec.2.4.2.

In this section, a description of the used MC setup is given, followed by the beam profile description and the clinical experimental data.

2.4.1 Electromagnetic core results

As a first comparison, the pure Molière theory results have been compared with the MC prediction, by using two different codes, FLUKA [44],[45] and MCNP6 [46]. FLUKA uses a special transport algorithm, based on Molière's theory of multiple Coulomb scattering improved by Bethe [47], and takes into account correlations between path length corrections and scattering angle, and also between the lateral deflection and the scattering angle [47], [48]. MCNP6 instead is based on the full Goudsmit-Saunderson model of multiple scattering as described in [49].
Both simulations have been performed by switching off all the nuclear interactions, and evaluating only the pure electromagnetic ones. The comparisons have shown that the prediction of the model are fully in agreement with those of both FLUKA and MCNP6. As a case in point, typical result are shown in Fig.2.4.

2.4.2 Complete model results

The complete model calculations take into account all the relevant interaction that occur in a proton-therapy context. The results are compared in this section with both FLUKA MC simulation and experimental data. The choice of FLUKA code is motivated by the fact that it is the MC code used in HIT, where the data have been acquired.
The initial particles distribution is the exact beam set up of HIT center, performed by using a phase space file.

FLUKA set up

FLUKA simulations were performed with the HADROTHE setting for a proton beam; this allows to take into account:

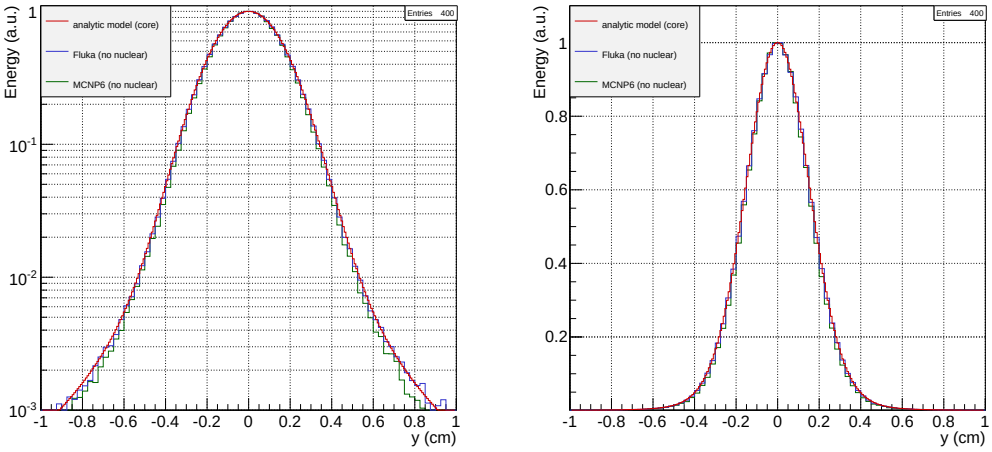

Figure 2.4: Comparison between the analytical model (red line), FLUKA (blue histogram) and MCNP6 (green histogram, slightly below the line on the log scale) in water for 200 MeV protons at a depth of 18 cm in log (left) and decimal (right) scale. All the nuclear effects (target fragmentation) are excluded.

- electromagnetic interactions
- inelastic form factor corrections to Compton scattering and Compton profiles
- low-energy neutron transport to thermal energies
- fully analogue absorption for low-energy neutrons
- complete particle transport (by setting threshold at 100 keV for all particles except for neutrons where is $10 - 5$eV)
- full multiple scattering, by setting threshold at minimum allowed energy for both primary and secondary charged particles;
- delta rays production (threshold at 100keV).

The simulations involved 10^7 primaries, batched in $10 \cdot 10^6$ histories each to reduce the variance of the scored quantities.

The **geometry** was set to account for the exact geometry in which the experimental data were acquired:

- Nozzle−isocenter[1] distance is 112.6 cm

[1] The point in space of the convergence of the three axes of rotation in radiation therapy; the intersecting point of the axis of rotation of the gantry, the collimator, and the treatment couch. The gantry rotation defines a horizontal axis which intersects a vertical axis defined by the rotation of the treatment couch. The treatment collimators also rotate about an axis pointing through the isocentre.
The placement of the radiation isocenter plays an important role in treatment planning because ideally the isocenter should be placed in the center of the target volume, usually a tumour.

- phantom is a water parallelepiped of dimensions :
  $x : [-5, 5]\, cm,\ y : [-5, 5]\, cm,\ z : [0, 32]\, cm$

- word is an air parallelepiped of dimensions :
  $x : [-30, 30]\, cm,\ y : [-30, 30]\, cm,\ z : [-115, 32]\, cm$

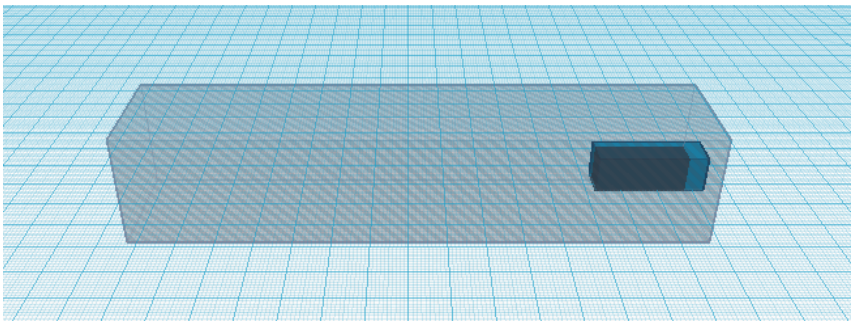

Figure 2.5: Simulation geometry setup

Scoring is ENERGY setting, to collect all the energy deposition within a mesh defined as a cartesian grid of $x :\ 1\, bin[-3, 3]\, cm, y :\ 300\, bin[-3, 3]\, cm, z :\ 2000\, bin[0, 20]\, cm$.

To reproduce the data, the **beam** conditions, the phase−space of the HIT beam line was used as input for simulations with a statistic of 10^8 initial particles. These phase-spaces (see Fig.2.6 (left)) were obtained from separate FLUKA simulations carried out at HIT, including the detailed modelling of the large area ionization chambers and multi−wire proportional chambers of the BAMS according to the manufacturer [4]. The beam scanning process of the line was simulated with a dedicated source routine, similar to the one described in [50].

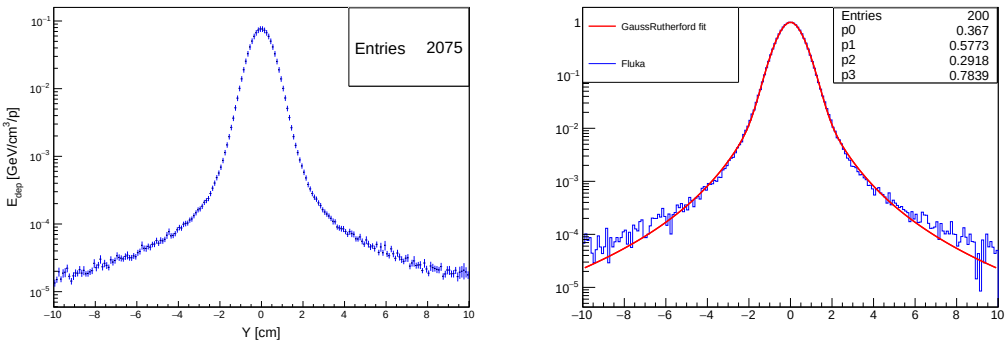

Figure 2.6: Lateral profiles of the original phase space at the isocenter for $158.58\, MeV$ proton beam at $z = 0\, cm$ depth (left) and lateral beam divergences at $z = 16.55\, cm$ (right), obtained by replacing water with vacuum. The solid lines is the fit with the function of Eq.2.73 before the convolution with the model.

An additional FLUKA simulation was performed to calculate the particles transport in a geometry made of air, but with the water target region replaced by vacuum, to take into account only the divergence generated prior to entrance in the target. These simulations have been studied at every thickness of interest and the resulting lateral displacement due only to the beam optics, have been taken into account into the model by parametrizing them with a the following function:

$$b(y) = \frac{a}{s} \exp\Big[- \frac{y^2}{2s^2} \Big] + \frac{b \cdot c}{(y^2 + c)^2} \tag{2.73}$$

where a and s are amplitude and sigma of the Gaussian respectively, b and c are amplitude and parameter of the hyperbolic (à la Rutherford) term [5].

The resulting lateral profile is then given by the convolution between the distribution of Eq.2.73 and that of Eq.2.72 for water:

$$F(y) = f * b \equiv \int f(t) b(y - t) dt \ . \tag{2.74}$$

Another effect that should be considered, in the comparison between theory and data, is that due to the detector size (see Sec.2.4.2). For the considered data, this effect can be taken into account through the parabolic normalized resolution function [51]

$$S(x) = \frac{2}{\pi R^2} \sqrt{R^2 - x^2} \ \text{ when } \ x < R \ , \ 0 \text{ otherwise,} \tag{2.75}$$

where x is the lateral position and R is the effective detector radius, quoted as $R = 0.145$ cm. To correct for these effects, we convolute this function with our final distributions of Eq.2.74, after the convolution with the beam. The results of this second convolution, as already noted by Schwaab etal (2011), have a very small effect for all the cases considered here. For this reason we will neglect the detector size effects in the following.

The behaviour of the two free parameters A and b that describe the nuclear effects as a function of the normalized depth is reported for two energies in Fig.2.7.

Figures also report the values of the coefficients of the best fit of Chebyshev polynomials of third and eighth order at the same energies used to fit the the parameters trend. The fit can improve the computational time without loosing significantly the accuracy. Another way, is to create a database of these parameters at different energies and depths with the model. Therefore for the evaluation of the nuclear parameters, two different approaches are possible: the fit of the lateral distribution tails (which requires a set of pre-calculated MC distribution) or the use of a pre-compiled external database. The latter solution does not require in advance for a full MC simulation and reproduces the same results. The two approaches are equivalent

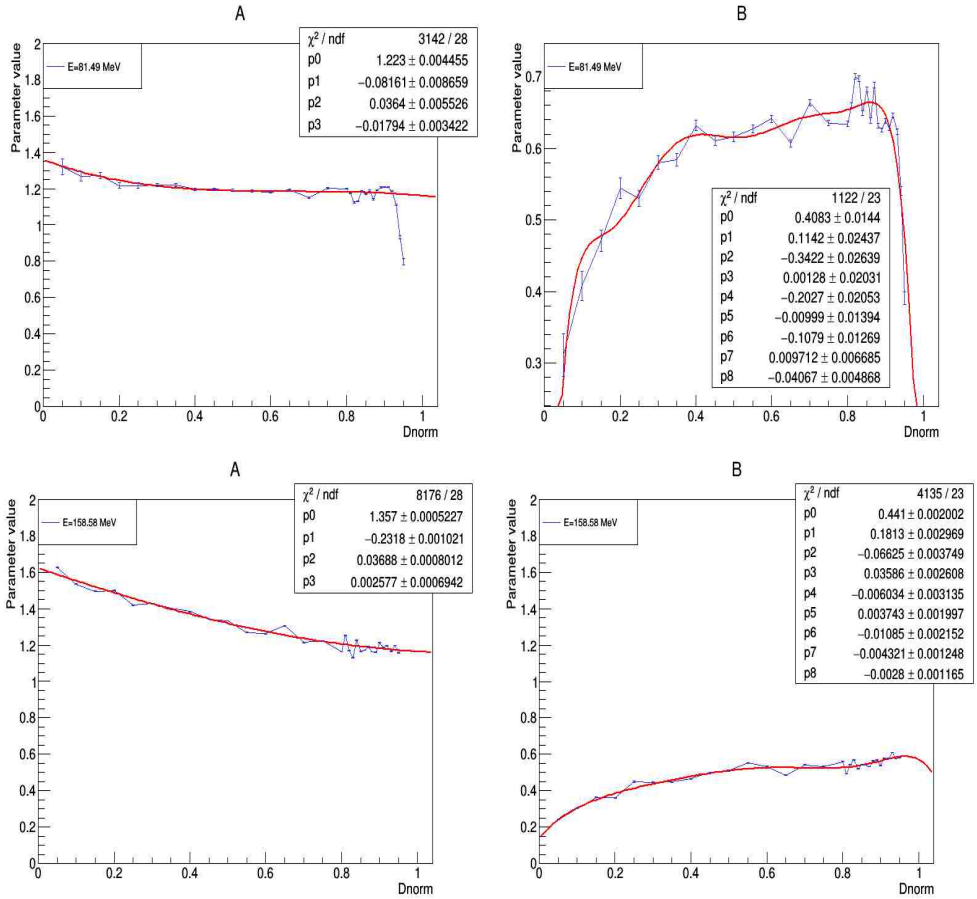

Figure 2.7: Behaviour of the free parameters A and b as a function of normalized depth for *81.49 MeV* (upper) and for *158.58 MeV* (lower).

both in accuracy and in calculation time.

Experimental data

In order to validate the predictions of the model in a realistic clinical situation of proton beam in water phantom, the model's results are compared with experimental data acquired at the HIT Heidelberg Ion Beam Therapy Center [51].

These dosimetric measurements were performed in a water phantom with entrance window at the treatment isocenter, using a special arrangement of 24 *PinPoint* ionization chambers (PTW Freiburg, type 31015, 0.030 cm^3 active volume) with six rows of four chambers aligned in lateral offset patterns (in beam-eye view) not to shadow each other, and controlled by a step motor. Lateral profiles were sampled at different depths in water by repeated acquisitions at horizontally shifted positions of the detector block for irradiation of a vertically scanned line pattern of 10 cm length and 1 mm scanning step size. Therapeutically relevant doses of

$1 - 2$Gy were delivered as an acceptable compromise between irradiation time and signal noise, especially in the low dose region. More details of the experimental setup can be found in [51].
The reported comparisons refer to initial beam energies of 81.49MeV and 157.43MeV and respectively beam sizes of 17.55mm and 10.7mm FWHM in air at the isocenter. The errors on the data range from 2% to 15%, going from the high dose points to the lowest dose regions.

Selection of results

A selection of the obtained result is shown: in figures 2.9-2.12 the data are compared with the prediction of FLUKA and of the analytical model of section 2.1.5. In any analyzed case, the model's calculations agrees very well with both FLUKA and the experimental data.
To quantify the level of agreement we have performed a Kolmogorov Smirnov test (Kolmogorov et al 1933) between our calculation and the FLUKA distribution. The model pass the test with a good *p-value* and we use the maximum distance D returned by the test to estimate the different fits quality in a relative manner as a function of depth. The good agreement is quantified by the maximum value of D obtained in our study, that is $7 \cdot 10^{-3}$ (Fig.2.8).

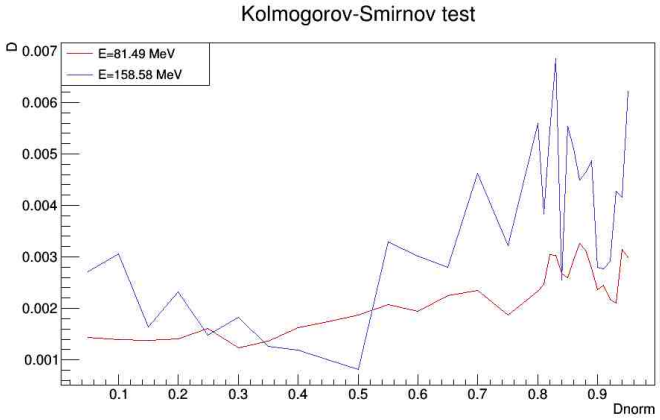

Figure 2.8: Maximum distance D obtained from the Kolmogorov Smirnov test between the model and the FLUKA simulation.

Considering that D is a parameter that does not have a universal statistical meaning, in case of binned data this is a well accepted practice. The comparison with the analogous MC calculation in case of a mono-energetic pencil beam shows as well a good agreement but with the advantage that calculation is much faster than the simulation. The computational time of the code for the evaluation of the projected distribution is mainly determined by the evaluation of the integral of

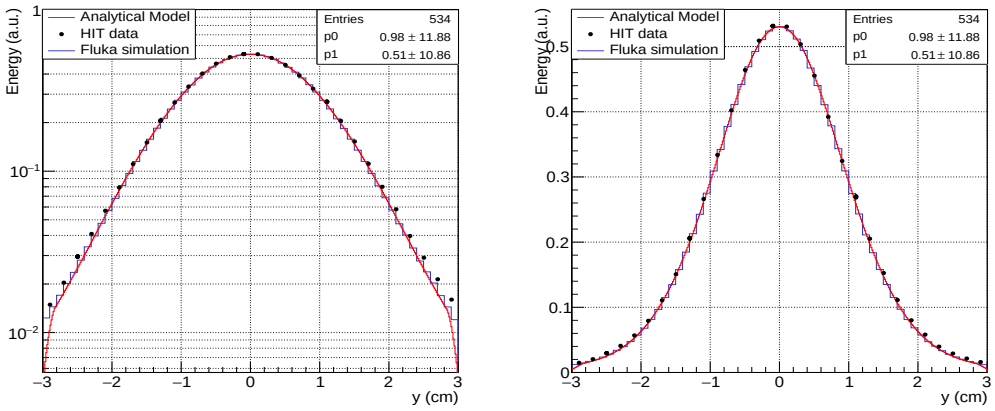

Figure 2.9: Comparison between analytical model, FLUKA simulation and experimental data for 81.49 MeV in water for a thickness of: z=1.57 cm in logarithmic (left) and linear (right) scales. The curves are normalized to the maximum of the FLUKA histogram, obtained by fitting the highest dose channels with a smooth curve. In the normalization zone the error of the data points is 2% (see section 2.4.2).

Eq.2.67 this integral in our code is computed only once for each depth and stored in a database that can be read and interpolated at any subsequent call. In this way the calculation time is reduced in average by a factor 2.

Therefore, the comparisons show that the model predictions have the same accuracy of the Monte Carlo codes, but with much shorter computational time;this aspect is reported quantitatively in the next session.

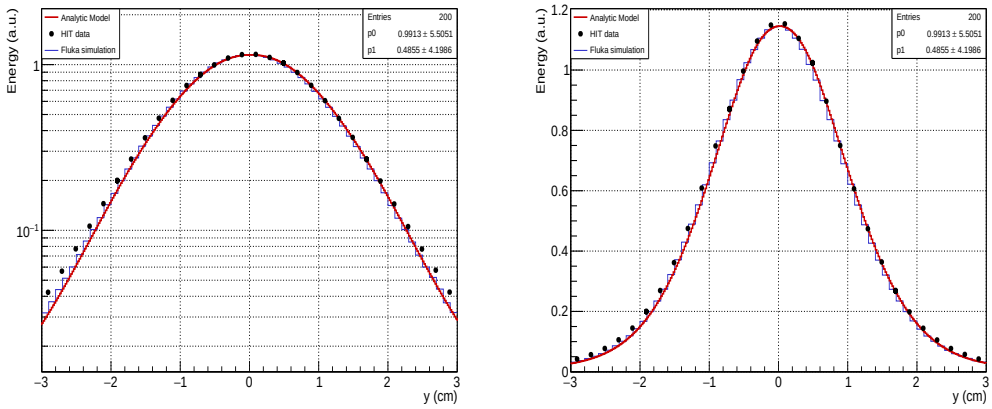

Figure 2.10: As in figure 2.9 with z=4.57 cm. Bragg peak is at 5.38 cm

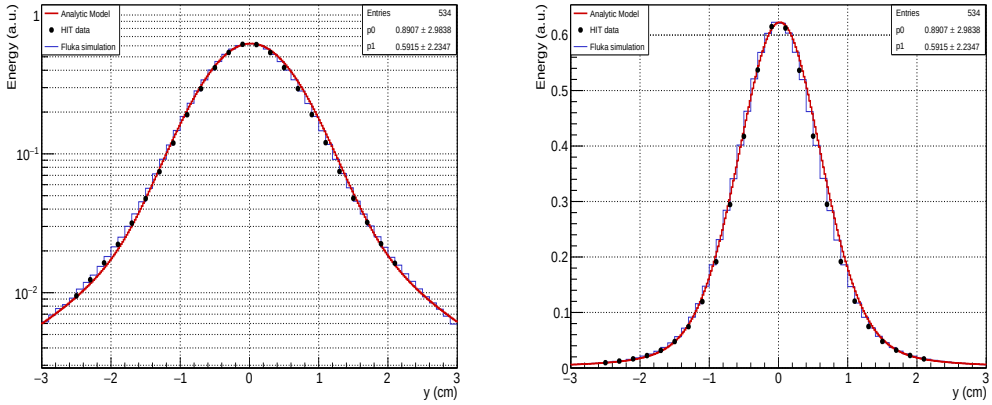

Figure 2.11: As figure 2.9 with E=157.43 MeV and z=11.55 cm.

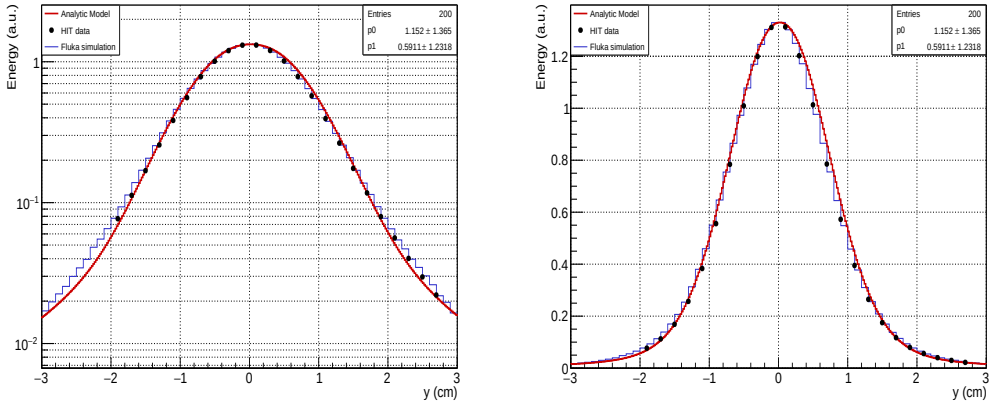

Figure 2.12: As figure 2.11 with z=16.55 cm. Bragg peak is at 17.23 cm

2.4.3 Beam scan result

To test a possible proton-therapy clinical application of the model, a beam scan is evaluated (see Sec.3.4) To reproduce this technique, the single beam profile is shifted in the beam perpendicular direction to paint a lateral scan with a given step, as in Fig.2.13. Within an homogeneous material, the calculation is performed only once and the profile is simply shifted by adding the single contributions to the dose. The result is compared with the MC prediction: the source routine is modified simultaneously with the model's single distribution lateral shift. In these conditions, on a DELL XPS computer with an INTEL core I7 (8 cores), with 3.6 GHz CPU, 16 Gbyte RAM and a 64 bit configuration, we have estimated that the computing time of the full lateral profile, using the aforementioned database for the Molière integrals, is about $3\,s$ for each depth: hence for example the time required for 100 depths is about 5min, to be compared with 90 min taken by the full MC simulation with a statistics of 10^7 primaries.

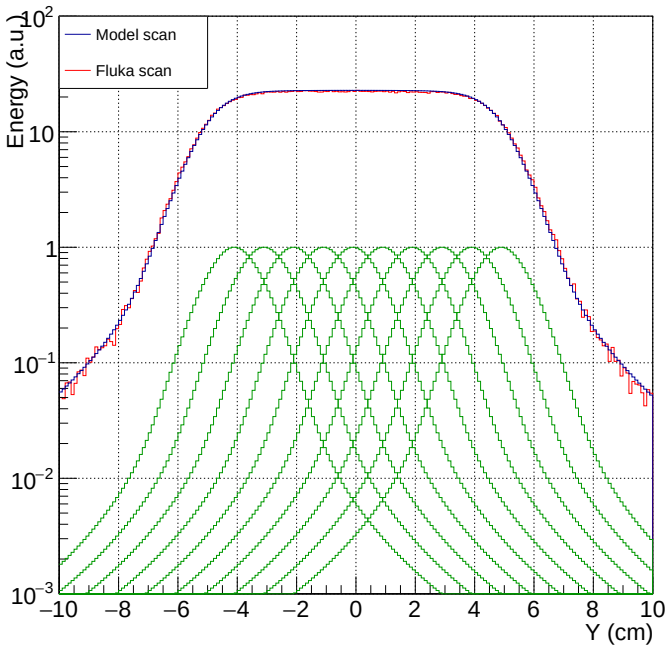

Figure 2.13: Lateral dose profile for a beam scan for the energy $81.49\,MeV$. In green a subset of the original single beams is shown.

2.5 From one dimensional to two dimensional distributions

Up to now, the lateral distribution of a proton beam passing through a layer of thickness t has been obtained, both for the spatial angular distribution and for the projected angle ones. A symmetry condition for x and y coordinates has assumed, $f_x(\theta) \equiv f_y(\theta)$.
In practices, to evaluate the lateral dose profiles, the scattering angle θ of the Molière theory [29] is replaced by the two projected angles θ_x and θ_y for a beam initially parallel to the z axis [9], [3]. This approach simplifies the mathematics of the tracking algorithms and allows the seamless convolution of the multiple scattering distribution with any initial beam profile, at the price of working with the marginal instead of the complete distributions. In order to provide a model useful for the clinical application, the combined x, y 2D distribution is essential.

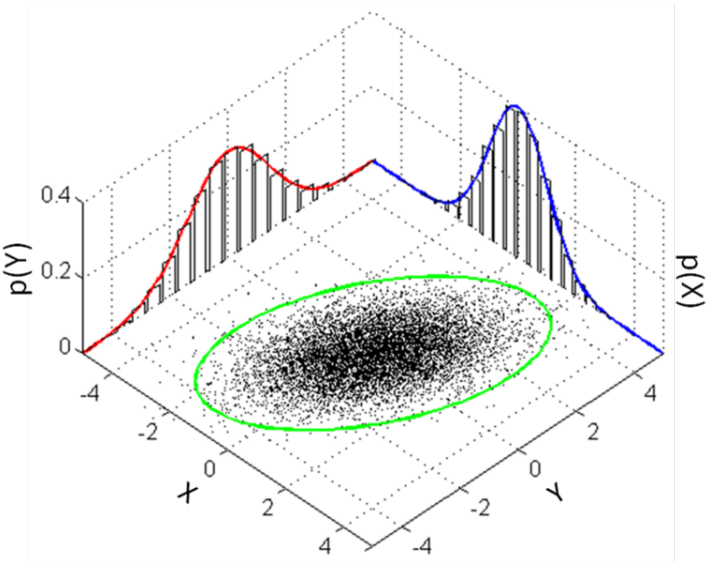

Figure 2.14: Example of a bidimensional Gaussian distribution

In the case of a Gaussian distribution, the solution is easier since it is always possible to reconstruct the joint distribution by multiplication of the two marginal distributions (Fig.2.14); in general:

$$\begin{aligned} f(x,y) &= f_x(x) \cdot f_y(y) \qquad (2.76) \\ &= \frac{1}{2\pi\sigma_X\sigma_Y\sqrt{1-\rho^2}} \exp\left(-\frac{1}{2(1-\rho^2)}\left[\frac{(x-\mu_X)^2}{\sigma_X^2} + \frac{(y-\mu_Y)^2}{\sigma_Y^2} - \frac{2\rho(x-\mu_X)(y-\mu_Y)}{\sigma_X\sigma_Y}\right]\right) \end{aligned}$$

where ρ is the correlation between X and Y, $\sigma_X > 0$, $\sigma_Y > 0$ and $\mu = \begin{pmatrix} \mu_X \\ \mu_X \end{pmatrix}$.

A base theorem of probability theory states that if two random variables are independent, they must be uncorrelated ($\rho = 0$). The reverse is generally true for

Gaussian distributions *only*. Indeed the above mentioned property for the joint distribution reconstruction is true for any pair of arbitrary chosen axes, *only* if the variables are Gaussian.

So, what if the case is not Gaussian?

- The joint distribution can not be simply calculated as $f(x,y) = f_x(x) \cdot f_y(y)$ for any arbitrary chosen orthogonal axis
- Two non-Gaussian distributions $f_x(x)$, $f_y(y)$ with cylindrical symmetry are *necessarily dependent*

These implications results from the Papoulis's theorem [52], that states that: if the property 2.76 is valid for any pair of arbitrary chosen orthogonal axis, then the variables X and Y are necessarily Gaussian.
This is for instance the case of multiple Coulomb scattering, where the long tails due to rare single scattering events and also to nuclear interactions modify the ideal Gaussian profile; it can be shown that the projected angles θ_x,θ_y of the multiple Coulomb scattering theory are uncorrelated but not independent. In the case of

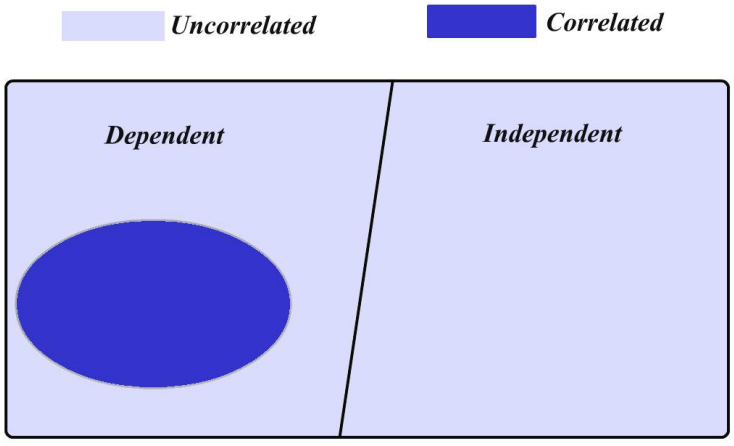

cylindrical symmetry, the radial 2-D distribution can be calculated from the projected ones by applying the Papoulis' theorem [53]; its application is described in the following section.

X-Y plane reconstruction in cylindrical coordinates

Let us consider a normalized distribution $f(x,y) \geq 0$ in the $x-y$ plane with circular symmetry; this can be expressed as:

$$f(x,y) = \hat{f}(r) \ , \quad r = \sqrt{x^2+y^2} \ . \tag{2.77}$$

The marginal distribution $f_x(x)$ of $f(x,y)$ on the x axis is:

$$f_x(x) = \int_{-\infty}^{\infty} \mathrm{d}y f(x,y) = \int_{-\infty}^{\infty} \mathrm{d}y \hat{f}(r)\mathrm{dy} = 2\int_0^{\infty} \hat{f}(\sqrt{x^2+y^2}) \tag{2.78}$$

This equation defines the projection operator that transforms $\hat{f}(r)$ into $f_x(x)$ by preserving the normalization. It is important to underline that the relation can be inverted to obtain $\hat{f}(r)$ from $f_x(x)$, i.e. to obtain the joint distribution from the marginal one, under the essential hypothesis of circular symmetry. The procedure is described in [52],[53], and in this work the main steps will be applied.
First, the following function has to be defined:

$$h(r) = \int_{-\infty}^{\infty} f_x(\sqrt{t^2+r^2})\mathrm{d}t = \int_{-\infty}^{\infty}\int_{-\infty}^{\infty} \hat{f}(\sqrt{t^2+r^2+y^2})\mathrm{d}y\mathrm{d}t \tag{2.79}$$

where the last term comes from Eq.2.78.
Passing in polar coordinates $t = \rho\cos\theta$, $y = \rho\sin\theta$, one obtains :

$$h(r) = 2\pi\int_0^{\infty} \hat{f}(\sqrt{r^2+\rho^2})\rho\mathrm{d}\rho \ . \tag{2.80}$$

And with the substitution $v^2 = r^2+\rho^2$, the following formula is obtained:

$$h(r) = 2\pi\int_r^{\infty} \hat{f}(v)v\mathrm{dv} \ . \tag{2.81}$$

in which the specific lower limit should be notated.
Then, the Leibnitz rule of differentiation is applied under the integral sign, in order to evaluate the final formula:

$$\hat{f}(r) = -\frac{1}{2\pi r}\frac{\mathrm{dh(r)}}{\mathrm{dr}} \tag{2.82}$$

The Eq.s 2.79, 2.82 just obtained, are the solution to reconstruct the 2D distribution with cylindrical symmetry, starting from a *non Gaussian* 1D projected distribution, to be used instead of Eq.2.76:
$f_x = f_y \rightarrow \hat{f}$

2.6 Conclusion

This chapter has presented a pencil beam model based on Molière theory, able to predict the lateral deflection in water with the same accuracy of current MC codes and with shorter computational time.
The model takes into account all the relevant interactions, the electromagnetic part is purely analytical without any free parameter, and the nuclear reactions are also considered using a parametrization with only two parameters. A systematic study has been also presented to evaluate such parameters and strongly reduce the computational time. So the model evaluates both the particle deflected angle distribution, and the spatial displacement on a detecting plane. The comparison with data, at two different energies, shows very good agreement between data, model and MC calculation.

Chapter 3

Treatment Planning system implementation

In this chapter the CERR (A Computational Environment for Radiotherapy Research)[13], [14] treatment planning system (TPS) will be described. After a general introduction on the system principles and the general concepts of TPS, the attention will be focused on the settings for the lateral dose calculation.

3.1 Introduction

In current clinical practice, plans are generated with a software application called *Treatment Planning System (TPS)*, using an iterative trial-and-error process. As a first step medical physicist and doctors identify the regions of interest (see Sec.3.2) by contouring them on CT images of the patient. These parameters are sets of input to the software. The main distinction between all the available software is *forward* or *inverse* planning.

Forward process is mainly based on the experience of human operators that makes a first choice of beam angles, weighting factors for the various clinical criteria, and other parameters. A 3D dose calculation algorithm in the TPS is then used to automatically optimize beam profiles and calculate the resulting dose distribution, based on the patients planning CT-scan. If the dose distribution is unacceptable or if the operator and treating physician see room for improvements, the operator will change some parameters (again based on experience) to generate a next, dose distribution, and so on. Reasons for stopping the iterative process may be that the dose distribution is considered satisfactory and/or the physician and operator may not see how new parameter adjustments could further improve the patients dose. With this procedure, the final dose distribution will generally depend on the skills

and available time of the operator and the physician. The process may be very labour-intensive, taking up to several days for an individual patient and there is no guarantee for an optimal trade-off between objectives, nor is there a guarantee that for the same tumour dose, dose delivery to the most important healthy tissues cannot be further reduced.

Inverse treatment planning, is a inverse process that starts from the dose constrains required by physicians and evaluates the input parameters (such as beam angles, energies and beam positioning) to satisfy them. The process is automatically done by performing the minimization of a quadratic dose objective function $p_s \left(D_i - D_i^0\right)^2$, where D_i is the dose in voxel i, D_i^0 is the prescribed dose and p_s a importance weight factor. The minimization of this function is called optimization (described in Sec.3.5), and leads to maximize of the dose that has to be delivered to the target and in the meanwhile to minimize of the dose to non-target regions. In this thesis a inverse treatment planning system has been chosen, and a description of the steps (see Fig.3.1) required to use it is given in following sections.

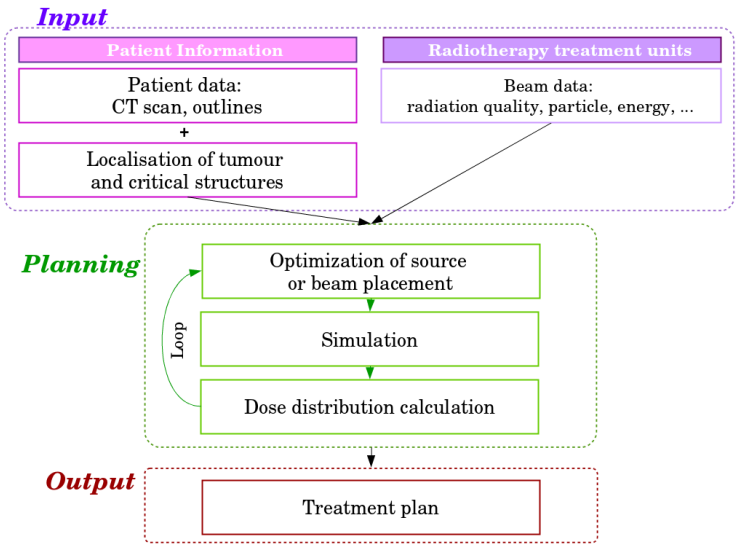

Figure 3.1: Schematic flowchart of a inverse treatment planning system

3.2 Clinical volumes

When delivering a radiotherapy treatment, parameters such as volume and dose have to be specified ad priori for different purposes.
The official definitions are given by ICRU (International Commission on Radiation

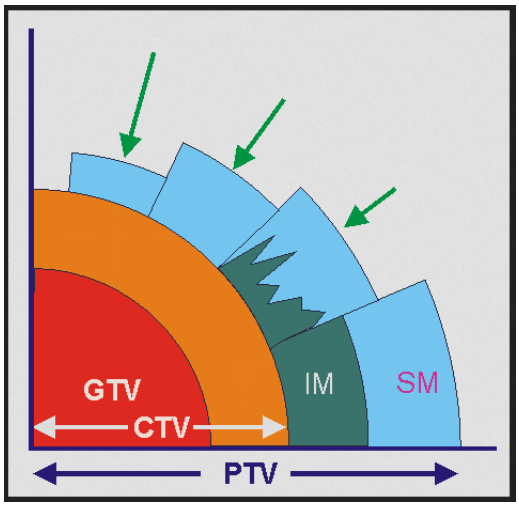

Figure 3.2: The diagram shows the various volumes to be considered. GTV is the volume as seen by physicians. CTV is the volume calculated according to the pathological knowledge of usual local invasion by cancer. PTV is a compromise taking into account various physiological phenomena (respiration, difficulties in positioning the patient, patient movement) as well as the Internal Margin (IM) to be added to CTV to compensate for internal physiologic movements and variation in size, shape, and position of the CTV during therapy in relation to an internal reference point and its corresponding coordinate system, and the Set-up Margin (SM) for patient movement and set-up uncertainties. Normal tissue (in dark green) is included in the PTV. The arrows show various attempts to reduce parasitical irradiation, the ideal being of course the smallest volume (ICRU Report no. 62 (25).

Units and Measurements) reports, primarily in Report 50, 62, 78 and 83 and the main elements are:

- **Gross Tumour Volume (GTV)** The GTV is the gross palpable or visible/demonstrable extent and location of the malignant growth.

- **Clinical Target Volume (CTV)** The CTV is a tissue volume that contains a GTV and/or subclinical microscopic malignant disease, which has to be eliminated. This volume thus has to be treated adequately in order to achieve the aim of the therapy (cure or palliation). For external beam therapy, margins will have to be added around the CTV to compensate for the effects of organ and patient movements and inaccuracies in beam and patient set up.

- **Planning Target Volume PTV** The PTV is a geometrical concept, and it is defined to select appropriate beam sizes and beam arrangements, taking into consideration the net effect of all the possible geometrical variations and inaccuracies in order to ensure that the prescribed dose is actually absorbed in the CTV.

Another set of structure are defined depending on the treatment used:

- **Treated Volume (TV)** is the volume enclosed by an isodose surface, selected and specified by the radiation oncologist as being appropriate to achive the purpose of treatment (e.g., tumour eradication, palliation).
- **Irradiated Volume (IrV)** is that tissue volume which receives a dose that is considered significant in relation to normal tissue tolerance.
- **Organs at Risk (OR)** are normal tissues whose radiation sensitivity may significantly influence treatment planning and/or prescribed dose.

3.3 CERR - A Computational Environment for Radiotherapy Research

CERR (Computational Environment for Radiotherapy Research) [13], [14] is an open source radiation therapy tool written in MATLAB (www.mathworks.com). It provides a convenient and powerful software environment to develop and prototype treatment planning concepts, offering the possibility of reading computed tomography scans, contouring structures on them and converting the informations into MATLAB matrix. It provides the ability to extract treatment plans from many different planning systems using the widely available AAPM/RTOG archiving mechanism, and offers various tools to quantify the dose distribution and the comparison between different plans.
Within the input geometry, PTV is fixed and the outside region is called WORLD; furthermore a safety margin of $+1cm$ in each direction x, y, z is added, creating the structure PTV+1. The aim of the plan is to delivery dose at PTV avoiding to irradiate the world, by setting as non-target region the volume PTV+1 (see Fig. 3.3)

This geometry is divided in voxel and saved in a MATLAB matrix; for the purpose of this work, the set-up is an homogeneous water box phantom of $30 \times 30 \times 30cm^3$ with different PTVs, as described in Chap.*(CERR Results)*

3.4 Dose evaluation

After the geometry is acquired and the structures are delineated, the calculation of the dose can start. The dose delivery technique of CERR is the *spot (or beam) scanning technique*. In this technique, the pencil beam transported to the beam nozzle by the beam transport system is directly sent into the patient without interacting with any scattering or energy-modulation devices. An orthogonal pair of magnetic

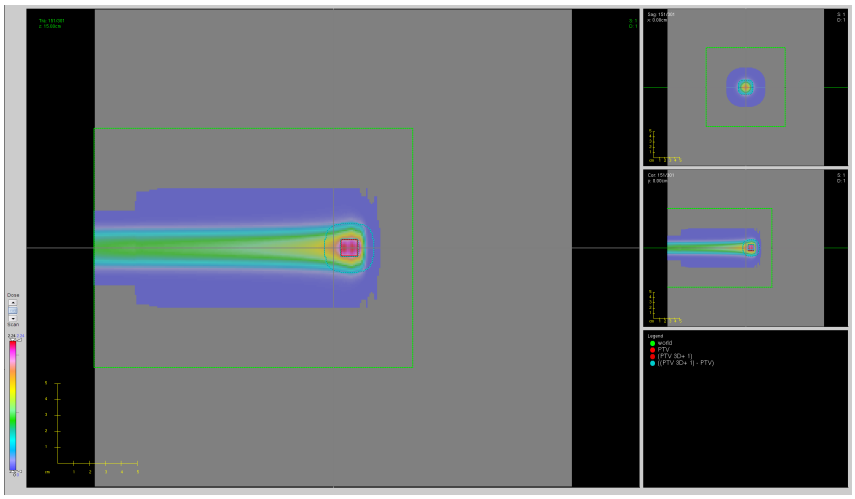

Figure 3.3: Screenshot of CERR interface; the three gray windows are the different cutting planes. The structures are displayed in different colours, in this case WORLD (green), PTV (red) and PTV+1 (cyan). The dose distribution is illustrated in colours with the intensity colour scale on the left.

dipoles is used to steer the thin beam to reach the full lateral extent of each target volume elements (voxels). The dose distribution is delivered by placing specific Bragg peaks in the patient one location at a time on a discrete grid (spot scanning) and then one layer at a time by varying the beam energy [30].

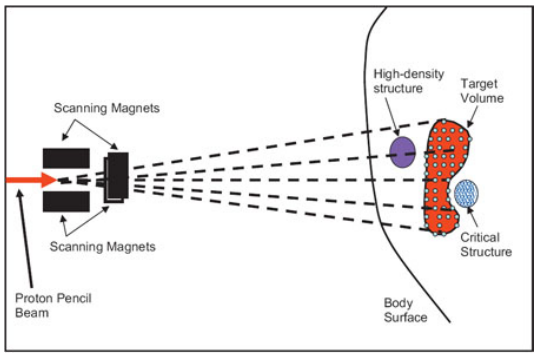

Figure 3.4: Schematic representation of beam scanning method

Each voxel that composes the discrete grid is correlated with a structure, e.g. CTV, OAR .. and to each of them have a weight factor w_{ij}. Based on this assignment the different incident beam directions are chosen. The fluence matrix is defined separately for each beam in the isocenter plan, perpendicular to the beam direction. The sum of all selected PB in each voxel i creates in this way the SOBP, and the

total dose results in

$$D = \sum_{i \in PTV} D_i = \sum_{i \in PTV} \sum_{j \in PB} w_j D_{ij} \tag{3.1}$$

where the matrix D_{ij} is the dose of PB_j in each voxel i and the weight factor w_j accounts the weight of each PB.
This process is a inverse process since the system evaluates the best assembly of beams (energy and position) to cover the PTV without irradiating the surrounding tissues .
Within this technique, the axial and the lateral dose distribution are described separately and convoluted; so, assuming z the beam direction, D in Eq. 3.1 can be expressed as

$$D = \frac{D_{xy}}{\int D_{xy}} * D_z \tag{3.2}$$

The longitudinal dose D_z is evaluated with a lookup table (LUT) produced using Geant4 simulations (see Sec.3.7.1) and the lateral dose contribution is described in next section.

In CERR the user has to set the beam direction, the initial σ_0, to account for the beam spread, the target region (PTV) and the non-target region (PTV+1, and also the WORD); thereafter the system begins the PB selection.
The definition of Pencil Beam differs from the definition used in the previous parts of the thesis: mono-energetic spots with the same central axis are summarised to a Pencil Beam, while a spot is one single Bragg peak;

$$\text{Spot} : \text{single Bragg peak (Fixed energy } E_j \text{ and position } x_i, y_i)$$

$$\text{PB} = \sum_{j=0}^{n} \text{Spot}_{\text{i;j}}(E_j, x_i, y_i) \text{ (Several energies in coaxial positions } i)$$

$$\text{Beam} = \sum_{k=0}^{m} \text{PBs (Several energies and positions)}$$

A grid of pencil beams is placed for each beam direction to cover the lateral shape of the tumour (see 3.5). The grid has an equidistant binning of 0.5 cm steps in a plane perpendicular to the irradiation direction (lateral), and the spots have an initial $\sigma_0 = 0.4$ cm in order to obtain a realistic configuration in clinical practice [54].

After the positions of the spot grid, the depths in beam direction are determined; for this purpose the depth of each voxel that has to be irradiated, is expressed in terms of the water equivalent path length (WEPL) and the beams are selected based on their energy.

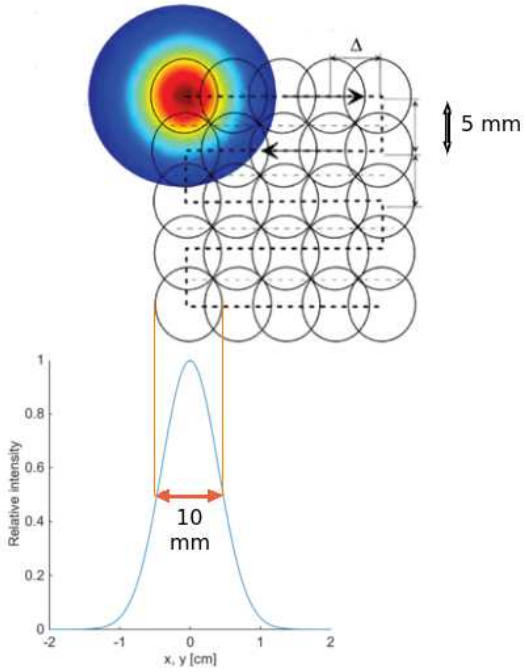

Figure 3.5: Schematic representation of beam scanning method

CERR has a database of Geant4 simulations, created by irradiating a homogeneous phantom (0 HU [1]) with protons of 30 to 250 MeV in 1 MeV steps; based on those results, for each energy the range is tabulated using the definition of *distal dose falloff*, *i.e.* position where the dose has decreased to 80% of the maximum dose. The reason for this choice is the fact that for a monoenergetic proton beam, the 80% fall-off position coincides with the mean projected range of a proton, that is the range at which 50% of the protons have stopped.

If the desired range of a PB lies in between these discrete steps, the Bragg-peak of the next higher energy is shifted to the desired range by a simplified range shifter. The range shifter is approximated as material of the necessary water equivalent thickness in the beamline well before entering the patient.

So, the system selects the energies required to cover the tumour area and the positions of the spots between all the possible configurations given by the explained grid.

[1]The *Hounsfield unit (**HU**)* is a quantity commonly used in computed tomography (CT) scanning to express CT numbers in a standardised and convenient form. Hounsfield units, created by and named after Sir Godfrey Hounsfield, are obtained from a linear transformation of the measured attenuation coefficients. This transformation is based on the arbitrary definitions of air and water: $HU_{air} = -1000$, $HU_{water} = 0$, obtaining $HU = 1000 \times \frac{\mu - \mu_{water}}{\mu_{water} - \mu_{air}}$

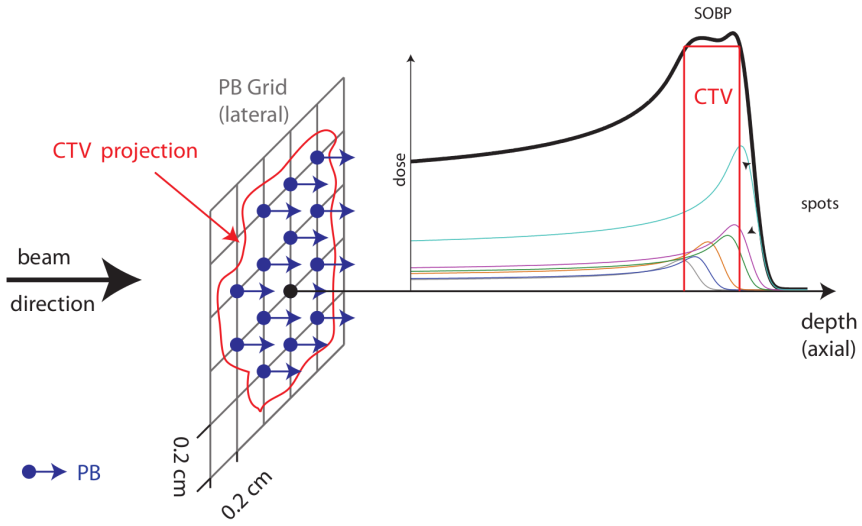

Figure 3.6: Beam structure: One beam direction is divided into parallel Pencil Beams. The PBs are placed on a equidistant (lateral) grid and CERR chooses the PBs that hit the CTV. Every chosen PB is sub- divided into spots. One spot reflects one (available) particle energy. The spots have different weights to perform a Spread-out Bragg peak (SOBP).

3.4.1 Lateral dose evaluation

In CERR the lateral dose distribution is currently calculated, for each PB, using two normalized 2D Gaussian functions.

$$\begin{aligned} D_{xy1}(x,y) &= \frac{1}{2\pi\sigma_1^2}\cdot\exp\left(\frac{-(x_b^2+y_b^2)}{2\sigma_1^2}\right) \\ D_{xy2}(x,y) &= \frac{1}{2\pi\sigma_2^2}\cdot\exp\left(\frac{-(x_b^2+y_b^2)}{2\sigma_2^2}\right) \end{aligned} \tag{3.3}$$

where x_b and y_b are relative coordinates centred on beam axis, and σ_1, σ_2 are read in a LUT based on the energy and depth (see Sec.3.7).
The two contributions are separately multiplied with two separate longitudinal dose vectors

$$\begin{aligned} D_1(x,y,z) &= D_{z1}\cdot D_{xy1} \\ D_2(x,y,z) &= D_{z2}\cdot D_{xy2} \end{aligned} \tag{3.4}$$

and then the total dose is calculated as the sum of both contributions

$$D(x,y,z)[Gy] = D_1 + D_2 \tag{3.5}$$

One of the original contributions of this thesis is the update of this method using the lateral values evaluated with the model described in chap.2:

As inputs parameters the model requires the depth z, the energy E and the ionization potential E_i. For each depth the function gives a 2D matrix in the x, y plane V_{mod}[MeV/cm^3], that stores in each voxel(i,j) the value of the lateral dose deposition.

$$V_{mod} = \frac{\sum_i \sum_j \Delta E_{i,j}}{\Delta V} \equiv \varepsilon[\text{MeV/cm}^3]] \tag{3.6}$$

where i runs over x coordinate and j on y coordinate. This matrix is automatically read by CERR, that interpolates x_b and y_b at intermediate points.

Since ε[MeV/cm^3] is the energy deposition and CERR requires the dose, a conversion is made; the dose is defined as the energy deposited per unit mass of the irradiated medium and it is measured in Gy (Gray), $1Gy = 1$J/Kg. To obtain the dose as input for CERR calculation, considering the water medium ($\rho_{H_2O} \cong 0.001[Kg/cm^3]$), this simple conversion is performed

$$D[\text{Gy}] = \frac{\varepsilon}{\rho_{H_2O} * 1.602 \cdot 10^{19}} = \varepsilon * 6.24 \cdot 10^9 \tag{3.7}$$

3.5 Optimization process

The optimization process is a multi-criterial problem, i.e. it involves more than one objective function to be optimized simultaneously, since usually a single solution that simultaneously optimizes each objective does not exist. Since the tumour has to be irradiated to a high dose, and healthy surrounding tissues should be avoided as much as possible, the process has to find the best set-up for:

- coplanar beam orientation
- treatment angles and beam weights
- intensity modulated beams

Optimizing both beam directions and intensity profiles is a huge mathematical multi-criteria, non-convex[1], discrete combinatorial problem that cannot be solved directly. The first two problems can be considered as a combinatorial optimisation problems, whereas the last one has been referred to as an '*inverse problem*'[55],[56]. Only the last one will be described since the set-up that has been chosen for the purpose of this thesis, has only one parallel beam (a complete description of the overall optimization process can be found in [57]).

[1] *Non convex problem* is a problem of non linear programming, i.e. the optimization may have multiple locally optimal points and it can take a lot of time to identify whether the problem has no solution or if the solution is global.

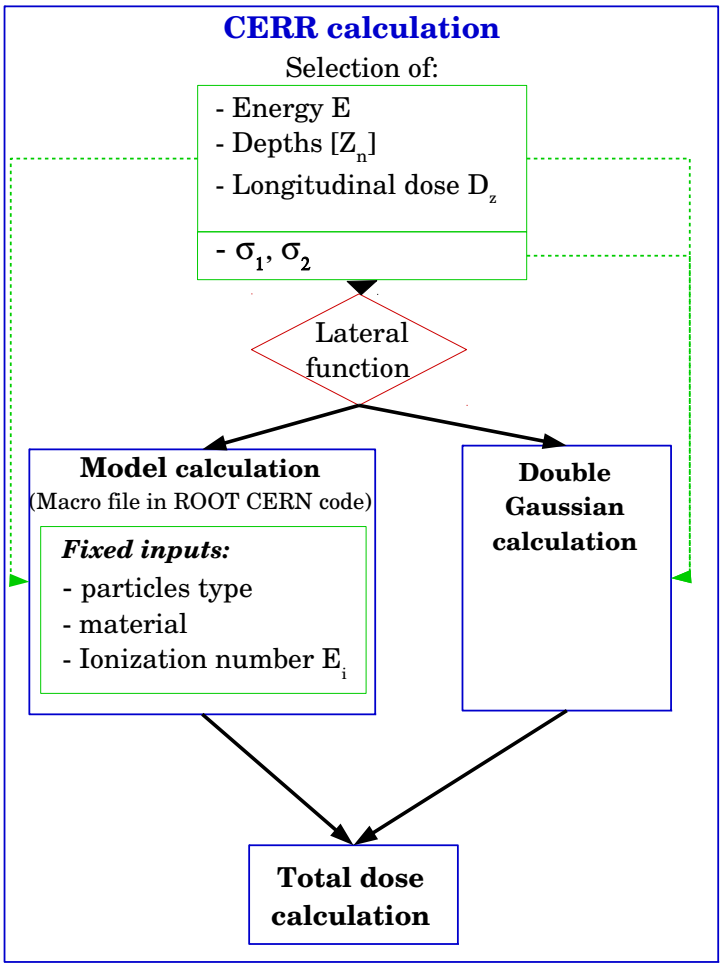

Figure 3.7: Schematic view of the CERR lateral dose evaluation.

The inverse problem (or *inverse process*), concerns the determination of the selection of the optimal weights of the preselected PBs to ensure the delivery of an uniform dose in the PTV, according to the physicians prescription. So it works back from a dose prescription to the determination of the best beam profiles that can produce such a dose distribution.
The problem of obtaining a uniform dose in PTV, minimizing in the meanwhile the dose on surrounding tissues, is reduced to the minimization of the *quadratic objective function*

$$F(w) = \sum_{i \in S} \left(D_i(w) - D_i^0 \right)^2 \tag{3.8}$$

where $D_i(w)$ is the result of the evaluation in 3.1 and D_i^0 is the desired dose in structure.
Minimizing this equation that runs all over the voxel j in structure S, leads to the optimal weight for each spot to be used in order to obtain the prescribed dose.
Another weight factor p_s has to be introduced to take into account critical structures; it is called *penalty factor* since it assigns a different importance to each structure. With this additional consideration Eq.3.8 is rewritten as:

$$F(w) = \sum_{S \in A} \left(p_s \sum_{i \in S} \left(D_i(w) - D_0 \right)^2 \right) \tag{3.9}$$

with A stands for the set of considered structures.
Using penalty factors ensures that the different consequences of the quadratic deviations $\left(D_i(w) - D_i^0 \right)^2$ for different structures can be adapted to medical requirements.This is done by setting to 0 the dose D_0 of structure S where the dose should be reduced, i.e. organs at risk (OARs) [58],[59]. Generally, the importance factors p_s are equal for all voxels in an organ [60]. In CERR the minimization is performed by a built-in function *fmincon*, which uses a gradient based optimization algorithm [61].

So, the optimal weights are determined by minimising the objective function $F(w) = min$ with $\omega_j \geq 0 \forall j$. The side condition means that the number of particles per spot cannot be negative. A spot j with $\omega_j = 1$ typically consists of $1 \cdot 10^6$ particles.

3.6 Treatment quality quantification

Visual analysis of the dose distribution, particularly in association with the anatomical data, is one of the major ways that physicians and treatment planners use to make decisions about how the treatment plan should be optimized or if it can be

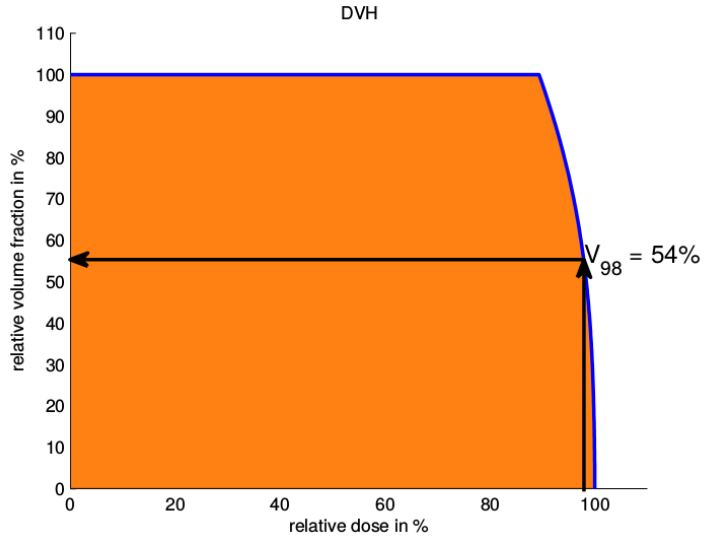

Figure 3.8: Example DVH of a CTV. The area highlighted in orange is correlated with the mean dose. The determination of V_{98} is indicated by the two black arrows.

accepted. Several dosimetric end points have been defined in ICRU Reports No. 23 and 50 for this purpose.

3.6.1 Dose-Volume-Histogram

A qualitative isodose distribution superpositioned over computed tomographic (CT) data is often insufficient to provide qualitative data for the Radiation Oncologist to determine the adequacy of a patient treatment plan. A more quantitative result is necessary which modern treatment planning systems provide in statistical analysis plots known as *dose-volume histograms* (DVHs). These plots describe the dose throughout the volume of each structure contoured within the plan. On the x-axis the relative dose is plotted, on the y-axis the relative volume reaching the dose is plotted. Therefore, this means that a DVH plot indicates the relative volume receiving at least a certain dose. For an ideal treatment the DVH of a CTV would be a rectangle with 100% dose for 100% of the volume, while the OAR should be a rectangle with 0% for 100% of the volume.
The average dose that a volume receives, can be interpreted as the area under the DVH line, and is called *mean dose*.

Other useful values for the quantification of the quality of the plan are the Relative Volume V_{95} and V_{98}. V_{98} is the relative volume that receives at least 98% of the dose, and it is determined on DVH as in Fig.3.8

3.7 MC database comparison

CERR evaluates the required ranges and the σ_1, σ_2 in Eq.3.3 used for the lateral dose evaluation, by using Monte Carlo database values. Since the databases have been created using Geant4 (GEometry ANd Tracking) [62], [63] where the model is based on FLUKA simulations[1], to avoid any possibility of mismatches the two codes results have been compared to test their consistence.

3.7.1 Geant4

The Geant4 simulation is executed for mono-energetic protons in water.
The resolution of the scoring mash grid in this simulation is $0.01\,cm$. Hence the cuts for secondary electrons as well as for photons and for positrons are set to 0.005 cm. Tests have shown that smaller cuts only increased the computation time but had no influence on the output data [58]. Physical interactions in Geant4 are activated by using predefined C++ class packages in which cross sections and the cut off are specified the. The physics list used to create the database of CERR is QGSP_BIC_HP [63] (comparable to the one in the *Hadrontherapy* advanced Geant4 example).
Material is homogeneous water with mean excitation energy of 68.327eV[2], density $\rho = 1.0055\,\mathrm{g/cm^3}$ and elements of volume composition of:

Element	volume percentage
O	0.45070
C	0.41751
H	0.10950
N	0.01902
S	0.00163
Cl	0.00163

The number of initial particles is 10^6 and the score matrix is a $30 \times 30 \times 30\,\mathrm{cm^3}$ cube of 1 mm resolution.

3.7.2 FLUKA

FLUKA simulation uses the *hadrontherapy* set-up and the same values of Geant4 for water, with the same media definition. The score matrix is equal to previous one and the output score is *Energy*.

[1] Code used at HIT and CNAO centres

[2] Here, a different value for the mean excitation energy is used with respect to the value I=77 eV in Sec.2.1.4, since the test aims to reconstruct the parameters used in CERR. To be consistent, also the new simulations of FLUKA use this value.

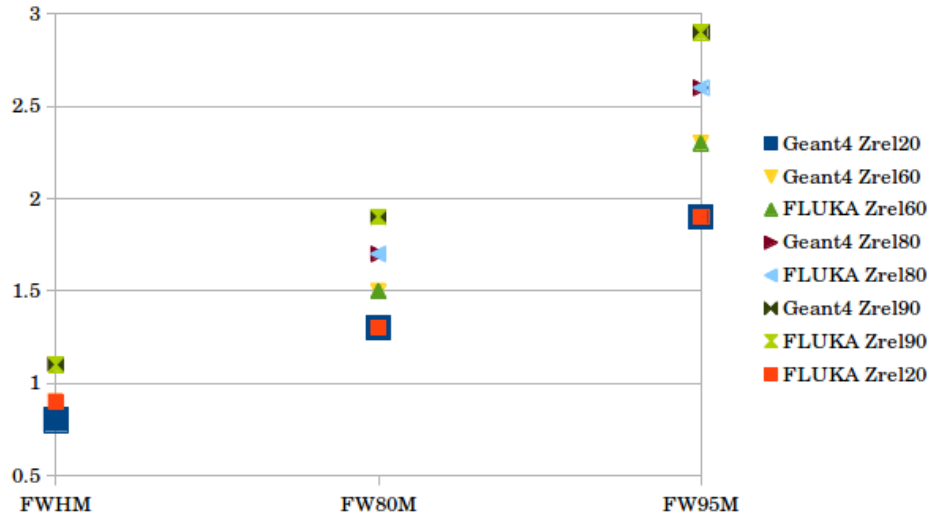

Figure 3.9: Plot of the comparison between Geant4 and FLUKA values of FWHM, Full Width 80% Maximum (FW80M) and Full Width 95% Maximum (FW95M), for $Z_{rel} = 20\%, 60\%, 80\%, 90\%$ at $E = 158$MeV

3.7.3 Comparison Results

The comparison of several energies and depths shows a good agreement between the two MC code results. A selection of the results is shown for comparison; the two MC codes are in good agreement both for the lateral distribution Fig.3.10, 3.11, and for the longitudinal distribution 3.12. Range and Full Width Half Maximum (FWHM) are compatible. A quantitative check is summarized in Fig.3.9 where the FWHM and the width at 80% and 95% of the maximum have been evaluating for relative depths of $Z_{rel} = 20\%, 60\%, 80\%, 90\%$.

Taking into account the agreement that is obtained by these results, the model evaluation using FLUKA simulations and CERR double Gaussian calculation, based on GEANT simulations, can be considered consistent, and no difference between them can be due to the MC codes difference.

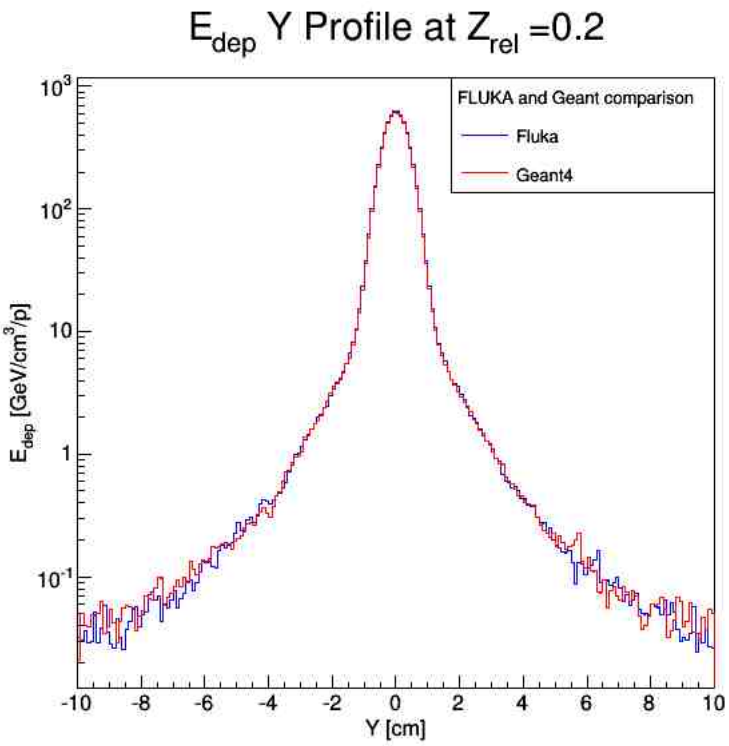

Figure 3.10: Comparison of the lateral energy distribution between Geant4 (red curve) and FLUKA (blue curve) for a proton beam of initial $\sigma = 0.8cm$ and energy $E = 158\text{MeV}$, at a normalized depth of $z_{rel} = 20\%$

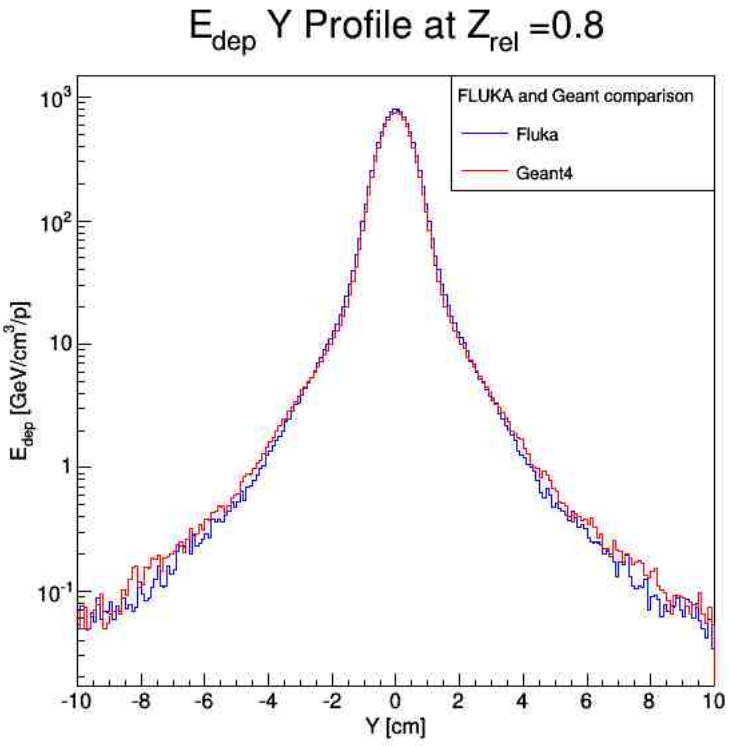

Figure 3.11: As in 3.10 for a normalized depth of $z_{rel} = 80\%$

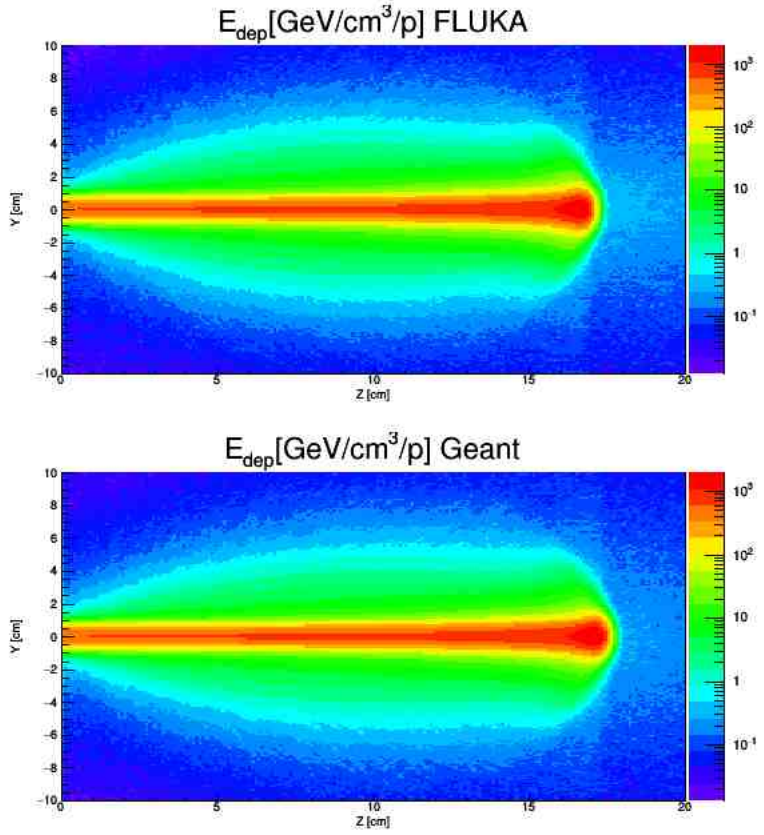

Figure 3.12: Comparison of the energy distribution between FLUKA (top) and Geant4 (bottom) for a proton beam of initial $\sigma = 0.8$cm and energy $E = 158$MeV

Chapter 4

CERR Results

The purpose of this chapter is to present the results obtained including the model introduced in Chap.2, in the CERR TPS. To study the possible improvements that can be obtained using the model, the same treatment plan has been optimized using the current Double Gaussian (DG) approximation and the model for the lateral calculations, and both have been compared with the MC plan re-evaluation (*MC Opt ReCalc*) as reference.
First, a single beam dose deposition study will be presented, showing the comparison between the DG, the model and the MC curves, for different energies and depths of clinical interest along the beam axis. Next the study of a full treatment plan dose deposition will be explained, as an outlook to give an idea of the differences achieved in a more realistic case. Subsequently, results obtained in a phantom with inhomogeneities will be considered.

4.1 Single beam

In order to test the effective benefits of introducing the model in the TPS instead of the current DG approximation, several treatment plans have been evaluated using only one beam of 10^7 particles. The same plan has been optimized by CERR, using the DG parametrization, then the model calculation for the calculation of the lateral profile, and each plan has been re-evaluated with *MC Opt ReCalc*. The single beam is not a realistic clinical case, but it is well suited to show the different lateral shapes obtained using the two different approaches, highlighting the possible improvement in the accuracy that can be obtained for each beam.

4.1.1 Phantom set up

In order to select only one single beam in CERR (see Sec.3.4), with fixed energy and position, the choice of the position of the PTV has to be changed in order to let

the system select the right range of energies needed to hit the target; CERR selects these energies using a LUT that associates the energy to the position at 80% of the peak dose (before the peak) as in Fig.4.1.

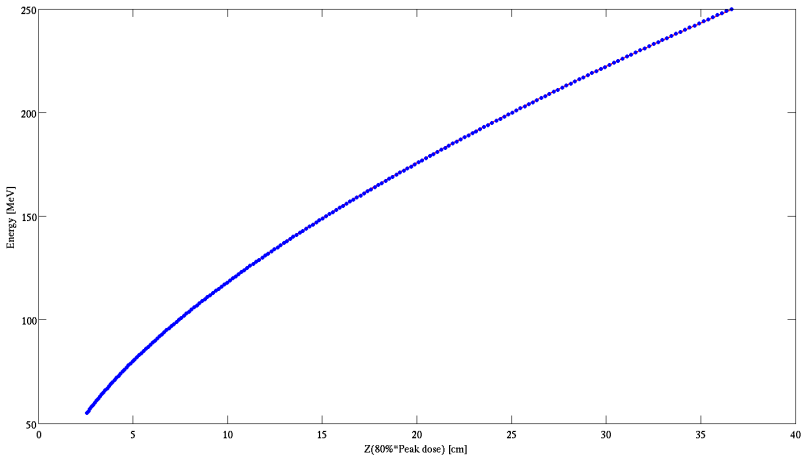

Figure 4.1: Plot of CERR database of the position at 80% of the peak dose (before the peak) versus the energy. This curve is used by the TPS to select the beams that are needed to achieve the best dose delivery to the PTV region.

For this purpose an homogeneous water phantom of $30 \times 30 \times 30\,\mathrm{cm}^3$ with 1 mm voxel size, was used as WORLD, in which the target PTV of $1 \times 1 \times 1\,\mathrm{cm}^3$ has been moved along the Z axis, to select the desired range of energies to cover it. A 3D margin of 1 cm expansion was set around the PTV to obtain the safety margin for the treatment in which the dose has to be minimized [13],[14],[58]. Then, manually, a weight of 0 has been assigned to all the sublets contained in the selected energy range group, except the selected one, resulting in a mono energetic beam. With this method, the following energies have been studied: 64 MeV, 148 MeV, 195 MeV. These are in the range of a clinical interest case, and each beam has a initial spread of $\sigma_0 = 0.4$ cm.

4.1.2 Lateral beam comparison

For each energy, two separate treatment plans were evaluated; one using the DG lateral parametrization and one using the model results. Later on, each plan was recalculated with the *MC Opt ReCalc*: one of the two optimized plans[1] is exported as a voxelized geometry in DICOM files; from these, the density of each voxel is read as HU and converted in density $\rho\,[g/cm^3]$ using a LUT [64]. The beam information is exported as well and with the CT is used as input for the simulation using 10^7

[1] Since is the case of a single beam, the two plans are equivalent in terms of optimization because the only parameter that the optimizer could change is the amplitude, that does not affects the normalized lateral beam shape.

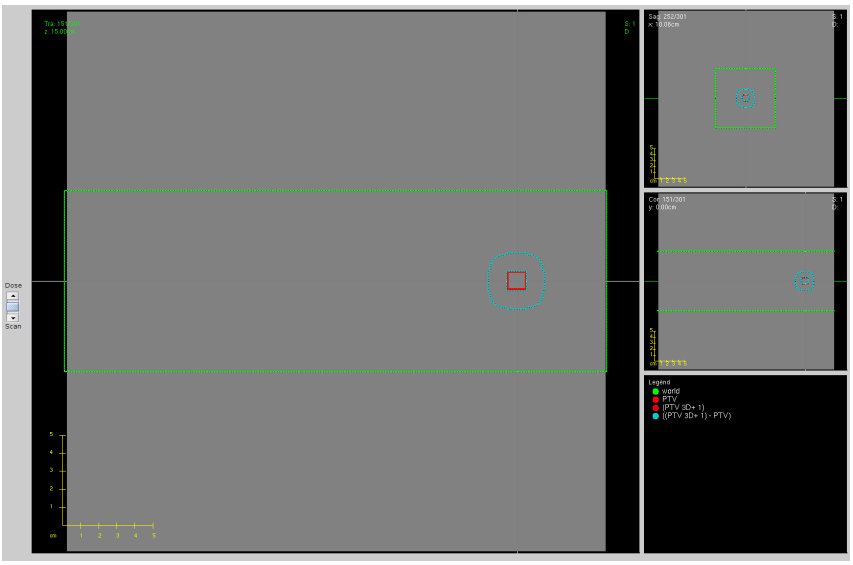

Figure 4.2: Example of geometry set up displayed in CERR interface. The world is a parallelepiped of water of $10 \times 10 \times 30\,\mathrm{cm}^3$ displayed in green, the PTV in red, is $1 \times 1 \times 1\,\mathrm{cm}^3$ positioned at a depth of 20 cm and the cyan region is the safety margin in which the dose has to be minimized by the optimizer, it is delineated following the clinical requirements, adding 1 cm^3 to the PTV.

initial particles (simulation details are described in Sec.3.7.1).

A selection of results is reported here, plotting the lateral profiles obtained within this procedure, for different normalized depths[1] . In the displayed plots, both the DG and the model show a discontinuity point at the same position. This is due to the fact that the system, to reduce the computational time, stores in two different vectors the values that are considered as *high dose* points and the ones considered as *low dose* points and two different weights are assigned to these vectors; this results in a discontinuity at the passage point from one vector to the the second one.

[1] *Normalized depth*(Z_{rel}) refers to the depth normalized to the position of the Bragg Peak: $Z_{rel} = Z \cdot 100/Z_{BP}$

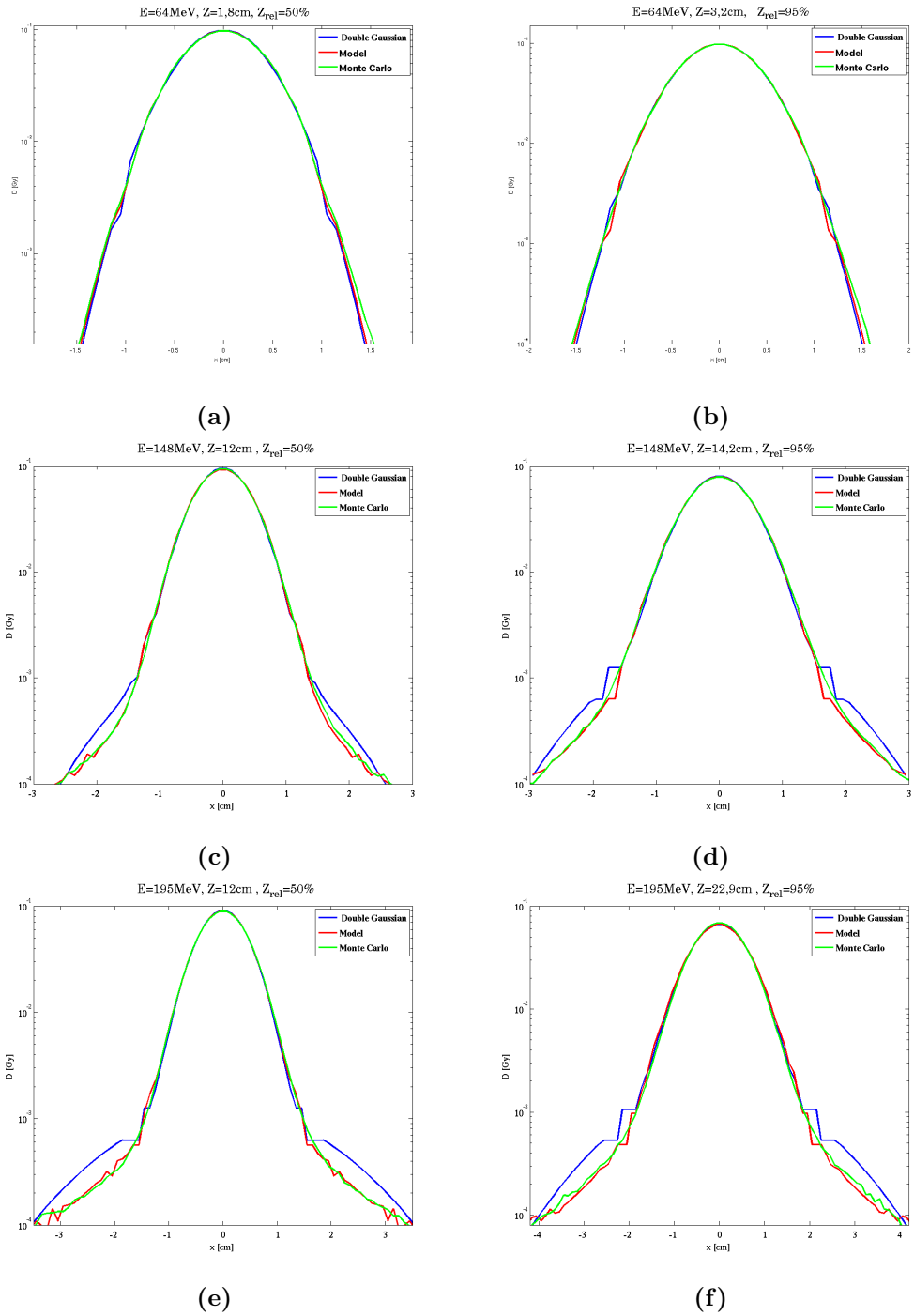

Figure 4.3: Lateral profile of the dose deposition evaluated by CERR TPS, in logarithmic scale for a single beam of energy E=60 MeV at a relative depth of $Z_{rel} = 50\%$ **(a)** and $Z_{rel} = 95\%$ **(b)**; the same for E=148 MeV **(c)**,**(d)** and E=195 MeV **(e)**,**(f)**. The blue curve represents the dose calculated using the DG lateral approximation to evaluate the plan, in red, the one obtained using the model to evaluate the same plan and the green one is the *MC Opt ReCalc*.

4.1.3 Kolmogorov-Smirnov test

To quantify the difference between the two approaches, a two sample Kolmogorov-Smirnov test [65] is performed evaluating the p-value[1] obtained when comparing the DG versus the MC and the p-value between the model and the MC. The test is evaluated at the 5% significance level for several depths. In Fig.4.4, the plots of results are reported for each energy, at a $Z_{rel} = 0\%$, 20%, 50%, 95%.
As the plots show, the model has higher values with respect to the DG ones (that means a better agreement), for all the analysed cases, and the agreement between the DG and the MC tends to decrease with the increase of the depth and the energy (except for the depth Z=0% where both the model and the DG are in good agreement with the MC). This behaviour is due to the fact that the parametrization with the DG function of the real case, is more difficult for large depths because the nuclear interactions play an increasing relevant role and the function assumes a less smooth behaviour.

4.1.4 Lateral width

The lateral beam shape of the three curves, normalized per area, has been tested evaluating the different lateral sizes of each curve as the FWHM (Full Width at Half Maximum), FW20%M (Full Width at 20% Maximum), FW10%M (Full Width at 10% Maximum) and FW0.5%M (Full Width at 0.5% Maximum). The plots of the results are shown in Fig.4.5,4.6,4.7 for three different energies at four relative depth each: $Z_{rel} = 0\%$, 20%, 50%, 95%. Also this test shows a good agreement between the model and the MC evaluation for all the analysed cases; the FHWM values of the three different curves are in good agreement for all the energies, and the differences between the model (in agreement with the MC, for all the depths) and the DG is increasing by increasing the depth and the energies. Furthermore, the DG curves show a small underestimation of the lateral width except on the FW0.5%M, where there is a net overestimation of the dose, as it can be also seen in Fig.4.3.
This finding is due to the fact that the DG parametrization is not fully accurate, and an overestimation of the width is preferable to an underestimation one, so the σ_2 value that are automatically chosen to evaluate the function, based on the energy and depth (see Sec.3.4.1), are considered broader to reach this purpose.

[1] The two sample Kolmogorov-Smirnov test is a nonparametric test that compares the cumulative distributions of two data sets. This test reports the maximum difference between the two cumulative distributions, and calculates a *p-value* from that; this value quantify the probability that the two cumulative frequency distributions would be as far apart as observed [66].

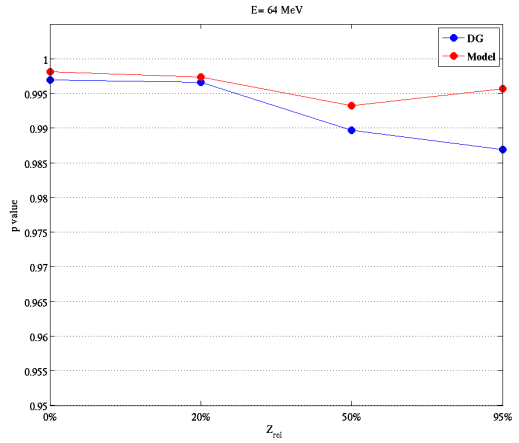

(a)

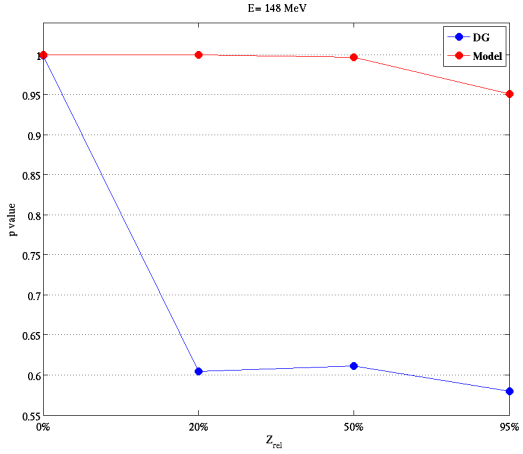

(b)

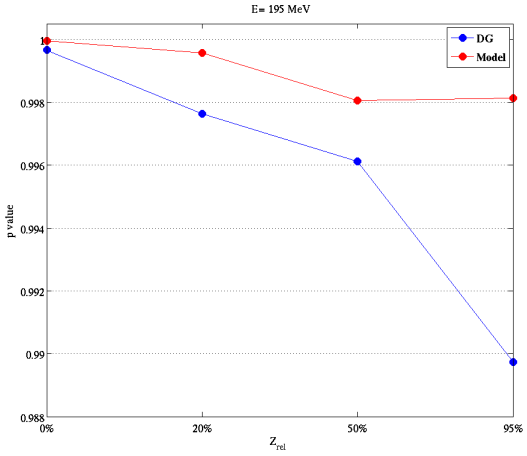

(c)

Figure 4.4: P-value results of Kolmogorov-Smirnov test for the energy E=64 MeV **(a)**, E=148 MeV **(b)**, E=195 MeV **(c)** at the relative depths of Z_{rel} = 0%, 20%, 50%, 95%. A linear interpolation of the points is added to improve visualization. The DG values are displayed in blue, the model ones in red.

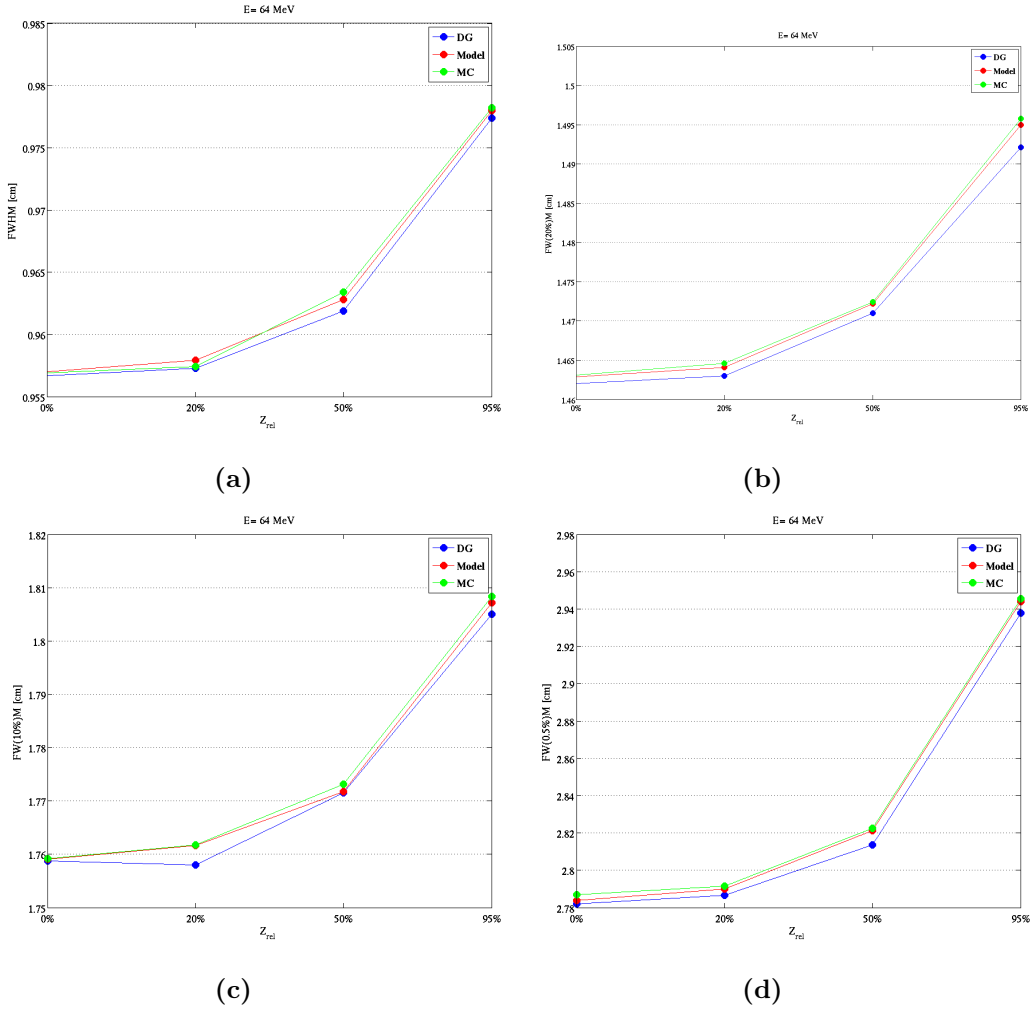

Figure 4.5: Plots of the values for the FWHM **(a)**, FW20%M **(b)**, FW10%M **(c)** and FW0.5%M **(d)** for a single beam of energy E=64 MeV at relative depths of Z_{rel} = 0%, 20%, 50%, 95%.

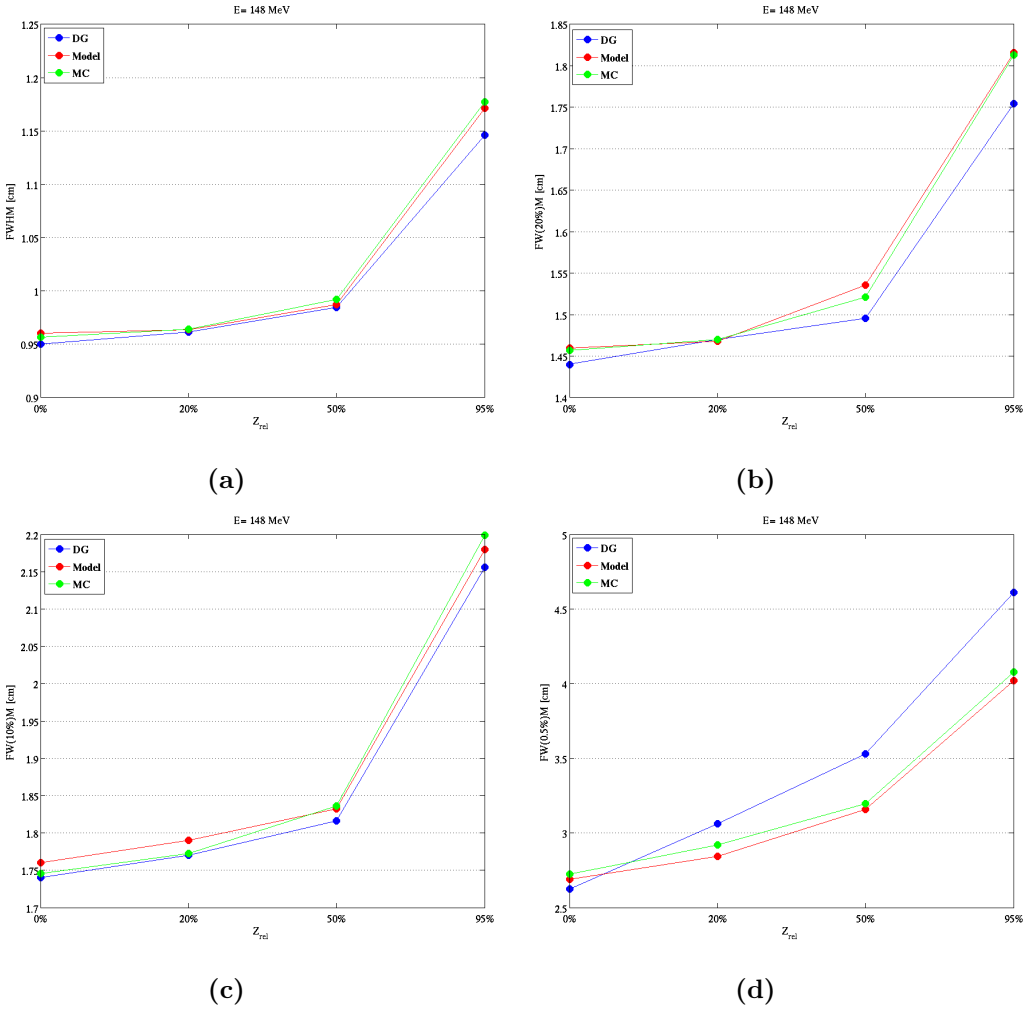

Figure 4.6: Same as in Fig.4.5 for a single beam of energy E=148 MeV.

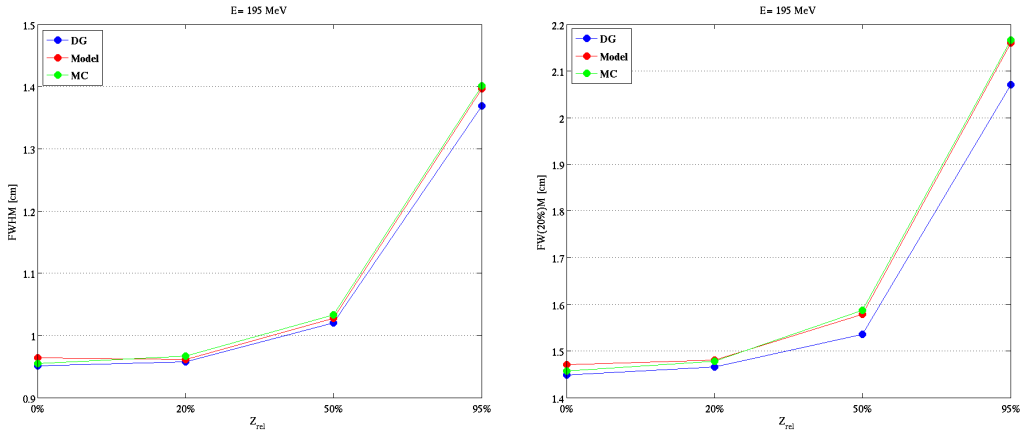

(a) **(b)**

(c) **(d)**

Figure 4.7: Same as in Fig.4.5 for a single beam of energy E=195 MeV.

4.2 Full treatment plan

After the results for a single beam are obtained, a full treatment case is considered. The plan is a geometrical case, chosen in order to show the possible application and future development of the implementation of the model. In this case the PTV and

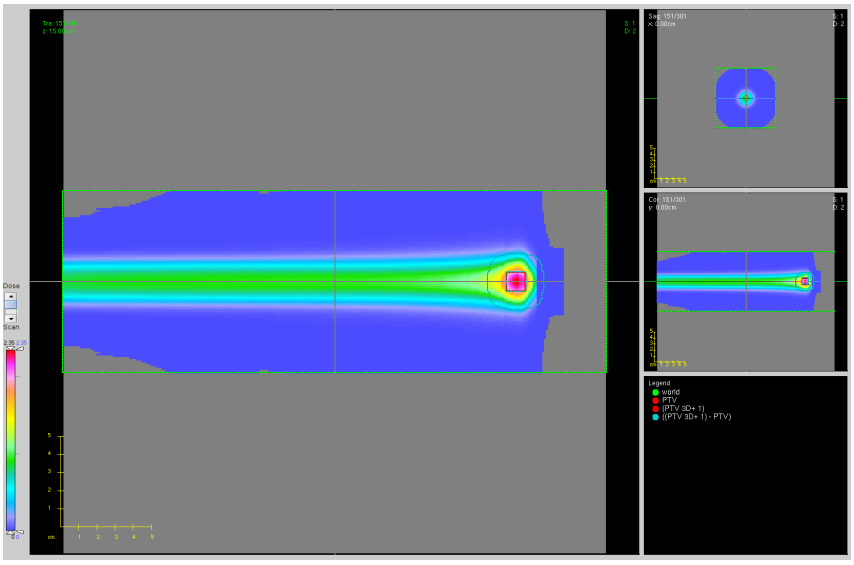

Figure 4.8: Full treatment plan dose deposition using the model results to evaluate the lateral beam shape, displayed in CERR interface. The geometry set up is a world of water of $10 \times 10 \times 30\text{cm}^3$ displayed in green, the PTV in red, is $1 \times 1 \times 1\text{cm}^3$ positioned at a depth of 20 cm and the cyan region is the safety margin in which the dose has to be minimized by the optimizer, it is delineated following the praxis requirement, adding 1 cm^3 to the PTV. The lateral cutoff is extended until 5 cm, to study the lateral differences between the different approaches, while the default one is normally evaluated at 2σ; this is the reason for which in the WORLD area, a blue dose region is displayed.

the WORLD are chosen in as in Fig.4.8. The system was allowed to choose the full set of energies to obtain the best isodose in the PTV region; the dose prescription was 2 Gy. With this geometry, the selected energies were 193 MeV, 195 MeV, 198 MeV, 200 MeV, 202 MeV. As for the case of the single beam, a plan is evaluated using the model and then a second one with the DG parametrization. Both plans were revaluated with the *MC Opt ReCalc*[1] as described in Sec.4.1.2. To study the lateral shape, the lateral cut off[2] has been set at the maximum level of 5 cm.
A selection of the results for the lateral beam shape is shown in Fig.4.9. The model is in good agreement with its *MC Opt ReCalc*, while the agreement between the

[1] In this case, the plans have been separately reevaluated because the optimization process varies different parameters, i.e. the range shifter, the weight of each beam, and not only the amplitude as in the case of the single beam.

[2] The value of the distance perpendicular to the beam axis, after which the dose is not calculated any more

DG and its *MC Opt ReCalc* is lower. So the model can be considered as a better description of the lateral energy deposition compared to the DG approximation. But from this first comparison, it is not possible to establish which plan is better; this test aims only to compare the lateral accuracy of the two curves, taking as reference the two different MC re-evaluation for the two different curves. To evaluate the quality of the treatment plan, a Dose Volume Histogram (DVH) analysis has been calculated.

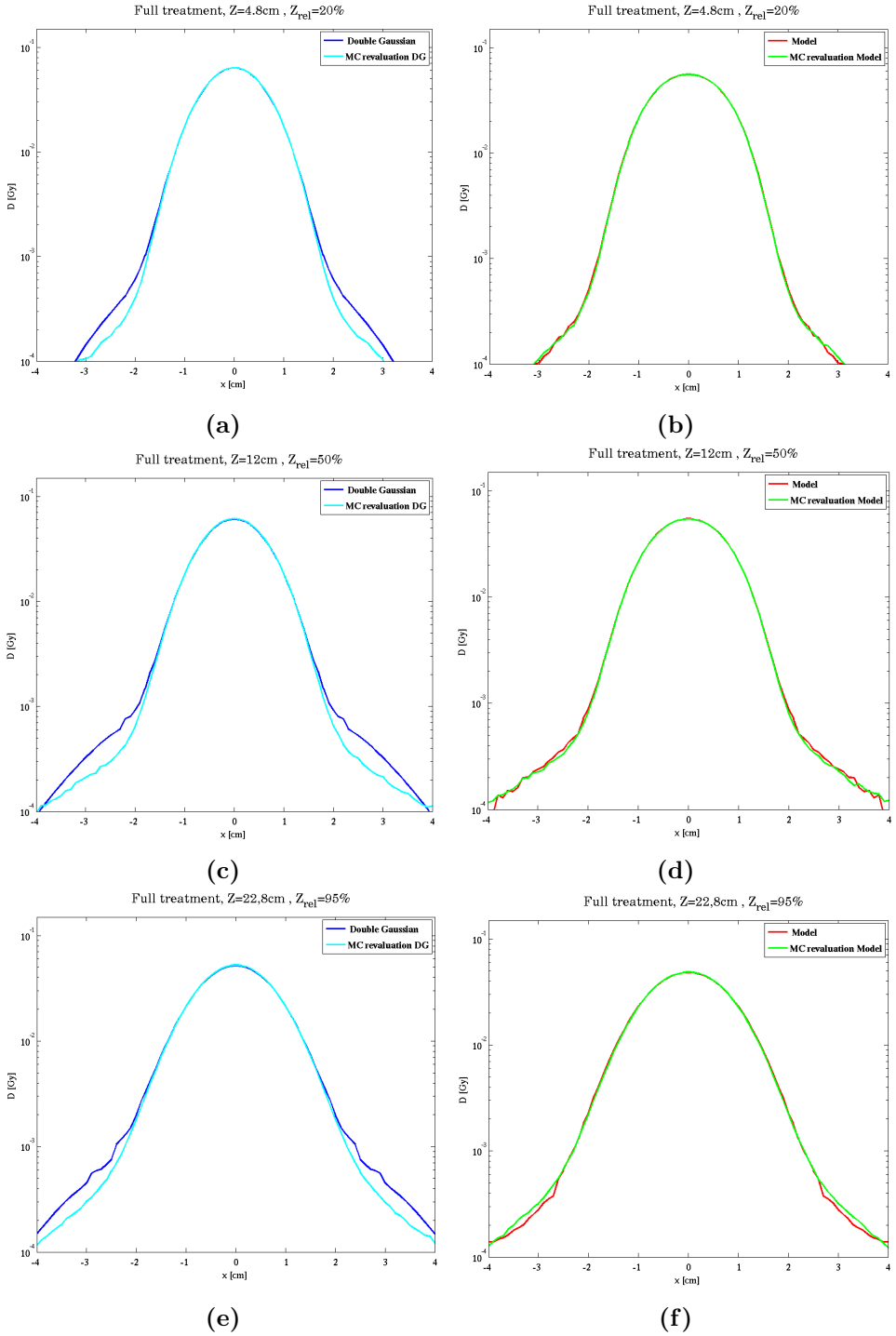

Figure 4.9: Lateral profile of the dose deposition evaluate by CERR TPS, for a full treatment plan. Fig. **(a), (c), (e)**, show the comparison between the dose evaluated using the DG lateral approximation to evaluate the plan in blue and the DG *MC Opt ReCalc* in cyan, is shown for relative depths of $Z_{rel} = 20\%, 50\%, 95\%$. Fig. **(b), (d), (f)**, show the same comparison but using the model, in red and its *MC Opt ReCalc* in green.

4.2.1 Dose Volume Histogram

A DVH is a graphical representation of the dose that is received by normal tissues and target volumes within a 3-D radiation therapy plan [67]. It provides information on the volume of a structure receiving a given dose over a range of doses. Fig.4.10, 4.11, 4.12, show cumulative DVH; they represent the percentage or absolute volume receiving greater than or equal to the value in the corresponding dose bin. These DVH were obtained using a phantom as in Fig.4.8, by expanding the PTV in X and Y direction by 3 cm, because the reported PTV was an interesting case of study for the lateral profiles analysis, but it was too small to analyse the dose deposition by a DVH. The nominal dose for this treatment was 2 Gy. The DVH of the DG and its *MC Opt ReCalc* is presented in Fig.4.10, where a general overdosing in the regions is visible except for the WORLD one. The same comparison for the model and its *MC Opt ReCalc* is reported in Fig.4.11; in this case the model evaluations is in better agreement with the MC, even if is not fully accurate. This is mainly due to the fact that the longitudinal dose is not calculated by the model, but based on CERR LUT and in region after the Bragg peak the model has still to be enhanced. Finally, Fig.4.12 shows the direct comparison between the model DVH and the DG ones; the delivered dose to the PTV is almost equal in the two cases but the dose on surrounding healty tissues ((PTV3D+1)-PTV) is lower with the model.
Overall one can conclude that a plan obtained using the model for the lateral evaluation of the dose, is a promising candidate instead the DG ones in terms of treatment quality.

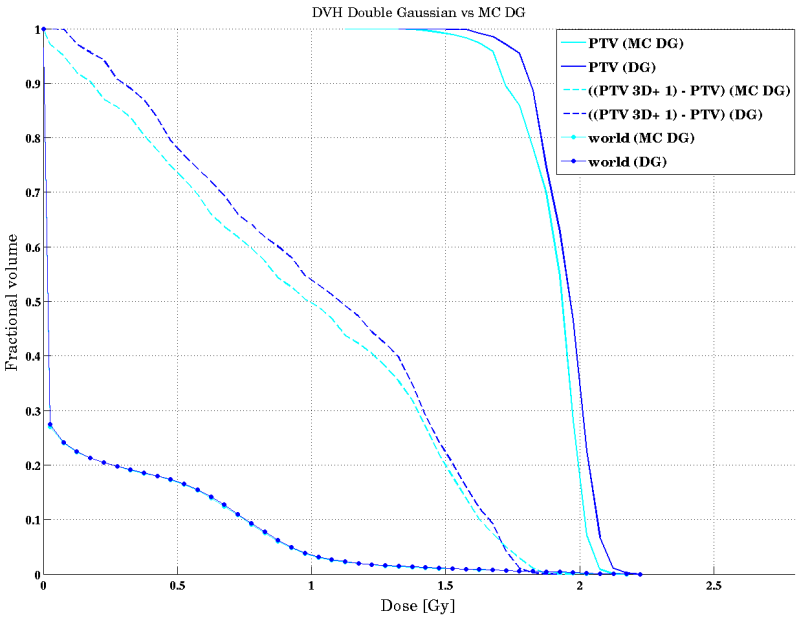

Figure 4.10: DVH calculated by CERR, for the PTV, the safe margin of PTV + 1 cm and the WORLD regions, both for the plan obtained with the DG (blue curves) and its *MC Opt ReCalc* (cyan curves).

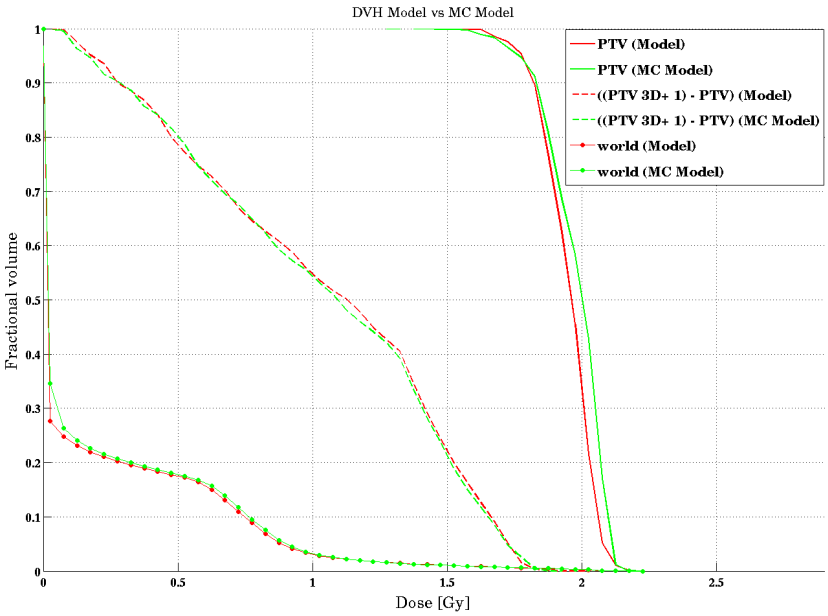

Figure 4.11: Same as in Fig.4.10 for the model (red curves) and its *MC Opt ReCalc* (green curves).

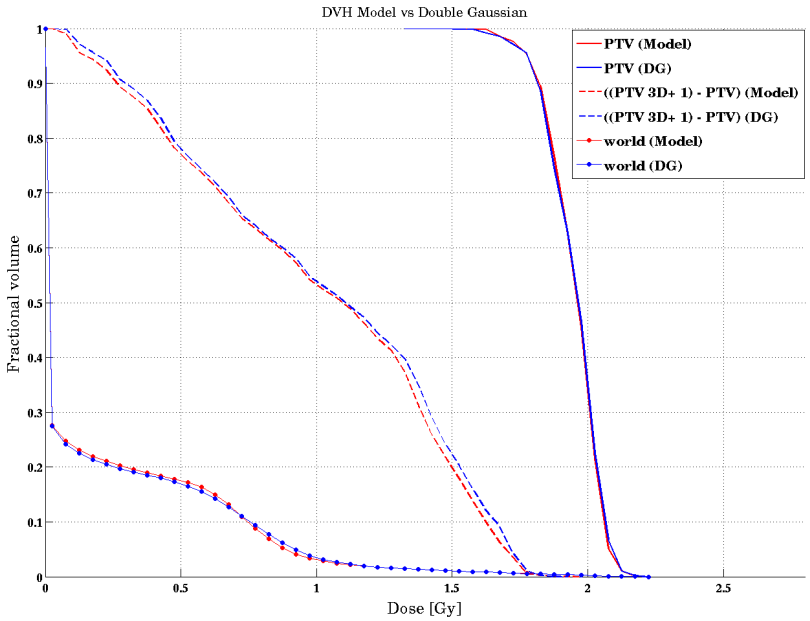

Figure 4.12: Same as in Fig.4.10, comparing the results of the DG (blue curves) and the model ones (red curves).

4.2.2 Kolmogorov-Smirnov test

As for the single beam case, to quantify the discrepancy in the lateral profile results, a Kolmogorov-Smirnov test is performed. This time, the test compares the model versus its *MC Opt ReCalc* and the DG versus its *MC Opt ReCalc*. The *p-value* trends, reported in Fig.4.13, are in good agreement with the single beam test, showing a better accuracy between the model evaluation with the model *MC Opt ReCalc* instead than the DG with the DG *MC Opt ReCalc*

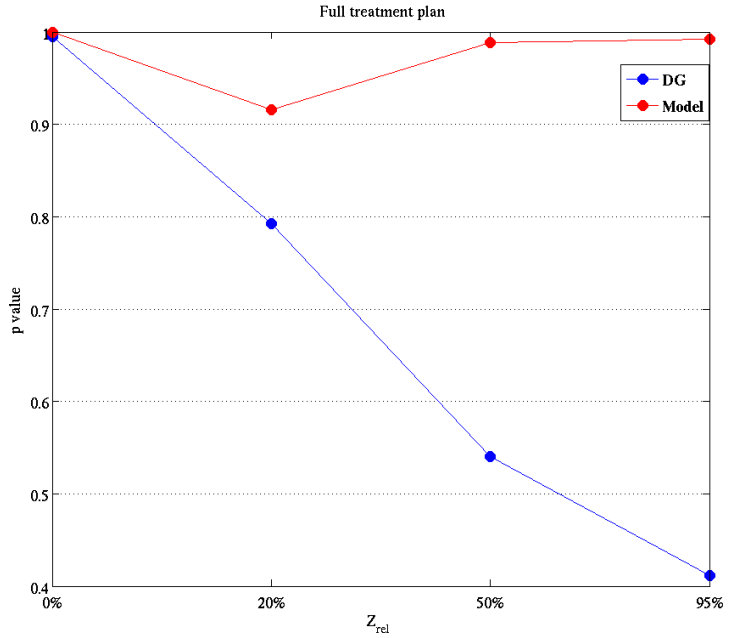

Figure 4.13: P-value results of Kolmogorov-Smirnov test for the the full treatment plan dose evaluation,at the relative depths of Z_{rel} = 0%, 20%, 50%, 95%. The points are joined by a segmented line to improve visualization. The DG values are displayed in blue, the model ones in red

4.2.3 Residual analysis

The residual[1] analysis is performed for the XY plane, orthogonal to the beam direction, to quantify the spatial the difference of two cases:

1. DG − DG *MC Opt ReCalc*
2. model − model *MC Opt ReCalc*

at relative depths of $Z_{rel} = 50\%, 80\%, 95\%$. In Fig.4.14−4.16, a clear difference of the halo can be seen for the case (1) versus case (2); furthermore the difference for the DG case increases with the increase of the depth and the energy, while for the model it remains almost constant (showing a good agreement with the MC).

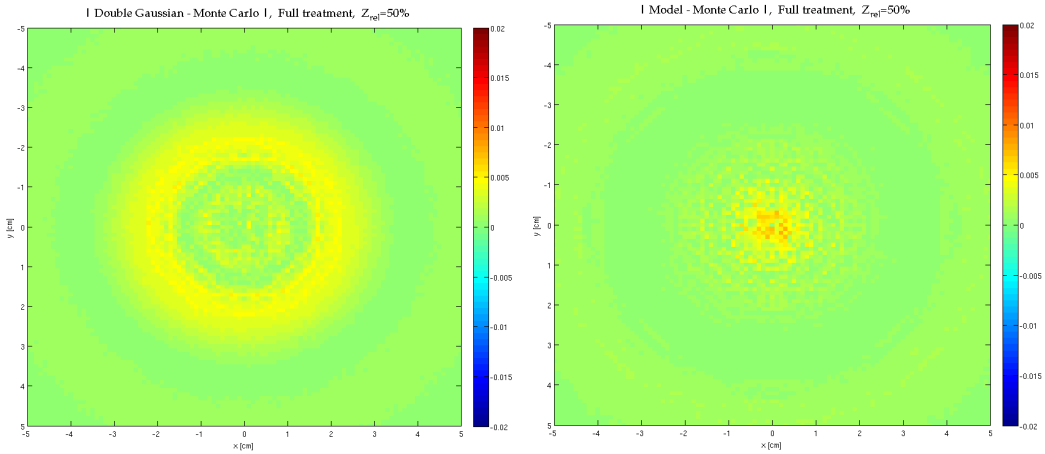

Figure 4.14: Net difference between the dose deposition in Gy, obtained for the treatment using DG lateral parametrization and the relative *MC Opt ReCalc (left)* and using the model evaluation compared in the same way with the MC re-evaluation for the model *(right)*; both for the relative depth $Z_{rel} = 50\%$.

[1]The difference between the observed value of the dependent variable and the predicted value is called the residual. Each data point has one residual.
Residual = Observed value − Predicted value, in this case the predicted values are the MC values.

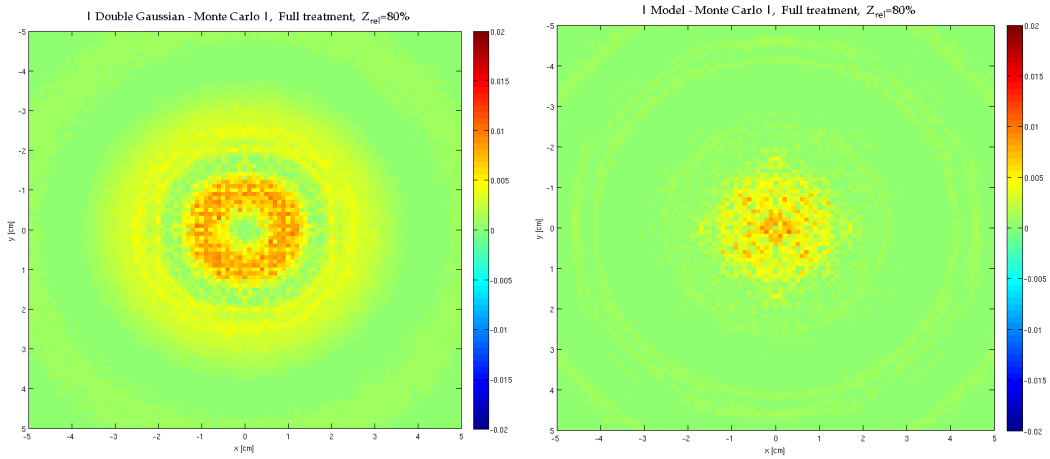

Figure 4.15: Same as in Fig.4.14 for the relative depth $Z_{rel} = 80\%$.

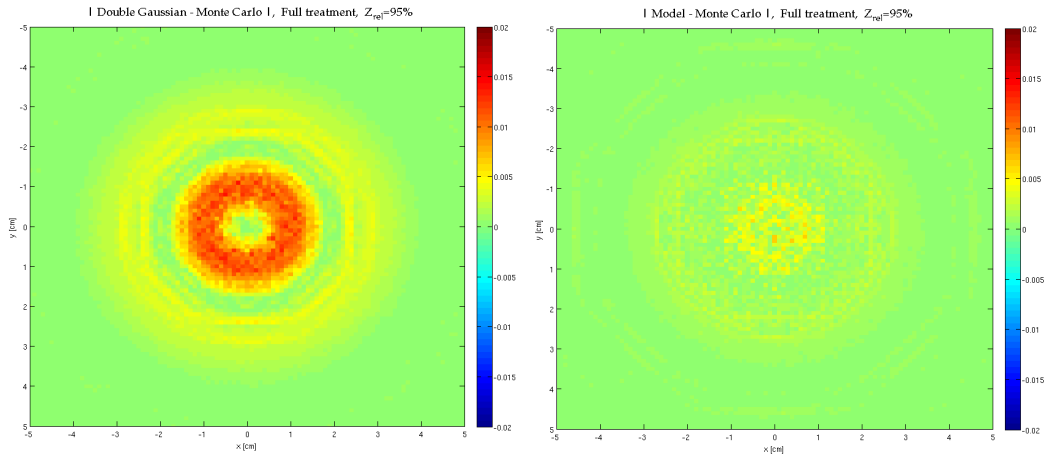

Figure 4.16: Same as in Fig.4.14 for the relative depth $Z_{rel} = 95\%$.

4.3 Inhomogeneities

Currently, CERR treatment plans are produced assuming the phantom as homogeneous water, treating all the materials in equivalent water media by converting the different densities in different Water Equivalent Path Lengths (WEPL). But it has to be considered that if a particle beam is passing trough interface between two media of different densities (and therefore relative stopping powers), it undergoes different Coulomb scattering events [68].
As last step of this work, a preliminary study of how do density heterogeneities affect the lateral profiles characteristics will be presented (the problem of range uncertainty is not treated here).
For this purpose, two cases have been considered; first a parallelepiped of bone was placed in the phantom, before the PTV, as in Fig.4.17, and second the same plan has been evaluating with a parallelepiped of fat. For both phantoms, two plans are evaluated using a single monochromatic beam as for the previous cases (Sec.4.1)), using the DG and the model for the lateral dose calculations. Since the model is implemented in CERR, it is set to evaluate the lateral profiles using water. But the better solution as a future perspective would be to use it with the real materials to give a more accurate evaluation of the scattering processes (see Chap.2). The *MC Opt ReCalc* of the plan, is evaluated using real materials composition.

4.3.1 Bone

A parallelepiped of bone of $10\times10\times4\,\mathrm{cm}^3$ is inserted in the water phantom at a depth of 14 cm as in Fig.4.17. The bone has a density of $\rho_{bone} = 1.698\,\mathrm{g/cm}^3$ (HU=1000),

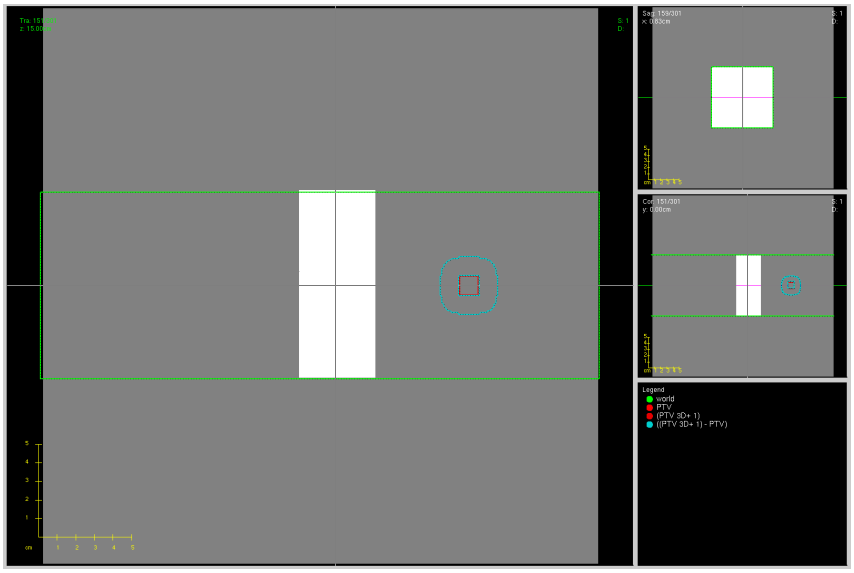

Figure 4.17: Geometry set up displayed in CERR interface. The same as in Fig.4.2 with the inclusion of an inhomogeneity region of a parallelepiped of bone of $10\times10\times4\mathrm{cm}^3$ at a depth of 14 cm.

a mean excitation energy of $I_{bone} = 103,15\,\mathrm{eV}$ and an element composition reported in Tab.4.1.

Element	Volume %
H	0.04521
C	0.21016
N	0.03890
O	0.42090
Mg	0.00171
P	0.08808
S	0.00278
Ca	0.19225

Table 4.1: *Geant4* element composition for bone

The lateral beam profiles of a beam of energy $E = 183$ MeV are presented in Fig.4.18 for a relative of depth of $Z_{rel} = 50\%$ before bone, $Z_{rel} = 70\%$ inside bone and relative depths of $Z_{rel} = 80\%$, 95% after bone.

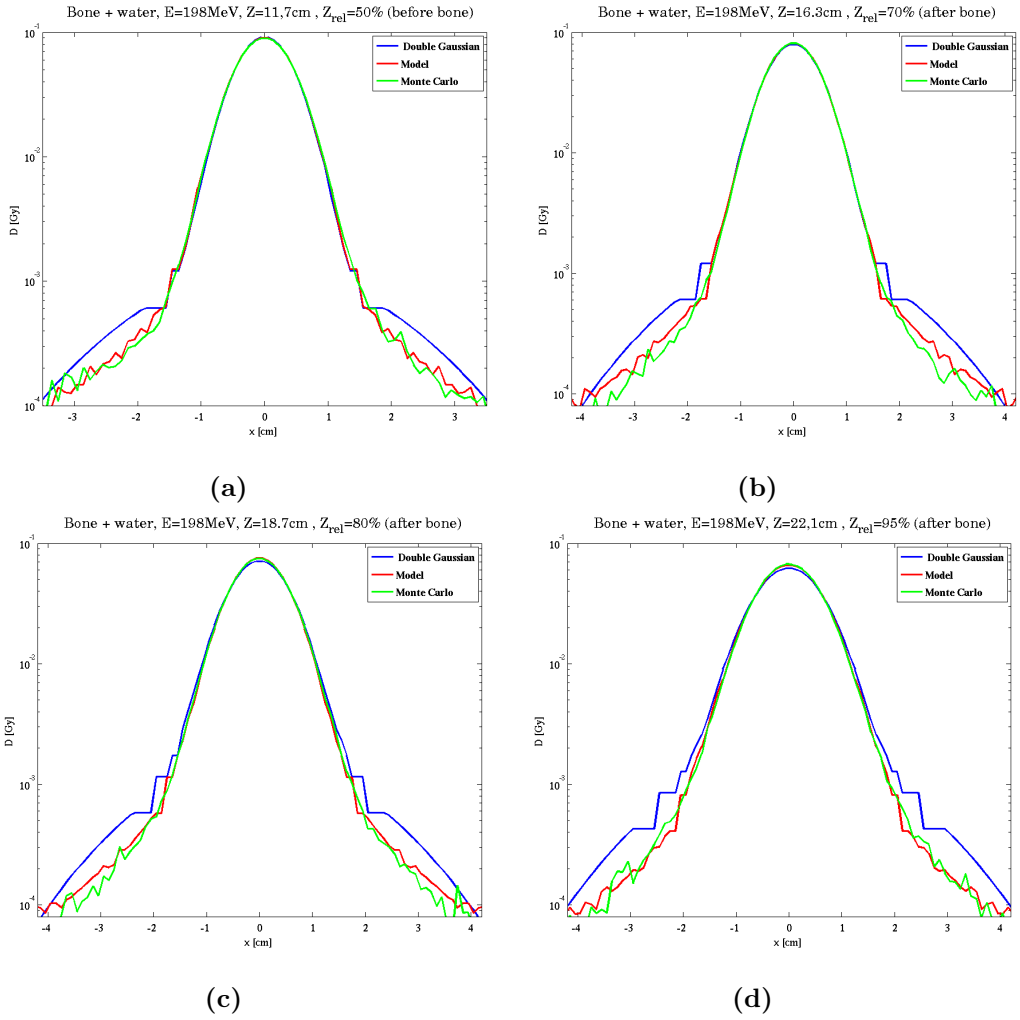

Figure 4.18: Lateral profile of the dose deposition evaluate by CERR TPS, at a relative depth of $Z_{rel} = 50\%$ **(a)**, $Z_{rel} = 70\%$ **(b)**, $Z_{rel} = 80\%$ **(c)** and $Z_{rel} = 95\%$ **(d)**, in logarithmic scale, for a single beam of energy $E = 198$ MeV in presence of a bone inhomogeneity. The blue curve represents the dose evaluated using the DG lateral approximation, in red, the one obtained using the model to evaluate the same plan and the green the *MC Opt ReCalc*.

The model shows a good agreement with the *MC Opt ReCalc*, also after the inhomogeneity. To quantify this result, a Kolmogorov-Smirnov test has been performed, and the results are reported in Fig.4.19. The test confirms the agreement between the model and the *MC Opt ReCalc*, for all the depths, and a good p-value for the double Gaussian before the bone, while it is consistently decreasing after the bone inhomogeneity due to the approximation of the Gaussian function that increase with the increment of the depth (in this case, bone has a much higher density compared to water, that results in a longer WEPL, so in a deeper Z).

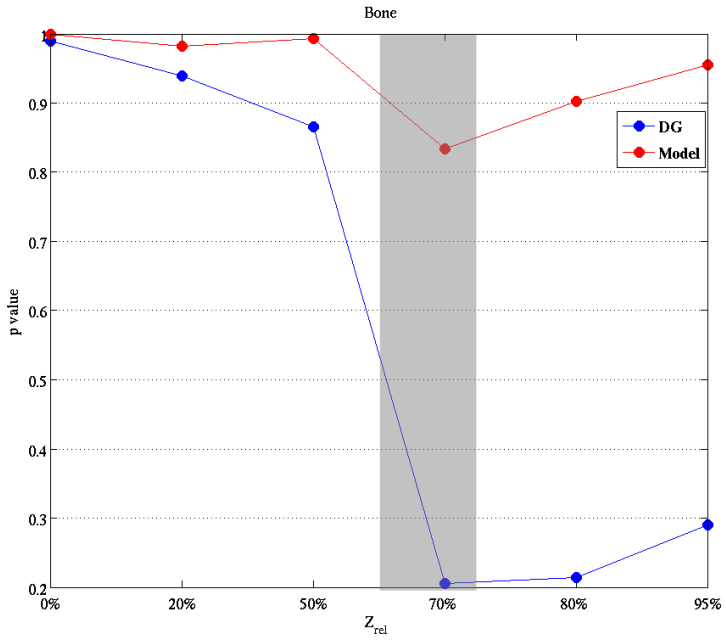

Figure 4.19: P-values results of Kolmogorov-Smirnov test for for a single beam of energy $E = 198$ MeV, in presence of a bone inhomogeneity schematically represented with the gray bar. Results are reported for a relative of depth of $Z_{rel} = 50\%$ before bone, $Z_{rel} = 70\%$ inside bone and relative depths of $Z_{rel} = 80\%$, 95% after bone. A segmented line that connects points is added to improve visualization. The DG values are displayed in blue, the model ones in red.

In addition, the lateral beam shape of the three curves, normalized per area, has been tested evaluating the different lateral sizes of each curve as in Sec.4.1.4. The values of the FWHM, FW20%M, FW10%M and FW0.5%M are reported in Fig.4.20 for a relative of depth of $Z_{rel} = 50\%$ before bone, $Z_{rel} = 70\%$ inside bone and relative depths of $Z_{rel} = 80\%$, 95% after bone. Also this test confirm the good agreement between the model and the *MC Opt ReCalc* for all the analysed cases; the values of FWHM, FW20%M, FW10%M of the double Gaussian are comparable with the MC for all the depths before bone, while they are less accurate after the

inhomogeneity showing an overestimation of the dose that increase with the increase of the depth. Instead, the values for the FW0.5%M of the DG are not accurate for all the depths (excluded 0 depth).

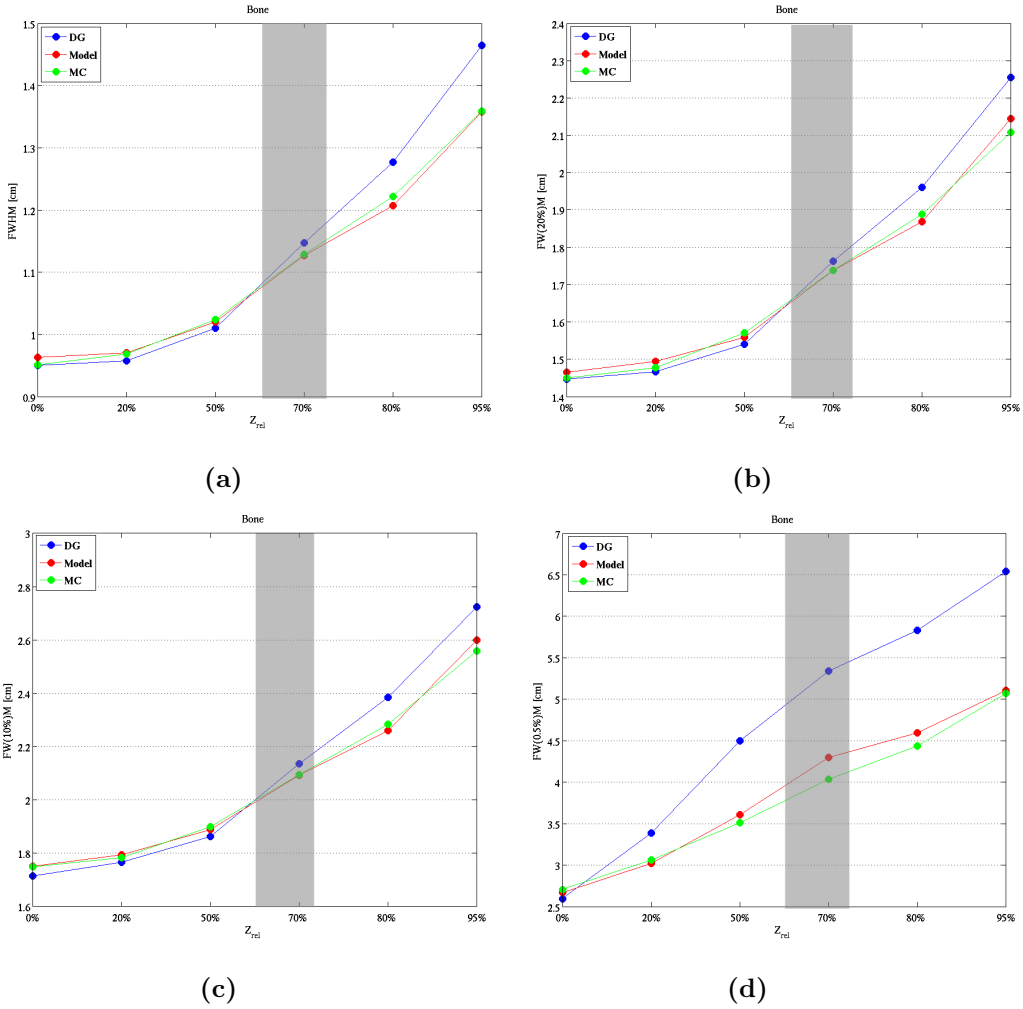

Figure 4.20: Plots of the values for the FWHM **(a)**, FW20%M **(b)**, FW10%M **(c)** and FW0.5%M **(d)** for a single beam of energy $E = 198$ MeV, in presence of a bone inhomogeneity schematically represented by with the gray bar, at the relative depths of $Z_{rel} = 0\%$, 20%, 50% before bone, and 70% inside bone, 80%, 95% after bone.

4.3.2 Fat

In this case a parallelepiped of fat of $10 \times 10 \times 4\,\mathrm{cm}^3$ is inserted replacing bone in Fig.4.17. The fat has a density of $\rho_{fat} = 0.9528\,\mathrm{g/cm}^3$ (HU=-100), a mean excitation energy of $I_{fat} = 63.86\mathrm{eV}$ and an element composition reported in Tab.4.2.

Element	Volume %
H	0.11527
C	0.64204
N	0.00440
O	0.23716
Na	0.00114

Table 4.2: *Geant4* element composition for fat

As for the case of bone inhomogeneity the lateral beam profiles were analysed. To study the same geometry, the beam energy has changed with respect to previous phantom, obtaining $E = 183$ MeV; the results are shown in Fig.4.21 for a relative of depth of $Z_{rel} = 50\%$ before fat, $Z_{rel} = 70\%$ inside fat and relative depths of $Z_{rel} = 80\%$, 95% after fat.

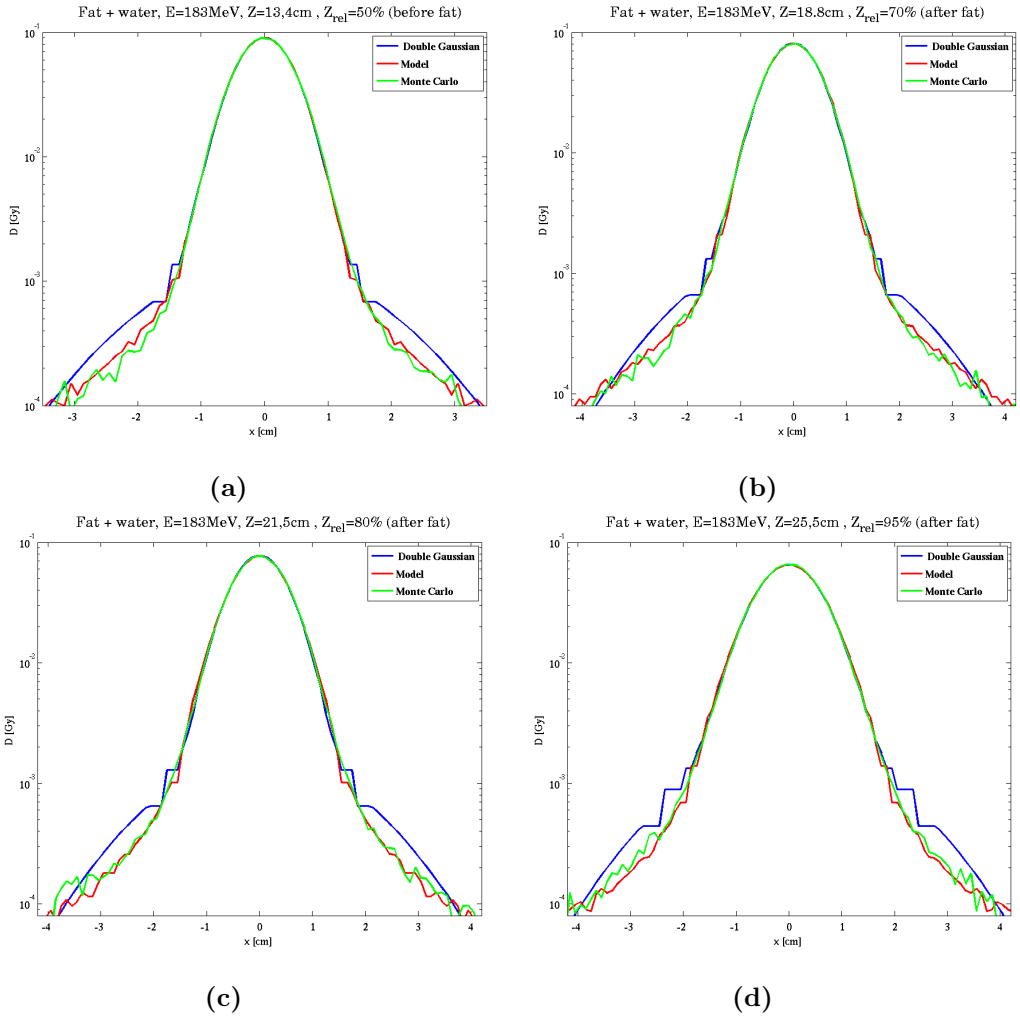

Figure 4.21: Lateral profile of the dose deposition evaluate by CERR TPS, at a relative depth of $Z_{rel} = 50\%$ **(a)**, $Z_{rel} = 70\%$ **(b)**, $Z_{rel} = 80\%$ **(c)** and $Z_{rel} = 95\%$ **(d)**, in logarithmic scale, for a single beam of energy $E = 183$ MeV in presence of a fat inhomogeneity. The blue curve represents the dose evaluated using the DG lateral approximation to evaluate the plan, in red, the one obtained using the model to evaluate the same plan and the green one is the *MC Opt ReCalc*.

Also in this case, the model presents a good agreement with the *MC Opt ReCalc*, for all the the depths. The agreement of the DG is better respect to the case of bone inhomogeneity since the scattering and nuclear effects have a less relevant role for fat as well as the absorption. The Kolmogorov-Smirnov test confirms these results, shown in Fig.4.22. The models values are accurate before the fat, and slightly decrease at greater depths. The DG presents the same behaviour but with lower p-values, especially for deep relative depths. This can be due, to a poor evaluation of the absorption process, which is not taken into account by the model and DG. But the accuracy of the model is still satisfactory because the MCS events are fully considered.

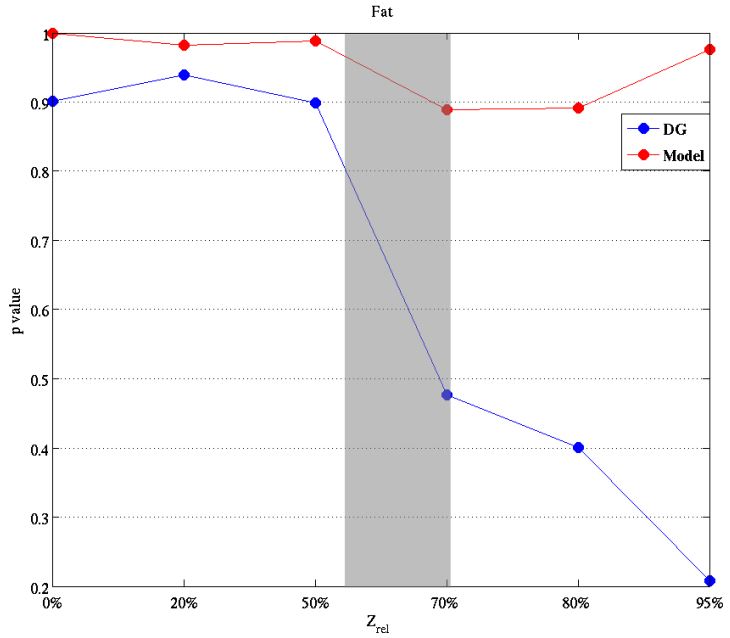

Figure 4.22: P-values results of Kolmogorov-Smirnov test for for a single beam of energy $E = 183$ MeV, in presence of a fat inhomogeneity schematically represented by the gray bar, at the relative depths of $Z_{rel} = 0\%$, 20%, 50% before fat, $Z_{rel} = 70\%$ inside fat and $Z_{rel} = 80\%$, 95% after fat. A linear interpolation of the points is added to improve visualization. The DG values are displayed in blue, the model ones in red.

The heterogeneity does not affects the accuracy in the evaluation of the lateral width for the model, as results from the evaluation of the FWHM, FW20%M, FW10%M and FW0.5%M, reported in Fig.4.23 for the relative of depths of $Z_{rel} = 50\%$ before fat, $Z_{rel} = 70\%$ inside fat and relative depths of $Z_{rel} = 80\%$, 95% after fat.
The DG, instead shows an underestimation of the dose for the FW20%M, FW10%M and a consistent overestimation of the dose for the FW0.5%M, that increases with the increasing of the depth (0 depth excluded).

4.4 Conclusion

The dose deposition of several plans calculated with the CERR TPS has been studied by comparing the lateral dose profiles obtained with the model calculations and the DG ones, using the *Geant4 MC Opt ReCalc* as reference. Starting with the case of a single beam in an homogeneous water phantom, several energies and depths have been analysed; the model showed a good agreement with the MC, and an improvement in the accuracy of the lateral dose calculation compared with the DG results (Fig.4.3,4.6). The differences of the DG are increasing with the increase of the depth

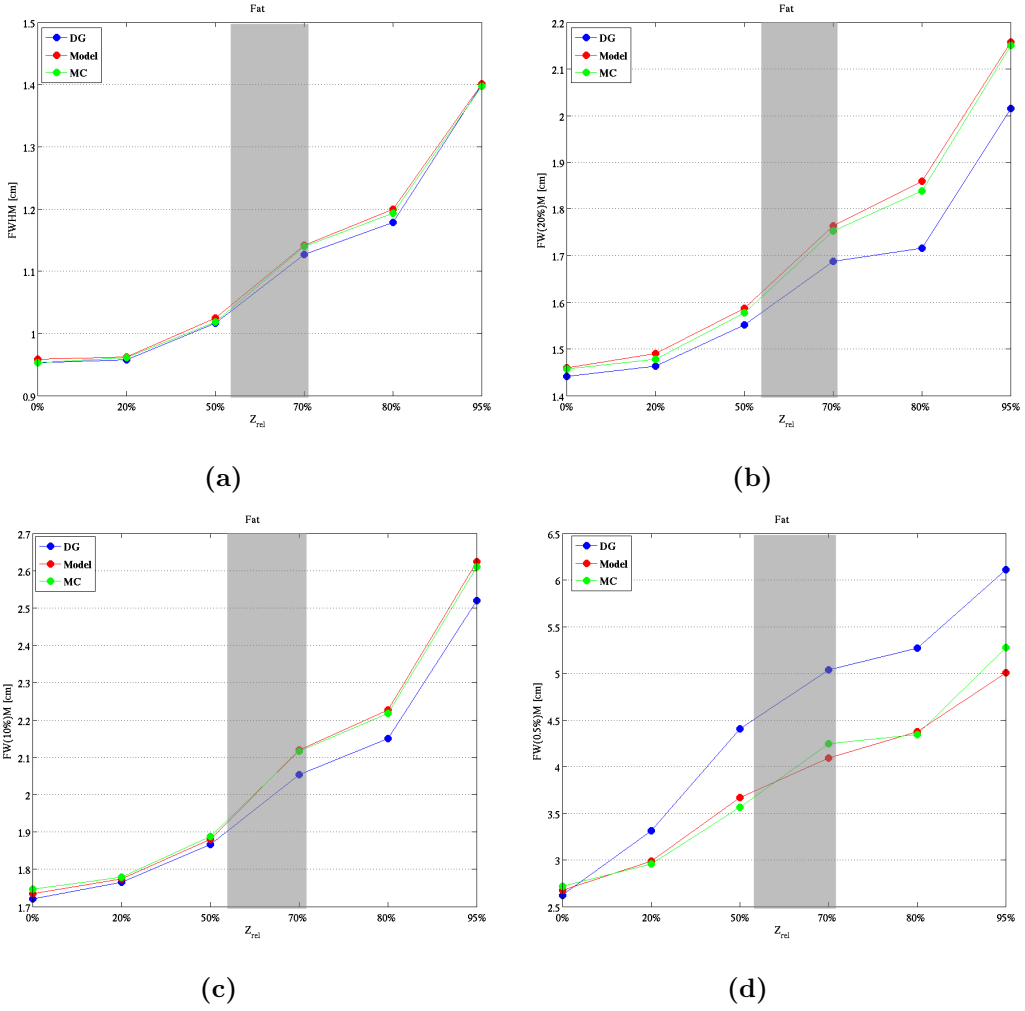

Figure 4.23: Plots of the values for the FWHM **(a)**, FW20%M **(b)**, FW10%M **(c)** and FW0.5%M **(d)** for a single beam of energy $E = 183$ MeV, in presence of a fat inhomogeneity schematically represented by the gray bar, at the relative depths of $Z_{rel} = 0\%$, 20%, 50% before fat, and 70% 80% 95% after fat.

and the energies, since the scattering increases as well and the function approximation presents a non smooth behaviour, with a general slight underestimation of the the dose and an overestimation on the tails at FW0.5%M (see Fig.4.5,4.6,4.7).
A full plan has been studied as well, and also in this case, the model agrees very well with its *MC Opt ReCalc*, while the DG is not so accurate compared with its *MC Opt ReCalc*(Fig.4.9). From the analysis of the DVH, one can conclude that the usage of the model can lead to an improvement in the treatment quality, since the dose in the PTV surrounding area is lower for the model with respect to the DG, at the same dose in the PTV (Fig.4.12); furthermore, the dose evaluated with the DG is less accurate with respect to the one with the model if one compares the two results with the respective *MC Opt ReCalc* as in Fig.4.10,4.11. This means that the predictions of the model are more similar to the predictions of the MC with respect to the ones of the DG.
As last study case, inhomogeneous phantoms have been studied considering fat and bone tissues. Even if the model performs the calculation in water-equivalent approximation, its accuracy is still good and, as a future perspective, can be improved by using the model to evaluate real materials, to better predict the lateral scattering. Based on these results, one can conclude that the model can be a good candidate to replace the DG approximation to enhance the dose calculation accuracy.

Chapter 5

Conclusions

The first part of this thesis presents a new pencil beam model based on the Molière theory, that allows to analytically predict the lateral deflection of a particle beam traversing a thickness of any kind of material, with the same precision of MC codes but with much shorter computational time [5].
The model avoids free parameters for the electromagnetic interaction, and fully takes into account nuclear effects in the tail of the lateral displacement with a two-parameters function. It has been validated in homogeneous water for proton beams with a systematic study on several energies in the range of clinical interest ($60\,\mathrm{MeV} < E < 250\,\mathrm{MeV}$), comparing the results against FLUKA MC simulations and HIT data. Since the comparison with data and MC shows very good agreement, the model can be proposed to be used instead the currently used DG parametrization; this solution can enhance the accuracy of the lateral profile evaluation in hadrontherapy practice, that can be a critical parameter especially in the case of deep tumours near to organs at risk.
A paper that describes the complete version of the model that allows the calculation of the thee-dimensional dose, including the XY plan lateral dose (2.5) and also the BP accurate position, is currently in preparation [69]. Since the model is much faster that the MC but with the same accuracy in water, as a future perspective it can be proposed for the online beam monitoring to replace the MC mode, and also as a powerful and flexible tool for the forward dose evaluation.
A future step will be the study of the effects of different materials and the geometry, including interfaces and the use of other particles already clinically used, *e.g.* Carbon ions, α particles.

In the second part of this work, a Matlab - C++ code has been developed to insert the model in the CERR TPS in order to test the differences between the TPS

dose calculation by using the current DG function and the model. First, the case of a single mono energetic beam in homogeneous water phantom has been considered, with a systematic study on several energies and depths; the results of the comparison between the model and the DG calculations have been validated against *Geant4* simulations[1] , a quantitative study has been done using a Kolmogorov-Smirnov test and a lateral width verification. Furthermore, the scenario of a complete treatment plan in water phantom was studied, testing a small PTV at a considerable depth (20 cm), as an example of a possible clinical difficult case. The same statistical tests were done, and in addiction the residual analysis and the DVHs were studied. Also in this case the accuracy between the model and its MC re-evaluation was better than the DG ones, especially for the deeper depths and higher energies.
As last step, heterogeneous phantoms were considered with a bone and fat inclusions.
The results show a good agreement between the model and the MC for all the analysed cases, and an higher accuracy with respect to DG approximation. The computational time to obtain an optimized treatment plan by using the DG is comparable with the ones by using the model calculation[2] ($\simeq$3 min for a single beam with a geometry as in Fig.4.2) and much lower respect to MC revaluation ($\simeq$4 hours as magnitude order for the same set-up with a statistic of 10^7 initial particles).

Overall, a promising perspective would be to implement the model in TPS to substitute the DG calculation, to have a sensible improvement of the lateral dose evaluation; the further step could be also to use the model accounting for inhomogeneities (not as WEPL but with real materials composition) and to create a database of lateral dose profile with the model, as for example the matrix used in this work, to have a fast and precise LUT that requires as input only energy and depth.

[1] A comparison between the MC code of FLUKA and *Geant4* has been performed first, to make sure that the differences between the model (validated on FLUKA) and DG of CERR and CERR itself (based on *Geant4*) could not be due to the differences between the codes results. The comparison shown in 3.7 ensure the compatibility between the two simulations results.

[2] This comparison refers to the time of using the model for which a database was created for each energy (the computational time to create a single matrix on the same computer on which the time mentioned above were been evaluated, is $\simeq$2.5 min)

References

[1] www.quantumdiaries.org. **www.quantumdiaries.org**. vii, 11

[2] Marco Durante and Harald Paganetti. **Nuclear physics in particle therapy: a review**. *Reports on Progress in Physics*, **79**(9):096702, 2016. 2, 5, 6

[3] R Frühwirth and M Regler. **On the quantitative modelling of core and tails of multiple scattering by Gaussian mixtures**. *Nuclear Instruments and Methods in Physics Research Section A: Accelerators, Spectrometers, Detectors and Associated Equipment*, **456**(3):369–389, 2001. 2, 5, 6, 13, 45

[4] Katia Parodi, Andrea Mairani, and Florian Sommerer. **Monte Carlo-based parametrization of the lateral dose spread for clinical treatment planning of scanned proton and carbon ion beams**. *Journal of radiation research*, **54**(suppl 1):i91–i96, 2013. 2, 5, 6, 38

[5] VE Bellinzona, M Ciocca, A Embriaco, A Fontana, A Mairani, M Mori, and K Parodi. **On the parametrization of lateral dose profiles in proton radiation therapy**. *Physica Medica*, **31**(5):484–492, 2015. 2, 5, 6, 39, 93

[6] Martin Soukup, Matthias Fippel, and Markus Alber. **A pencil beam algorithm for intensity modulated proton therapy derived from Monte Carlo simulations**. *Physics in Medicine and Biology*, **50**(21):5089, 2005. 2, 5, 6, 33

[7] E Pedroni, S Scheib, T Böhringer, A Coray, M Grossmann, S Lin, and A Lomax. **Experimental characterization and physical modelling of the dose distribution of scanned proton pencil beams**. *Physics in medicine and biology*, **50**(3):541, 2005. 2, 5, 6

[8] Harald Paganetti. **Range uncertainties in proton therapy and the role of Monte Carlo simulations**. *Physics in medicine and biology*, **57**(11):R99, 2012. 2, 5, 6

[9] EV Bellinzona, M Ciocca, A Embriaco, A Ferrari, A Fontana, A Mairani, K Parodi, A Rotondi, P Sala, and T Tessonnier. **A model for the accurate computation of the lateral scattering of protons in water**. *Physics in medicine and biology*, **61**(4):N102, 2016. 2, 3, 5, 6, 15, 45

[10] TT Böhlen, F Cerutti, MPW Chin, A Fassò, A Ferrari, PG Ortega, A Mairani, PR Sala, G Smirnov, and V Vlachoudis. **The FLUKA code: developments and challenges for high energy and medical applications**. *Nuclear Data Sheets*, **120**:211–214, 2014. 2, 5, 6

[11] Alfredo Ferrari, Paola R Sala, Alberto Fasso, and Johannes Ranft. **FLUKA: a multi-particle transport code**. Technical report, Stanford Linear Accelerator Center (United States). Funding organisation: US Department of Energy (United States), 2005. 2, 5, 6

[12] W. Ulmer. **Theoretical aspects of energyrange relations, stopping power and energy straggling of protons**. *Radiation Physics and Chemistry*, **76**(7):1089 – 1107, 2007. 2, 5, 6, 32

[13] Joseph O Deasy, Angel I Blanco, and Vanessa H Clark. **CERR: a computational environment for radiotherapy research**. *Medical physics*, **30**(5):979–985, 2003. 2, 3, 5, 6, 49, 52, 66

[14] Stefan Schell and Jan J Wilkens. **Advanced treatment planning methods for efficient radiation therapy with laser accelerated proton and ion beams**. *Medical physics*, **37**(10):5330–5340, 2010. 2, 3, 5, 6, 49, 52, 66

[15] Lindsey A Torre, Freddie Bray, Rebecca L Siegel, Jacques Ferlay, Joannie Lortet-Tieulent, and Ahmedin Jemal. **Global cancer statistics, 2012**. *CA: a cancer journal for clinicians*, **65**(2):87–108, 2015. 9

[16] Huan Giap and Bosco Giap. **Historical perspective and evolution of charged particle beam therapy**. *Translational Cancer Research*, **1**(3):127–136, 2012. 9

[17] Harald Paganetti. *Proton therapy physics*. CRC Press, 2016. 10, 12, 13

[18] Dieter Schardt, Thilo Elsässer, and Daniela Schulz-Ertner. **Heavy-ion tumor therapy: physical and radiobiological benefits**. *Reviews of modern physics*, **82**(1):383, 2010. 10, 11

[19] William Henry Bragg and R Kleeman. **XXXIX. On the α particles of radium, and their loss of range in passing through various atoms and molecules**. *The London, Edinburgh, and Dublin Philosophical Magazine and Journal of Science*, **10**(57):318–340, 1905. 10

[20] Robert R Wilson. **Radiological use of fast protons**. *Radiology*, **47**(5):487–491, 1946. 10

[21] D Schardt, I Schall, H Geissel, H Irnich, G Kraft, A Magel, MF Mohar, G Münzenberg, F Nickel, C Scheidenberger, et al. **Nuclear fragmentation of high-energy heavy-ion beams in water**. *Advances in Space Research*, **17**(2):87–94, 1996. 11

[22] Gerhard Kraft. **Tumor therapy with heavy charged particles**. *Progress in Particle and Nuclear Physics*, **45**:S473–S544, 2000. 11

[23] Charles Kittel. *Elementary statistical physics*. Courier Corporation, 2004. 13

[24] Hartland S Snyder and William Taussig Scott. **Multiple scattering of fast charged particles**. *Physical Review*, **76**(2):220, 1949. 13

[25] WT Scott. **Mean-value calculations for projected multiple scattering**. *Physical Review*, **85**(2):245, 1952. 13

[26] Saunderson Goudsmit and JL Saunderson. **Multiple scattering of electrons**. *Physical Review*, **57**(1):24, 1940. 13

[27] HW Lewis. **Multiple scattering in an infinite medium**. *Physical review*, **78**(5):526, 1950. 13

[28] Gert Moliere. **Theorie der Streuung schneller geladener Teilchen II Mehrfach-und Vielfachstreuung**. *Zeitschrift für Naturforschung A*, **3**(2):78–97, 1948. 13, 17

[29] H. A. Bethe. **Molière's Theory of Multiple Scattering**. *Phys. Rev.*, **89**:1256–1266, Mar 1953. 13, 22, 23, 45

[30] Harald Paganetti. *Proton therapy physics*. CRC Press, 2011. 16, 53

[31] L. Braicovich, B. De Michelis, and A. Fasana. **Plural Scattering of Electrons and Positrons**. *Phys. Rev.*, **154**:234–238, Feb 1967. 16

[32] G Bendiscioli, E Lodi Rizzini, A Rotondi, and A Venaglioni. **Coulomb multiple scattering of heavy particles**. *Il Nuovo Cimento A*, **68**(2):101–122, 1982. 17

[33] B Gottschalk, AM Koehler, RJ Schneider, JM Sisterson, and MS Wagner. **Multiple Coulomb scattering of 160 MeV protons**. *Nuclear Instruments and Methods in Physics Research Section B: Beam Interactions with Materials and Atoms*, **74**(4):467–490, 1993. 17, 27, 31

[34] BP Nigam, MK Sundaresan, and Ta-You Wu. **Theory of multiple scattering: second Born approximation and corrections to Moliere's work**. *Physical Review*, **115**(3):491, 1959. 17

[35] Rafael Garcia-Molina. **Peter Sigmund, Particle Penetration and Radiation Effects. Volume 2: Penetration of Atomic and Molecular Ions (2014), Springer, Switzerland. ISBN 978-3-319-05563-3.**, 2015. 22

[36] William T. Scott. **The Theory of Small-Angle Multiple Scattering of Fast Charged Particles**. *Rev. Mod. Phys.*, **35**:231–313, Apr 1963. 25, 26, 28

[37] U. Fano. **Inelastic Collisions and the Molière Theory of Multiple Scattering**. *Phys. Rev.*, **93**:117–120, Jan 1954. 27, 28

[38] Bernard Gottschalk. **On the scattering power of radiotherapy protons**. *Medical Physics*, **37**(1):352–367, 2010. 28

[39] U. Schneider, J. Besserer, and P. Pemler. **On small angle multiple Coulomb scattering of protons in the Gaussian approximation**. *Zeitschrift fr Medizinische Physik*, **11**(2):110 – 118, 2001. 28

[40] W. Ulmer and B. Schaffner. **Foundation of an analytical proton beamlet model for inclusion in a general proton dose calculation system**. *Radiation Physics and Chemistry*, **80**(3):378 – 389, 2011. 28, 29, 33

[41] K Parodi, A Mairani, S Brons, B G Hasch, F Sommerer, J Naumann, O Jkel, T Haberer, and J Debus. **Monte Carlo simulations to support start-up and treatment planning of scanned proton and carbon ion therapy at a synchrotron-based facility**. *Physics in Medicine and Biology*, **57**(12):3759, 2012. 28

[42] Virgil L. Highland. **Some practical remarks on multiple scattering**. *Nuclear Instruments and Methods*, **129**(2):497 – 499, 1975. 31

[43] Geant4 Collaboration et al. **Physics reference manual**. *Version geant4*, **9**, 2007. 33

[44] T.T. Bhlen, F. Cerutti, M.P.W. Chin, A. Fass, A. Ferrari, P.G. Ortega, A. Mairani, P.R. Sala, G. Smirnov, and V. Vlachoudis. **The {FLUKA} Code: Developments and Challenges for High Energy and Medical Applications**. *Nuclear Data Sheets*, **120**:211 – 214, 2014. 36

[45] Alfredo Ferrari, Paola R Sala, Alberto Fasso, and Johannes Ranft. **FLUKA: A multi-particle transport code (Program version 2005)**. Technical report, 2005. 36

[46] T Goorley, M James, T Booth, F Brown, J Bull, LJ Cox, J Durkee, J Elson, M Fensin, RA Forster, et al. **Initial MCNP6 release overview**. *Nuclear Technology*, **180**(3):298–315, 2012. 36

[47] A. Ferrari, P.R. Sala, R. Guaraldi, and F. Padoani. **An improved multiple scattering model for charged particle transport**. *Nuclear Instruments and Methods in Physics Research Section B: Beam Interactions with Materials and Atoms*, **71**(4):412 – 426, 1992. 36

[48] A Fasso, A Ferrari, J Ranft, and PR Sala. **An update about FLUKA**. In *Proc. 2nd workshop on Simulating Accelerator Radiation Environment, SARE-2, CERN-Geneva*, pages 9–11, 1995. 36

[49] John T Goorley, M James, T Booth, F Brown, J Bull, Lawrence J Cox, J Durkee, J Elson, M Fensin, RA Forster, et al. **Initial MCNP6 release overview-MCNP6 version 1.0**. *Los Alamos National Laboratory, Los Alamos, NM, LA-UR-13-22934*, **1**, 2013. 36

[50] K Parodi, A Mairani, S Brons, J Naumann, M Krmer, F Sommerer, and T Haberer. **The influence of lateral beam profile modifications in scanned proton and carbon ion therapy: a Monte Carlo study**. *Physics in Medicine and Biology*, **55**(17):5169, 2010. 38

[51] J Schwaab, S Brons, J Fieres, and K Parodi. **Experimental characterization of lateral profiles of scanned proton and carbon ion pencil beams for improved beam models in ion therapy treatment planning**. *Physics in Medicine and Biology*, **56**(24):7813, 2011. 39, 40, 41

[52] A Papoulis. **Dual optical systems**. *JOSA*, **58**(5):653–653, 1968. 46, 47

[53] G Amsel, G Battistig, and A Lhoir. **Small angle multiple scattering of fast ions, physics, stochastic theory and numerical calculations**. *Nuclear Instruments and Methods in Physics Research Section B: Beam Interactions with Materials and Atoms*, **201**(2):325–388, 2003. 46, 47

[54] L Grevillot, D Bertrand, F Dessy, N Freud, and D Sarrut. **A Monte Carlo pencil beam scanning model for proton treatment plan simulation using GATE/GEANT4**. *Physics in Medicine and Biology*, **56**(16):5203, 2011. 54

[55] Steve Webb. *The physics of three dimensional radiation therapy: Conformal radiotherapy, radiosurgery and treatment planning*. CRC Press, 1993. 57

[56] Anders Brahme. **Optimization of stationary and moving beam radiation therapy techniques**. *Radiotherapy and Oncology*, **12**(2):129–140, 1988. 57

[57] Olivier C Haas. *Radiotherapy treatment planning: new system approaches*. Springer Science & Business Media, 2012. 57

[58] Florian Kamp. **Comparison of the Lateral Dose Fall-Off for Proton and Ion Beams in Radiation Therapy**. *Journal of Sth*, 2011. 59, 61, 66

[59] Stefan Schell et al. *Dose delivery and treatment planning methods for efficient radiation therapy with laser-driven particle beams*. 2011. 59

[60] Qiuwen Wu and Radhe Mohan. **Algorithms and functionality of an intensity modulated radiotherapy optimization system**. *Medical physics*, **27**(4):701–711, 2000. 59

[61] **fmincon**. `hhttp://de.mathworks.com/help/optim/ug/fmincon.html`. 59

[62] S. Agostinelli et al. **Geant4a simulation toolkit**. *Nuclear Instruments and Methods in Physics Research Section A: Accelerators, Spectrometers, Detectors and Associated Equipment*, **506**(3):250 – 303, 2003. 61

[63] J. Allison et al. **Geant4 developments and applications**. *IEEE Transactions on Nuclear Science*, **53**(1):270–278, Feb 2006. 61

[64] Andreas Franz Resch. **Development of a Monte Carlo simulation-based treatment planning tool for proton therapy**. 2015. 66

[65] Andrej N Kolmogorov. *Sulla determinazione empirica di una legge di distribuzione*. na, 1933. 69

[66] D'Abrera H.J.M. Lehmann E.L. *Nonparametrics : statistical methods based on ranks*. Holden-Day, 1975. 69

[67] Luther W Brady and Theodore E Yaeger. **Encyclopedia of radiation oncology**. 2013. 77

[68] CM Charlie Ma and Tony Lomax. *Proton and carbon ion therapy*. CRC Press, 2012. 83

[69] EV Bellinzona, A Embriaco, A Fontana, and A. Rotondi. **An accurate model for the computation of the dose of protons in water**. (In preparation). 93

Acknowledgement

I would like to express first my deep thanks to my advisor **Prof. Alberto Rotondi**, for giving me the chance to be involved in his amazing flux of ideas and develop one of them, **Dr. Andrea Fontana** for his passion in teaching me and supporting daily my work and **Prof. Dr. Katia Parodi**, who gave me the opportunity to do my thesis as a cotutuelle PhD student at the chair of medical physics at Ludwig-Maximilians-Universität München. You have been great teachers, not only in the science field.

A special thanks to **Dr. Guillaume Landry** , for his precious support at LMU, and his patient in investigating with me the huge and wired word of CERR.
Thanks to my **Munich colleagues**, for the interesting conversations that for sure helped me to grow up (somehow in a German way). Garching can be considered noisy and far away from the civilized word (and actually it is), but thanks to you it has been a really pleasuring working/living place. I want to add a specific thanks to George, Chiara and Marco for their support, and to Andreas for his time, his competence and his deep life philosophy.

And my deep gratitude goes to my **Munich friends**, for all the adventures, the beers and the brilliant ideas born after the beer, for each broken bone (every time it was worthwhile), for each international dinner (sometimes maybe too much international :)) and for all the nice time stolen to my thesis. In particular thanks to Marina, Elvira, Aji, Victor, Steffen, Lia, Phil, Mhuam and Franz (you are more a sweet friend than a colleague); you are precious friends.
Thanks to all of my **room-mates**, that for a matter of time I can't thank one by one. In particular Baki, Neeraj, Patti, Chia Ua, Christof, Mali, Yan Ti, for the amazing time spent together, no German evening has been cold thanks to you.

Silvia and **Chiara** you are making disorder even within the acknowledgement of this thesis! Since you have been colleagues, friends and somehow room-mates,

where should I put you? So, just thanks Silvia to have included me in your shiny and pinky cosmos, for your sweetness and your lovely "organization" and for all the warm hugs; thanks Chiara for having destroyed a huge part of my butterfly word, giving me the chance to see the real one (anyway, I have no intention to exit from mine!), you have really taught me a lot.

Grazie ai **fisici pavesi**, in particolare
Alessia, che chiamare collega è sarebbe indubbiamente riduttivo. Amica, confidente e compagna di passeggiate scientifiche e di vita. Grazie per essere stata la mia Tata e per non avermi gambizzata a Roma :)
E grazie, **Beppe** per aver cercato con me verità recondite nei fumi (..dell'incenso), per avermi rassicurata ogni volta sulla presenza della scarpa sinistra, e sopratutto con la tua presenza, dolcemente cinica e disillusa.

Un amico ci accetta per come siamo e ci aiuta ad essere quello che dovremmo.
Grazie agli amici di una vita:

Sara, l'unica persona che non solo mi ha creato un vezzegiativo animalesco, nominandomi Giraffina Fifina, ma mi ha anche dimostrato che è bello. Mi hai tenuto la mano nel mondo reale, e mi hai voluto bene anche quando mi sono persa nel mio. Grazie per avermi fatto sentire importante e per essere così importante per me, mentre cresciamo insieme.

Mattia, riassumendo: 1) Andiamo a pattinare? Ah, già comunque ciao, sono Elettra. 2) Andiamo a una conferenza sui cambiamenti climatici? Si, e Fondiamo la *Pan Teoria* intanto che ci siamo. 3) Dopo aver passato un'intera serata a parlare della differenza tra le varie specie di anatre, decidiamo di buttare via i vecchi cestini, di creare la *Carta da Parata*, di seguire le rotaie del treno per tornare a casa (non per forza la mia), di raccontarci per anni storie sempre nuove e avvincenti, sapendo che probabilmente è sempre la stessa che ci dimentichiamo, ma ce la dimentichiamo insieme.
Grazie per aver capito questo ringraziamento, per aver capito quello che non ho detto, ma sopratutto quello che ho detto!

A Ulrichk, Dodo, Gaia, Gian, Luca, Chiara, Ste, Sabri, Anna, Susi, Fra e a tutti quelli che mi accolgono con: "Ah! sei tornata, ogni volta senza chiedermi per quanto resto, facendomi sentire a casa.

Alla compagnia dei musicisti per avermi fatto apprezzare la melodia dell'irrazionalità e del vostro incredibile caos (anche se devo ammettere che la birra ha aiutato).

Grazie a **Gaia V.**, per avermi encomiabilmente guidata nella risoluzione degli unici problemi che prorpio non mi appassionano, quelli irrazionali.

"≪Volare mi fa paura≫ stridette Fortunata alzandosi. ≪Quando succederà, io sarò accanto a te≫ miagolò Zorba leccandole la testa. [Luis Seplveda, Storia di una gabbianella e del gatto che le insegn a volare.]

Neno. Per motivi ecologici non posso ringraziarti qui per tutto, mi limito a dirti grazie per come mi hai tenuta per mano ovunque fossimo, per la sicurezza in cui mi culli ogni volta che mi guardi e per il futuro Gallettante che ho sempre più voglia di scoprire insieme a te.
Devo indubbiamente ringraziare anche **Pip** (Josephina Trillian Thompson Taddeolini), il mio morbido criceto arrogante, per avermi fatto di sì con quel bel testino peloso mentre discorrevamo tra un semino e l'altro sul senso della vita dell'universo e tutto. Rimango convinta che tu ora lo conosca.

Un grazie alla mia **famiglia**, grande quanto il vostro amore, per avermi accettata chiassosa, noiosa e piena di *perchè*? E anche se non sono mai riuscita a spiegarvi proprio bene perchè anche se sono Dott. non ho un camice bianco, questo traguardo è anche vostro.

Alla mia sorellina **Ruth** devo un ringraziamento ermetico, come lei; per aver creduto in me senza dirmelo, o dicendomelo a morsi e per avermi mostrato le bizzarre e complesse forme che assume l'affetto, senza spiegazioni ne astrazioni.

Mamma e Papà. Vi voglio ringraziare insieme, perchè insieme mi avete donato la più grande bellezza della vita: La calda sicurezza di essere amata, senza la quale non avrei scritto nemmeno l'introduzione di questa tesi.
Grazie Papà, per non aver messo nessun titolo ai tuoi quadri ne alla mie scelte; per aver combattuto per i tuoi ideali, insegnandomene il valore e permettendomi di avere i miei.

E Mamma, ti potrei ringraziare di avermi fatto riscrivere mille volte i temi perchè pensavi che potessi fare meglio, per non avermi permesso di andare a campeggiare da sola nei boschi perchè l'area attrezzata era troppo mainstream, per avermi avermi spronata/sostenuta/ascoltata davvero sempre (anche quando ho avuto la bizzarra idea di iscrivermi a Fisica invece di Medicina) o per tutte le volte che sei stata più forte per me che per te. Potrei, ma è tutto davvero troppo riduttivo; quindi solo grazie di essere così meravigliosamente tu.

A guardar le nuvole appoggiati di schiena si è più leggeri.

Ettore Bellinzona

2016